



CASE FILE COPY

TECHNICAL MEMORANDUM

X - 48

PRESSURE MEASUREMENTS OBTAINED IN FLIGHT AT TRANSONIC SPEEDS FOR A CONICALLY CAMBERED DELTA WING

By Earl R. Keener

High-Speed Flight Station
Edwards, Calif.

DECLASSIFIED - EFFECTIVE 1-15-64
Authority: Memo Sec. Erobka NASA HQ
Code ATSS-A Dtd. 3-12-64 Subj: Change
in Security Classification Marking.

N 65 12688

(ACCESSION NUMBER)

(THRU)

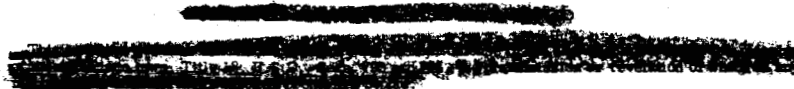
70
(PAGES)

(CODE)

01

(CATEGORY)

(NASA CR OR TMX OR AD NUMBER)



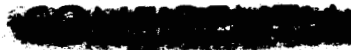
NATIONAL AERONAUTICS AND SPACE ADMINISTRATION

WASHINGTON

October 1959

Hard copy (HC) \$3.00

Microfiche (MF) \$0.75



NASA TM X-48

FACILITY FORM 802

CONFIDENTIAL

NATIONAL AERONAUTICS AND SPACE ADMINISTRATION

TECHNICAL MEMORANDUM X-48

PRESSURE MEASUREMENTS OBTAINED IN FLIGHT AT TRANSONIC SPEEDS FOR A CONICALLY CAMBERED DELTA WING*

By Earl R. Keener

SUMMARY

12688

DECLASSIFIED - EFFECTIVE 1-15-64
Authority: Memo Sec. Drobka NASA HQ.
Code ATSS-A Dtd. 3-12-64 Subj: Change
in Security Classification Marking.

Pressure measurements were made in flight over the conically cambered delta wing of the Convair JF-102A airplane at Mach numbers up to 1.19. Maximum angles of attack tested ranged from 24° at a Mach number of 0.70 to 9° at 1.19.

Appreciably large suction pressures are realized at the leading edge of the wing similar in magnitude to the high suction pressures experienced by thin, plane, delta wings. The cambered leading edge is effective in distributing the low pressures at the leading edge over a greater frontal area, thus increasing the leading-edge thrust. The conical distribution of camber results in near-elliptic span-load distributions at the lower angles of attack; however, a more important effect of conical camber (together with the wing fences and reflexed tips incorporated by the JF-102A) is the delay to higher angles of attack in the occurrence of flow separation that normally occurs on a plane delta wing. A favorable effect on the pressure drag may also be attributed to the delay in flow separation. Although the outboard wing fence probably contributes to the delay in flow separation at the tip, the pressures indicate that the fence induces flow separation inboard of the fence starting near the leading edge at angles of attack of about 8° and extending to the trailing edge as the angle of attack increases.

A wide variation occurs in the span-load distributions from a near-elliptic loading at the lower angles of attack to a near-triangular loading at the very high angles of attack tested. In general, the distributions are similar to those of a plane wing, although the delay in flow separation in the tip region results in slightly larger tip loads

Auth

* Title, Unclassified.

CONFIDENTIAL

1G
H
1
1
6



INTRODUCTION

Theoretically, a suction force is predicted along the leading edge of thin wings at subsonic speeds and also at supersonic speeds if the leading edge is swept behind the Mach cone. Physical realization of the suction force results in an appreciable reduction in drag due to lift. Pressure measurements on thin, plane, delta wings have shown that a large reduction in pressure, approaching a vacuum, is realized at the leading edge (ref. 1). However, drag measurements of such wings have shown that the reduced pressures do not produce the predicted suction force because of the small frontal area over which the suction pressures are distributed (ref. 2).

To distribute the low leading-edge pressures over the maximum possible frontal area, it was suggested in reference 3 that the leading edge be cambered. A theoretical study of leading-edge camber for swept and delta wings (ref. 4) showed that, in addition to cambering the leading edge, the span-load distribution must approximate an ellipse to minimize the induced drag due to lift. A study of surface shapes that result in an elliptic load distribution led to the development of conical camber. The amount of camber depends on the design Mach number and design lift coefficient. Wind-tunnel and flight measurements of airplane drag verified that conical camber results in an appreciable reduction of total drag at moderate angles of attack (refs. 4 and 5).

To study in detail the effects of conical camber on the pressure distribution and span-load distribution of delta wings, pressure measurements were made in the wind tunnel and in flight. Wind-tunnel pressure measurements are available at Mach numbers up to 1.9 in references 6 to 8. The flight measurements are presented herein.

The flight investigation was conducted at the NASA High-Speed Flight Station at Edwards, Calif., utilizing the 6.3-percent conically cambered delta wing of the Convair JF-102A airplane. In addition to conical camber, the wing also incorporates two fences, a reflexed tip, and an elevon-control surface. This paper presents an analysis of the flight measurements of wing pressures at Mach numbers up to 1.2. Particular emphasis is given to the effects of camber on the distribution of the leading-edge pressures and the effects of the combination of camber, fences, and reflexed tip on the span-load distributions. In addition, the flow-separation characteristics, which are not predicted in the theoretical development of conical camber, are discussed. Comparison is made with the flight measurements of wing pressures reported in reference 1 for a plane wing. Tabulated pressure coefficients and integrated aerodynamic coefficients for all data points are available upon request from the National Aeronautics and Space Administration.



SYMBOLS

- b/2 wing semispan
- b'/2 wing-panel span, spanwise distance from first row of orifices (0.186b/2) to wing tip
- C_b wing-panel bending-moment coefficient about 0b'/2,

$$\int_0^1 c_n \frac{c}{c_{av}} \frac{2y'}{b'} d \frac{2y'}{b'}$$
- C_m wing-panel pitching-moment coefficient about 0.25c̄,

$$\frac{c_{av}}{\bar{c}} \int_0^1 c_m' \left(\frac{c}{c_{av}} \right)^2 d \frac{2y'}{b'}$$
- C_N wing-panel normal-force coefficient, $\int_0^1 c_n \frac{c}{c_{av}} d \frac{2y'}{b'}$
- C_p surface-pressure coefficient, $\frac{p - p_\infty}{q}$
- ΔC_p differential-pressure coefficient, $\frac{p_l - p_u}{q}$
- C_{p,sonic} pressure coefficient for a local Mach number of 1
- c local wing chord of uncambered section, measured parallel to plane of symmetry
- c̄ mean aerodynamic chord of wing panel, $2/S \int_0^{b'/2} c^2 dy'$
- c_{av} average chord of wing panel
- c_m wing-section pitching-moment coefficient about 0.25c,

$$\int_0^1 \Delta C_p \left(0.25 - \frac{x}{c} \right) d \frac{x}{c}$$

H
1
1
6



4

c_m' wing-section pitching-moment coefficient about line perpendicular to longitudinal axis of airplane, passing through $0.25\bar{c}$, $c_m + 0.7021\left(1 - \frac{\bar{c}}{c}\right)c_n$

c_n wing-section normal-force coefficient, $\int_0^1 \Delta C_p d \frac{x}{c}$

M free-stream Mach number

p local static pressure

q free-stream dynamic pressure

$S/2$ area of wing panel (outboard of $Ob'/2$)

t wing-section maximum thickness

x chordwise distance rearward of leading edge of local chord

x_{cp} chordwise location of center of pressure of wing section, $100\left(0.25 - \frac{c_m}{c_n}\right)$, percent c

x_{CP} chordwise location of center of pressure of wing panel from leading edge of \bar{c} , $100\left(0.25 - \frac{C_m}{C_N}\right)$, percent \bar{c}

y' spanwise distance outboard of $Ob'/2$

y_{CP} spanwise location of center of pressure of wing panel, $100\left(\frac{C_b}{C_N}\right)$, percent $b'/2$

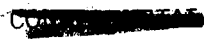
z local ordinate of wing section, measured normal to chord line of uncambered section

α measured airplane angle of attack

δ_e elevon position

Subscripts:

L left



H
1
1
6

- l lower surface
- u upper surface
- ∞ free stream

DESCRIPTION OF AIRPLANE AND WING PANEL

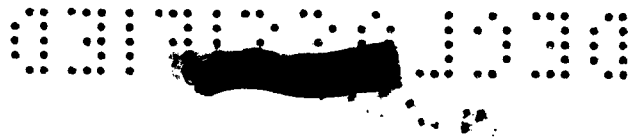
H A three-view drawing presenting the overall dimensions of the
 1 Convair JF-102A airplane is shown in figure 1. Photographs of the air-
 1 plane including several views of the wing showing the leading-edge cam-
 6 ber, fences, and reflexed tip are presented in figure 2. The physical
 characteristics of the airplane and wing panel are given in table I.

A drawing of the wing, including cross-sectional views of the leading edge at each orifice station, is shown in figure 3. The delta wing has an aspect ratio of 2.08, a taper ratio of 0.023, and zero incidence, dihedral, and twist. The leading edge is swept back 60.1°, and the trailing edge is swept forward 5°. Wing fences, shown in figures 1 to 3, are located at 0.225b'/2 and 0.600b'/2. The wing tips are reflexed 6° behind the extended hinge line of the elevon (fig. 3). The wing section is an NACA 0004-65 airfoil modified by leading-edge camber, which is distributed conically over the outer 6.3 percent of the local semispan (fig. 3); the design lift coefficient at a Mach number of 1.0 is 0.166. In providing conical camber the local wing chord was extended slightly over that for an NACA 0004-65 airfoil and, as a result, the wing-section maximum-thickness ratios are slightly less than 4 percent. The wing-section coordinates are presented in table II for the static-pressure-orifice locations.

The geometric characteristics of the elevon, used for longitudinal and lateral control, are included in table I and figure 3. The fuselage of the JF-102A is indented according to area-rule considerations for a Mach number of 1.0.

INSTRUMENTATION AND ACCURACY

Standard NASA instruments were used to record the wing-surface and differential pressures, indicated free-stream static and dynamic pressures, normal acceleration, angle of attack, angle of sideslip, elevon position, and rolling and pitching angular velocities and accelerations. The indicated free-stream static and dynamic pressures were obtained from an airspeed head mounted on a nose boom, and the static-pressure error was determined in flight. Angles of attack and sideslip were



measured by vanes mounted on the nose boom. Elevon position was measured at the elevon midspan. All instruments were correlated by a common timer.

Flush-type static-pressure orifices installed in the left wing were arranged in seven streamwise rows (fig. 3). The orifices were connected by tubing through the wing to multicell mechanical manometers in the instrument compartment. Surface pressures were measured at orifice rows 1, 3, 5, and 7, and differential pressures between the lower and upper surfaces were measured at orifice rows 2, 4, and 6.

Estimated maximum errors of the pertinent recorded quantities and the resulting coefficients are:

M	±0.02
$p - p_\infty$ or $p_l - p_u$, lb/sq ft	±7
δ_{eL} , deg	±0.2
C_p	±0.02
c_n	±0.02
c_m	±0.006
C_N	±0.03
C_m	±0.01

TESTS

The data presented were obtained from pushovers to angles of attack near zero followed by gradual turns to high angles of attack. The data cover the Mach number range from 0.7 to 1.2 at an altitude of 40,000 feet.

Reynolds number for these tests varied between 23×10^6 and 58×10^6 based on the mean aerodynamic chord of the wing.

DATA REDUCTION

Longitudinal control of the JF-102A airplane is obtained by means of elevons on the wing; therefore, the characteristics of the wing at zero elevon deflection could not be obtained throughout the lift range. Consequently, data were selected from the tests at flight conditions for which the airplane was essentially trimmed at each angle of attack (near-zero angular velocity and angular acceleration). Table III presents the Mach number, angle of attack, and elevon deflection for all selected data points. For most data points presented, the pressure lag

resulting from tube length was negligible because the data were obtained from gradual maneuvers. Some lag corrections were necessary, however, for a few of the low-lift data points obtained from the pushovers to near-zero angle of attack; these points are indicated in table III. Lag corrections were determined by the method in reference 9 for photographic instruments, and the corrections were checked in flight by comparing pressure measurements from abrupt and gradual maneuvers. The corrected data comprised 11 of the total 69 data points and compared favorably to the zero-lag data.

Automatic digital computing equipment was used to obtain pressure coefficients from the recorded data and to perform the chordwise and spanwise integrations necessary to obtain the normal-force and pitching-moment coefficients. Wing-panel coefficients are based on the geometric properties of the wing outboard of the first row of orifices ($0.168b'/2$).

RESULTS

The aerodynamic characteristics of the wing sections are presented in figures 4 to 6 in the form of curves of normal-force coefficients, pitching-moment coefficients, and chordwise centers of pressure for nominal Mach numbers of 0.70, 0.90, 1.02, and 1.19. Figure 7 presents aerodynamic characteristics of the wing panel. These figures are presented as basic data, and only the section normal-force characteristics are discussed. Chordwise pressure distributions over the upper and lower surfaces of the wing at four spanwise stations are presented in figure 8 in oblique projection. In addition to Mach number and angle of attack, the pressure coefficients for a local Mach number of $1.0(C_{p,sonic})$ and the elevon deflection angle are given. The effect of the elevon deflection may be noted in the pressure distributions by the abrupt changes in pressure at the elevon junction. The pressure measurements are also affected by the outboard fence, by the reflexed tip, and, somewhat, by the elevon-actuator fairing and the inboard fence (fig. 3).

Figure 9 is presented to compare the thicknesswise pressure distribution for an outboard section of the cambered wing with that of a similar wing section of the plane wing of reference 1. Two angles of attack are shown, 7° and 12° , which represent the moderate angle-of-attack range. It may be noted that the area under the pressure distributions is directly proportional to the wing-section pressure drag. Consequently, suction pressures over the forward part of the wing section represent a negative drag or suction force. In addition to the pressure distribution over the forward part, figure 9 also includes the pressure distribution over the rearward part of the upper surface to show the favorable effect of camber on the pressure drag in this region. The pressure coefficients



are plotted as a function of z/t instead of the usual z/c because the maximum thickness of the plane wing is 6.5-percent chord compared to 4-percent chord for the cambered wing. Although the distributions are uncorrected for elevon deflections and some effect of the outboard fence is present, a qualitative comparison can still be made. For clarity, the leading-edge and trailing-edge locations are noted in the figure.

Figure 10 presents the thicknesswise pressure distributions over the forward part of the wing section to show in detail the effects of leading-edge camber on the leading-edge pressures. Distributions are shown at several angles of attack, and at each angle the pressures at four spanwise stations are superimposed. In this manner the effects of increasing amounts of camber can be seen more readily. Since station $0.584b'/2$ is located immediately inboard of the outboard fence ($0.600b'/2$), the leading-edge pressures include some of the effect of the fence.

Figure 11 shows a comparison of the wing-section normal-force coefficient at three comparable stations for the cambered wing and for the plane wing of reference 1 at $M \approx 0.70$. The span-load distributions for the cambered wing are presented in figure 12. Included in the figure are the locations of the two wing fences, the end of the elevon, and the reflexed tip. Figure 13 shows a comparison of the span-load distributions with an elliptic-load distribution (with minor axis at $0b'/2$, which is approximately the wing-body junction). Figure 14 compares the span-load distributions for the conically cambered and plane delta wings. In this figure the span-load distributions are uncorrected for elevon deflection for both the plane and the cambered wing, therefore the comparison is qualitative only.

DISCUSSION

Effect of Camber on Leading-Edge Suction

Leading-edge pressures.- The chordwise pressure distributions of figure 8 show that appreciable suction pressures are physically realized at the leading edge of the conically cambered wing of the JF-102A. The suction-pressure peaks at the leading edge are similar to those for the plane wing of the XF-92A (ref. 1). For $M \approx 1.02$ and 1.19, which are beyond the range of the data for the plane wing, appreciable suction pressures also occur, although the minimum pressure is generally near the base of the leading-edge camber rather than at the leading edge as for the subsonic Mach numbers.

Distribution of leading-edge pressures.- The favorable effect of leading-edge camber on the distribution of leading-edge pressures may

SECRET

be seen in figure 9 by comparing the cambered-wing distributions to the plane-wing distributions at similar wing stations and at moderate angles of attack. It is apparent that leading-edge camber distributes the suction pressures at the leading edge over a greater relative frontal area, thus increasing the suction force over that of the uncambered section. For clarity, the increased suction force is represented by the shaded area between the pressure distributions over the forward part of the wing sections.

H
1
1
6
From the thicknesswise distributions of figure 10 for the conically cambered wing, the favorable effects of camber are first apparent in the distributions at $\alpha \approx 6^\circ$. At $\alpha \approx 3^\circ$ and below, the pressures over most of the cambered part are greater than ambient, since the angle of attack of the leading edge is negative to the free stream. At $\alpha \approx 6^\circ$ the suction pressures are well developed over the leading edge of all the stations except the root station, $0b'/2$, which has no appreciable camber. The tip station, which has the greatest amount of camber, experiences the most favorable distribution of leading-edge pressures per unit chord. The tip-station distributions show that it is possible to distribute the suction pressures over a frontal projection more than twice the maximum thickness of the airfoil (4 percent for the JF-102A wing). At the high angles of attack obtained at $M \approx 0.70$ and 0.90 the magnitude of the suction pressures at the outboard wing sections is reduced as a result of flow separation associated with wing-section stall.

The favorable effects of leading-edge camber appear to continue to the supersonic speeds tested. At $M \approx 1.02$ and 1.19 the outboard suction-pressure coefficients at angles of attack between 6° and 9° (figs. 10(c) and (d)) are closer to a vacuum than for $M \approx 0.70$ and $\alpha = 9.0^\circ$ (fig. 10(a)). However, it should be mentioned that the angle of attack for cruise of most aircraft is generally below 3° at supersonic Mach numbers where, for the JF-102A wing, the effects of camber are not beneficial (figs. 10(c) and (d)). It was noted in reference 2 that benefits of both camber and twist on drag measurements diminish with increasing Mach number, becoming negligible when the Mach number component normal to the leading edge exceeded about 0.7. For the JF-102A airplane this is equivalent to a free-stream Mach number of 1.4, slightly higher than the range of the present investigation.

From the pressure distributions of figure 9 it would appear advantageous to camber the inboard sections of the wing also, even though the span-load distributions might not be elliptic. However, in this respect the results of reference 10 are of interest; drag reductions were obtained for swept wings by increasing the leading-edge radius. Essentially all the drag reduction was obtained by increasing the leading-edge radius at the outboard stations, which indicates that cambering the inboard leading edge would, similarly, have little effect on the



drag. In fact, figures 8 and 10 show that it may even be detrimental to camber the inboard sections because leading-edge suction does not become appreciable at these sections until higher angles of attack are reached. As a result, the leading-edge pressures at the inboard sections probably would be greater than ambient pressure at the moderate angles of attack at which leading-edge suction is desired; thus the drag would be increased.

Flow-Separation Characteristics

Leading-edge-separation vortex.- For thin wings with low aspect ratios and highly swept leading edges, the flow over the leading edge characteristically rolls up into a vortex, referred to as the leading-edge-separation vortex. The vortex originates near the wing tip and moves inboard along the leading edge with increasing angle of attack, trailing off the wing near the tip and predominating over the tip vortex. Flight data (ref. 1) showed the existence of the vortex at Mach numbers up to 0.93, and wind-tunnel results from references 6 and 11 show a vortex at supersonic speeds for both plane and cambered wings with subsonic leading edges.

H
1
1
6

In figure 8 the trough in the pressure distributions near the leading edge indicates the presence of a leading-edge-separation vortex for the cambered wing. The effects, however, are not as prominent as for the plane wing. The presence of the vortex is expected, even with leading-edge camber and fences, since experiments have shown that the vortex has considerable strength. However, the camber and fences apparently resist the formation of the vortex and delay its effect to higher angles of attack.

Wing-section stall.- The individual contributions of conical camber, fences, and reflexed tip cannot be determined from the data herein. The combined effect on the wing-section-stall characteristics is best evaluated by examining the section normal-force-coefficient curves of figure 4 and the comparison of the section normal-force coefficients of the cambered wing and the plane wing in figure 11. In figure 4 the high lifting efficiency of the two outermost wing sections is readily apparent. The comparatively high normal-force coefficients and angles of attack attained before the occurrence of section stall on the cambered wing are in contrast to the early loss in lift at the tip sections reported for the plane wing in reference 1 and shown in figure 11. The stalling of the tip sections of the plane wing at low angles of attack is a consequence of the formation of the leading-edge-separation vortex. Therefore, an important effect of the combination of camber, fences, and reflexed tip is to delay early flow separation at the outboard sections to higher angles of attack (above 8° , fig. 4).



The delay in flow separation at the outboard wing sections would be expected to have a favorable effect on the pressure drag. It is difficult to show this quantitatively by using the plane- and cambered-wing data because of the wing fences and the differences in the elevon position; however, figure 9 shows an indication of this source of drag reduction at $\alpha \approx 12^\circ$. The thicknesswise pressure distribution over the rear part of the plane and cambered wing sections shows a reduction in pressure drag for the cambered section as a result of the delay in flow separation.

H
1
1
6

Effect of outboard fence.- A noticeable effect of the outboard fence ($0.600b'/2$) on the wing sections just inboard of the fence may be noted in figure 4. At orifice station $0.584b'/2$ a large reduction in normal-force-curve slope occurs at an angle of attack of about 8° throughout the Mach number range tested. The pressure distributions in figure 8 show a reduction in loading at the leading edge between angles of attack of 8° and 10° . As the angle of attack increases above 12° , it becomes apparent that flow separation is occurring inboard of the fence extending eventually over the full chord, as indicated by the lack of pressure recovery at the trailing edge. The flow separation inboard of a wing fence has been shown to be a normal occurrence for fences on swept and delta wings (ref. 12); however, this undesirable effect is usually compensated by the contribution to the delay in flow separation outboard of the fences.

Span-Load Distributions

The span-load distributions in figure 12 show a wide variation in loading from a near-elliptic loading at the lower angles of attack to a near-triangular loading at the very high angles of attack. At moderate angles of attack, beginning at $\alpha \approx 9^\circ$ in figure 12, the effect of the wing fences on the loading is apparent. The outboard fence results in a significant reduction in loading on the inboard side as a result of the previously mentioned local-flow separation. This is contrary to the theoretical effect which, in the absence of flow separation, should be to increase the loading inboard and decrease the loading outboard (ref. 13). Some effect of the inboard fence is also noticeable, with the fence increasing the loading inboard and decreasing the loading outboard, as predicted by theory. At $\alpha \approx 24^\circ$ ($M \approx 0.70$) the fence effects are no longer noticeable as a result of extensive flow separation outboard of about $0.3b'/2$ (see also figs. 4(a) and 8(a)); consequently, the span loading is nearly triangular.

Since the basic purpose in distributing the leading-edge camber in a conical manner along the span is to obtain an elliptic span-load distribution at moderate angles of attack, the distributions from figure 12 at $\alpha \approx 7^\circ$ are compared to an elliptic distribution in figure 13. From



this figure it may be seen that the loading falls generally along the line for an ellipse. At Mach numbers below 1.19 the reflexed tip decreases the tip loading below the elliptic loading. As a result, the spanwise position of the center of pressure in figure 7(e) is about 2 percent farther inboard for subsonic Mach numbers than for $M \approx 1.19$.

In general, the distributions in figure 12 at $M \approx 0.70$ do not differ greatly from those for a plane wing at low and high angles of attack, as can be seen in figure 14. At $\alpha \approx 9^\circ$ and 13° the previously mentioned delay in flow separation for the cambered wing results in slightly larger loads in the tip region than for the plane wing.

In reference 14 the span-load distributions of the JF-102A were compared to those predicted by linear theory for a flat-plate wing of the same plan form. The distributions compared well at the lower angles of attack, primarily because theory predicts a near-elliptic loading for plane triangular wings. At high angles of attack the comparison breaks down because of flow separation, the effect of which can be seen at $\alpha \approx 24^\circ$ in figure 14 herein. Using the theory in reference 15, which accounts for the vortex at the leading edge, and correcting for elevon deflection by the method of reference 16, the results are still unsatisfactory. However, this theory is for wings of very low aspect ratio and, apparently, should not be applied for any other case. For moderate aspect ratios there does not appear to be a method available that will predict the effects of the leading-edge-separation vortex.

H
1
1
6

CONCLUDING REMARKS

Pressure measurements were made in flight over the conically cambered delta wing of the Convair JF-102A airplane at Mach numbers up to 1.19. Maximum angles of attack tested ranged from 24° at a Mach number of 0.70 to 9° at 1.19.

Appreciably large suction pressures are realized at the leading edge of the conically cambered delta wing similar in magnitude to the high suction pressures experienced by thin, plane, delta wings. The cambered leading edge is effective in distributing the low pressures at the leading edge over a greater frontal area, thus increasing the leading-edge thrust. The conical distribution of camber results in near-elliptic span-load distributions at the lower angles of attack; however, a more important effect of conical camber (together with the wing fences and reflexed tips incorporated by the JF-102A) is the delay to higher angles of attack in the occurrence of flow separation that normally occurs on a plane delta wing. A favorable effect on the pressure drag may also be attributed to the delay in flow separation. Although the outboard wing fence probably contributes to the delay in

~~CONFIDENTIAL~~

flow separation at the tip, the pressures indicate that the fence induces flow separation inboard of the fence starting near the leading edge at angles of attack of about 8° and extending to the trailing edge as the angle of attack increases.

A wide variation occurs in the span-load distributions from a near-elliptic loading at the lower angles of attack to a near-triangular loading at the very high angles of attack tested. In general, the distributions are similar to those of a plane wing, although the delay in flow separation in the tip region results in slightly larger tip loads.

High-Speed Flight Station,
National Aeronautics and Space Administration,
Edwards, Calif., May 5, 1959.

H
1
1
6

REFEREN**CE**S

1. Keener, Earl R., and Jordan, Gareth H.: Wing Pressure Distributions Over the Lift Range of the Convair XF-92A Delta-Wing Airplane at Subsonic and Transonic Speeds. NACA RM H55G07, 1955.
2. Hall, Charles F.: Lift, Drag, and Pitching Moment of Low-Aspect-Ratio Wings at Subsonic and Supersonic Speeds. NACA RM A53A30, 1953.
3. Jones, Robert T.: Estimated Lift-Drag Ratios at Supersonic Speed. NACA TN 1350, 1947.
4. Boyd, John W., Migotsky, Eugene, and Wetzell, Benton E.: A Study of Conical Camber for Triangular and Swept-Back Wings. NACA RM A55G19, 1955.
5. Saltzman, Edwin J., Bellman, Donald R., and Musialowski, Norman T.: Flight-Determined Transonic Lift and Drag Characteristics of the YF-102 Airplane With Two Wing Configurations. NACA RM H56E08, 1956.
6. Mugler, John P., Jr.: Pressure Measurements at Transonic and Low Supersonic Speeds on a Thin Conical Cambered Low-Aspect-Ratio Delta Wing in Combination With Basic and Indented Bodies. NACA RM L57G19, 1957.
7. Mugler, John P., Jr.: Analysis of Pressure Data Obtained at Transonic Speeds on a Thin Low-Aspect-Ratio Cambered Delta Wing-Body Combination. NACA RM L58F24, 1958.
8. Phelps, E. Ray: Pressure Distributions at Mach Numbers of 1.6 and 1.9 of a Conically Cambered Wing of Triangular Plan Form With and Without Pylon-Mounted Engine Nacelles. NACA RM A56B03, 1956.
9. Huston, Wilber B.: Accuracy of Airspeed Measurements and Flight Calibration Procedures. NACA Rep. 919, 1948.
10. Evans, William T.: Leading-Edge Contours for Thin Swept Wings: An Analysis of Low- and High-Speed Data. NACA RM A57B11, 1957.
11. Spahr, J. Richard, and Dickey, Robert R.: Wind-Tunnel Investigation of the Vortex Wake and Downwash Field Behind Triangular Wings and Wing-Body Combinations at Supersonic Speeds. NACA RM A53D10, 1953.

12. Haines, A. B., and Rhodes, C. W.: Tests in the R.A.E. 10 Ft. x 7 Ft. High Speed Tunnel on a 7.5% Thick, 50° Swept Wing Fitted With Stall Fences and a Leading-Edge Chord-Extension. Tech. Note No. Aero 2521, British R.A.E., Sept. 1954.
13. Weber, J.: Theoretical Load Distribution on a Wing With Vertical Plates. R. & M. No. 2960, British A.R.C., 1956. (Supersedes R.A.E. Aero 2500, Mar. 1954.)
14. Malvestuto, Frank S., Cooney, Thomas V., and Keener, Earl R.: Flight Measurements and Calculations of Wing Loads and Load Distributions at Subsonic, Transonic, and Supersonic Speeds. NACA RM H57E01, 1957.
15. Brown, Clinton E., and Michael, William H., Jr.: On Slender Delta Wings With Leading-Edge Separation. NACA TN 3430, 1955.
16. Diederich, Franklin W., and Zlotnick, Martin: Calculated Spanwise Lift Distributions and Aerodynamic Influence Coefficients for Swept Wings in Subsonic Flow. NACA TN 3476, 1955.

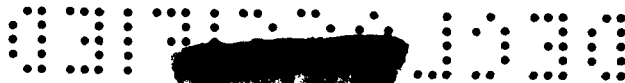


TABLE I

TABLE OF PHYSICAL CHARACTERISTICS

Wing:	
Total area, sq ft	695.05
Span (actual), ft	38.17
Airfoil section	NACA 0004-65 (Modified)
Conical camber, percent local semispan	6.3
Mean aerodynamic chord, ft	23.76
Aspect ratio	2.08
Root chord, ft	35.63
Tip chord, ft	0.81
Taper ratio	0.023
Sweep at leading edge, deg	60.1
Sweep at trailing edge, deg	-5
Incidence, deg	0
Dihedral (uncambered chord line), deg	0
Geometric twist, deg	0
Tip reflex, deg	-6
Wing panel (outboard of wing station 3.542 ft) -	
Area (one panel) sq ft	232.50
Span (one panel), ft	15.52
Mean aerodynamic chord (wing station 8.210 ft), ft	20.64
Elevons:	
Area (total, rearward of hinge line), sq ft	67.2
Span (one elevon), ft	12.89
Vertical tail:	
Airfoil section	NACA 0004-65 (Modified)
Area (above waterline 33), sq ft	68.3
Aspect ratio	1.1
Sweepback of leading edge, deg	60.0
Sweepback of trailing edge, deg	-5
Fuselage:	
Length, ft	63.3
Maximum diameter, ft	6.5
Equivalent-body fineness ratio	9.1
Power plant:	
Installed static thrust at sea level, lb	8,800
Installed static thrust at sea level (with afterburner), lb	13,200
Test center-of-gravity location, percent mean aerodynamic chord	28 to 29



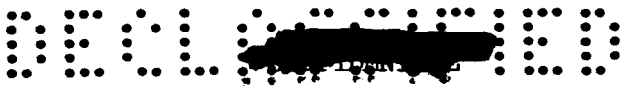


TABLE II
LOCATIONS OF STATIC-PRESSURE ORIFICES
[Stations and ordinates, percent chord]

0 b'/2		0.168 b'/2		0.320 b'/2		0.441 b'/2		0.584 b'/2		0.713 b'/2		0.851 b'/2	
Station	Ordnate	Station	Ordnate	Station	Ordnate	Station	Ordnate	Station	Ordnate	Station	Ordnate	Station	Ordnate
Upper surface													
0	-0.314	2.5	-.595	0	-0.934	2.5	.130	0	-2.081	2.5	-1.688	0	-6.919
0.5	.217	5.0	.848	0.5	-.307	5.0	.616	0.5	-1.367	5.0	-.849	2.5	-5.016
1.0	.380	9.0	1.090	1.0	-.054	7.5	.866	1.0	-1.096	10.0	-.354	5.0	-4.006
2.0	.583	10.0	1.138	2.0	-.138	9.3	1.011	2.0	-.674	15.0	.951	10.0	-2.185
3.0	.717	13.4	1.275	3.0	-.556	13.2	1.166	3.0	-.333	23.7	1.380	15.0	-.761
4.0	.809	15.0	1.333	4.0	-.664	15.0	1.271	4.0	-.046	30.0	1.539	20.0	-.298
5.0	.892	20.0	1.500	6.0	-.855	20.0	1.442	6.0	.383	40.0	1.716	29.4	1.291
7.5	1.054	25.0	1.623	7.9	-.976	24.8	1.567	8.0	.674	50.0	1.800	42.9	1.589
11.1	1.220	30.0	1.722	10.8	1.121	29.8	1.677	10.0	.872	60.0	1.809	52.9	1.688
12.5	1.277	34.8	1.798	12.5	1.204	35.0	1.757	12.0	1.017	71.8	1.688	61.3	1.887
15.0	1.369	40.6	1.866	15.3	1.320	40.0	1.822	17.1	1.262	79.0	1.446	70.0	2.715
20.1	1.526	45.2	1.903	20.0	1.474	45.0	1.867	20.0	1.354	80.0	1.399	80.0	3.526
25.0	1.640	50.1	1.924	25.0	1.598	50.0	1.892	25.0	1.499	85.0	1.100	91.0	3.989
30.0	1.737	55.0	1.927	30.0	1.702	55.0	1.897	30.0	1.605	90.0	.755	95.0	4.138
35.0	1.815	60.0	1.914	35.0	1.777	60.0	1.887	35.0	1.691	95.6	.364		
40.0	1.875	65.0	1.873	40.0	1.843	65.0	1.847	40.0	1.764				
45.0	1.917	70.1	1.780	45.0	1.889	70.7	1.752	45.0	1.810				
50.3	1.935	75.0	1.634	50.0	1.910	74.9	1.627	50.0	1.836				
55.7	1.935	80.0	1.398	55.0	1.914	83.0	1.211	55.0	1.843				
60.8	1.917	86.8	.947	60.0	1.901	87.5	.906	58.3	1.843				
65.0	1.880	89.1	.783	65.0	1.864	90.0	.731	66.1	1.797				
70.0	1.789	90.0	.721	70.0	1.777	92.5	.556	70.0	1.731				
75.0	1.635	92.0	.581	75.2	1.615	94.5	.415	75.0	1.599				
81.4	1.312	94.0	.441	79.9	1.399	97.6	.195	85.2	1.063				
85.0	1.069	96.0	.301	84.5	1.121			87.0	.938				
88.4	.829	98.4	-.133	87.9	.876			90.0	.733				
90.1	.709			88.5	.830			94.8	.403				
91.0	.646			90.0	.722			97.0	.244				
93.0	.506			93.0	.516								
95.0	.366			96.0	.303								
97.0	.226			98.0	.162								
98.6	.112												
Lower surface													
0.5	-0.403	2.5	-.677	0.5	-1.017	2.5	-1.286	0.5	-2.219	2.5	-3.329	2.5	-6.820
1.0	-.440	5.0	-.762	1.0	-1.009	5.0	-1.076	1.0	-2.219	5.0	-2.816	5.0	-6.191
2.0	-.500	9.0	-1.039	2.0	-.967	7.5	-.991	2.0	-2.100	10.0	-1.977	10.0	-4.767
3.0	-.568	10.0	-1.104	3.0	-.897	9.3	-1.021	3.0	-1.942	15.0	-1.473	15.0	-3.476
4.0	-.646	13.4	-1.268	4.0	-.872	13.2	-1.156	4.0	-1.790	23.7	-1.380	20.0	-2.400
5.0	-.734	15.0	-1.333	6.0	-.868	15.0	-1.271	6.0	-1.506	30.0	-1.539	29.4	-1.440
7.5	-.969	20.0	-1.500	7.9	-.922	20.0	-1.442	8.0	-1.368	40.0	-1.716	42.9	-1.589
11.1	-1.197	25.0	-1.623	10.8	-1.100	24.8	-1.567	10.0	-1.189	50.0	-1.800	52.9	-1.688
11.9	-1.260	30.0	-1.722	12.5	-1.191	29.8	-1.677	11.7	-1.143	60.0	-1.809	61.3	-1.556
15.0	-1.366	34.8	-1.798	15.3	-1.312	35.0	-1.757	18.3	-1.328	71.8	-1.688	70.0	-.613
20.1	-1.526	40.6	-1.866	20.0	-1.474	40.0	-1.822	20.7	-1.420	79.0	-1.446	80.0	.712
24.5	-1.640	45.2	-1.903	25.0	-1.598	45.0	-1.867	25.0	-1.539	80.0	-1.399	91.0	2.500
30.0	-1.737	50.1	-1.924	30.0	-1.702	50.0	-1.892	30.0	-1.645	85.0	-1.100	94.6	3.178
35.0	-1.815	55.0	-1.927	35.0	-1.777	55.0	-1.897	35.0	*-2.642	90.0	-.755		
39.6	-1.875	60.0	-1.914	40.0	-1.843	60.0	-1.887	40.0	*-3.230	95.6	-.364		
45.0	-1.917	65.0	-1.873	45.0	-1.889	65.0	-1.847	45.0	*-3.673				
50.3	-1.935	70.1	-1.780	50.0	-1.910	70.7	-1.752	50.0	*-4.075				
55.7	-1.935	75.0	-1.634	55.0	-1.914	74.9	-1.627	55.0	*-4.426				
60.8	-1.917	80.0	-1.398	60.0	-1.901	83.0	-1.211	60.0	*-4.723				
65.0	-1.880	86.8	-.950	65.0	-1.864	87.5	-.906	65.0	*-5.000				
70.0	-1.789	89.1	-.783	70.0	-1.777	90.0	-.731	70.0	*-5.284				
75.0	-1.635	90.0	-.721	74.9	-1.615	92.5	-.556	75.0	*-5.542				
81.4	-1.312	92.0	-.581	80.0	-1.399	94.5	-.415	85.0	*-5.040				
85.0	-1.069	94.0	-.441	85.1	-1.063	97.6	-.195	87.0	*-4.346				
88.4	-.828	96.0	-.301	87.9	-.876			90.0	*-3.237				
90.1	-.709	98.4	-.133	88.5	-.830			94.9	*-1.632				
91.0	-.646			90.0	-.722			97.0	*-.912				
93.0	-.506			93.0	-.516								
95.0	-.366			96.0	-.303								
97.0	-.226			98.0	-.162								
98.6	-.112												

*Orifices located on surface of elevator-actuator fairing.

H-116



TABLE III

FLIGHT CONDITIONS AT WHICH PRESSURE DISTRIBUTIONS WERE OBTAINED

M	α , deg	δ_e , deg	M	α , deg	δ_e , deg
$M \approx 0.55$			$M \approx 0.95$		
0.53	7.0	1.6 up	0.95	-0.5	1.5 down
.51	8.2	2.0	.95	6.1	.4 up
.59	26.1	12.2	.95	7.4	2.0
.56	27.4	†11.0	.95	9.5	4.6
$M \approx 0.70$			$M \approx 0.98$		
*0.70	3.0	0.4 up	0.98	3.8	0.5 down
*.70	3.8	.5	.98	6.0	4.0 up
*.70	4.7	.6	.98	8.7	6.9
.70	7.3	.9	.99	10.1	8.7
.70	9.0	1.4	.97	10.8	†8.7
*.70	9.9	2.1	$M \approx 1.02$		
.69	11.7	2.4	*1.02	1.0	1.4 down
.66	13.1	3.9	*1.02	2.0	1.3
.74	15.7	5.3	1.02	3.9	.9 up
.73	18.5	7.6	1.02	6.4	4.5
.69	22.2	10.9	1.02	7.6	5.9
.68	23.7	†9.6	1.02	8.8	8.0
$M \approx 0.80$			1.02	9.4	8.4
0.82	5.2	1.5 up	$M \approx 1.10$		
.82	6.4	2.1	1.11	1.2	2.2 down
.82	8.9	2.3	1.11	1.7	.9
.80	10.5	3.1	1.12	2.8	.6 up
.80	12.0	3.9	1.12	4.3	3.1
.81	13.0	4.5	1.10	5.0	4.8
.80	14.5	5.7	1.12	6.0	6.8
.80	17.8	†4.4	1.11	6.8	7.6
.80	20.6	8.6	1.08	7.4	7.9
$M \approx 0.90$			1.08	8.7	9.9
0.90	-1.0	1.7 down	1.07	9.2	10.3
*.90	.1	1.1	$M \approx 1.19$		
*.90	1.1	1.0	1.19	0.7	1.1 down
*.90	2.0	1.0	1.19	3.1	2.5 up
*.90	2.9	.7	1.19	7.0	9.7
*.90	3.9	.6 up	1.18	8.6	11.1
.89	5.1	.5			
.92	6.9	1.4			
.92	9.0	†1.5			
.88	9.7	3.3			
.89	11.3	†2.3			
.90	12.7	3.9			
.90	17.9	10.3			

* Corrected for pressure lag.

† $\delta_e < \delta_e$ for trim.

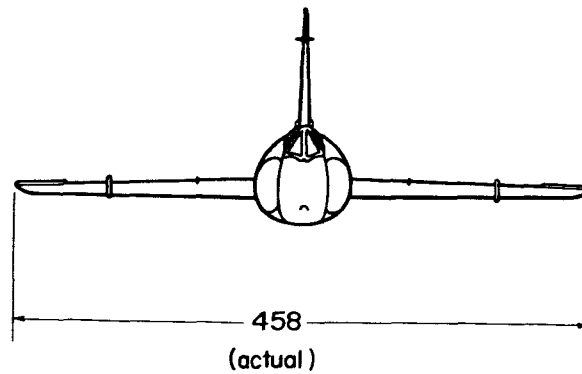
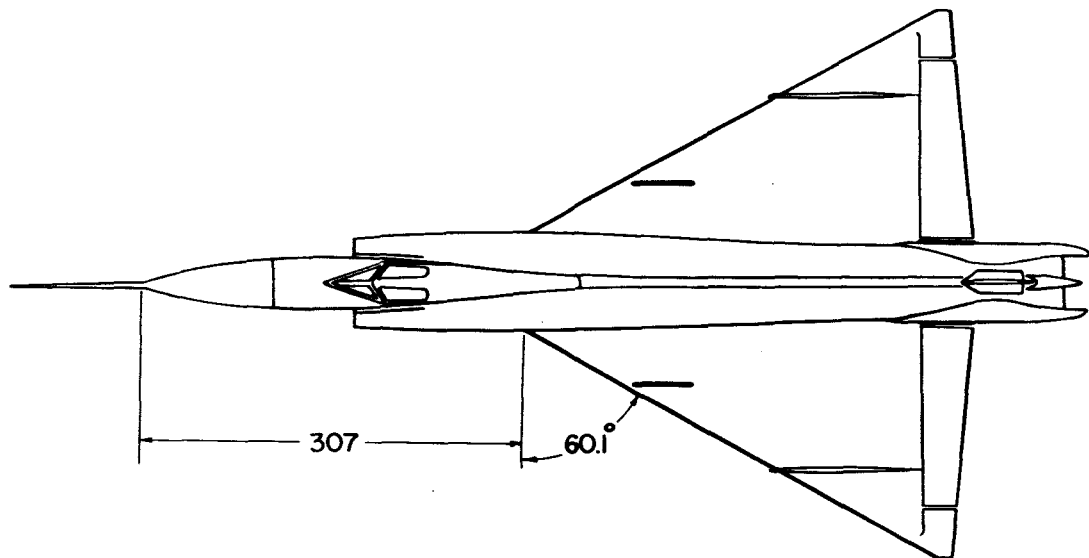
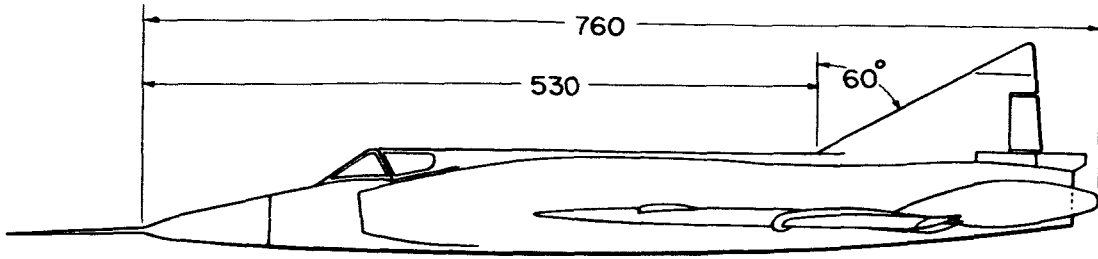
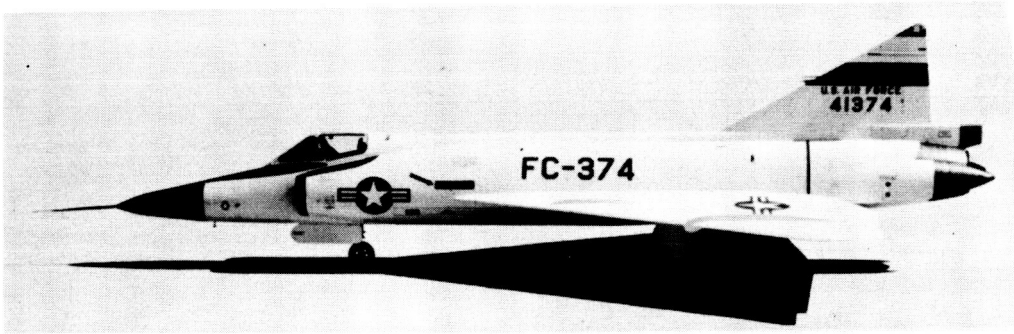


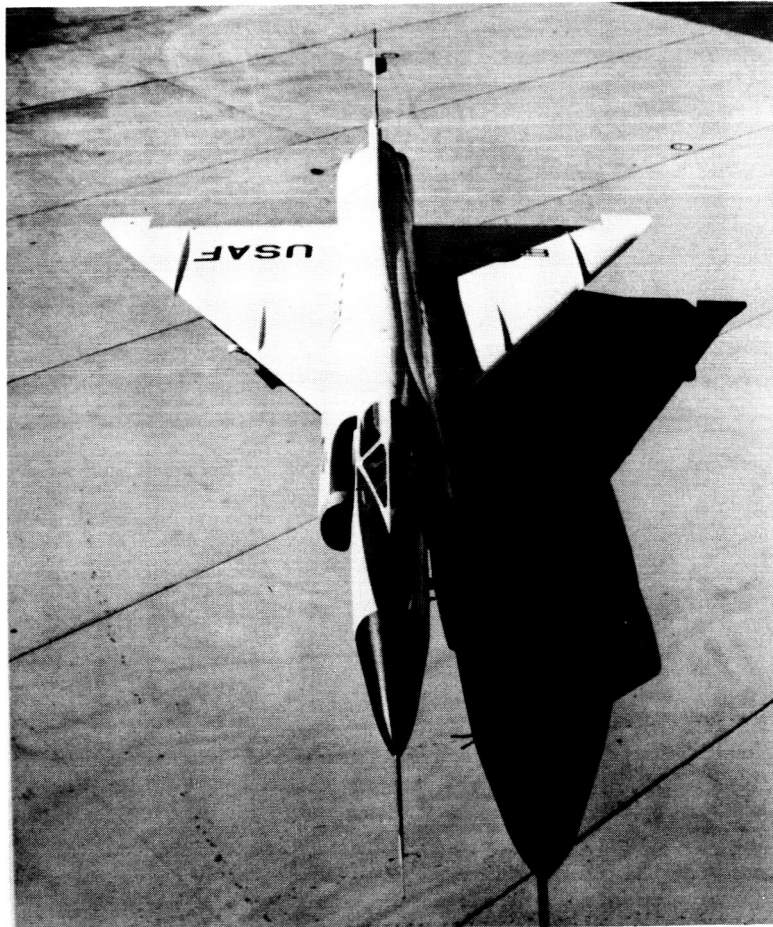
Figure 1.- Three-view drawing of the airplane. All dimensions in inches.

H-116

~~CONFIDENTIAL~~



E-2554

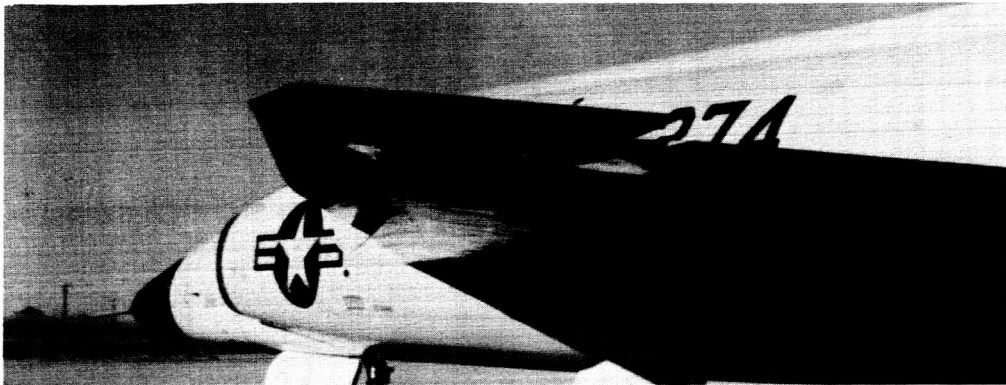


(a) Complete airplane; side and overhead views. E-2551

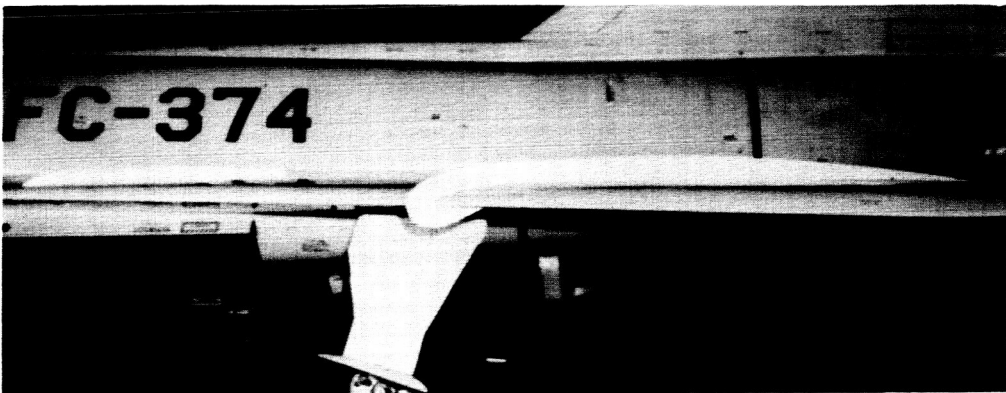
Figure 2.- Photographs of the JF-102A airplane.

~~CONFIDENTIAL~~

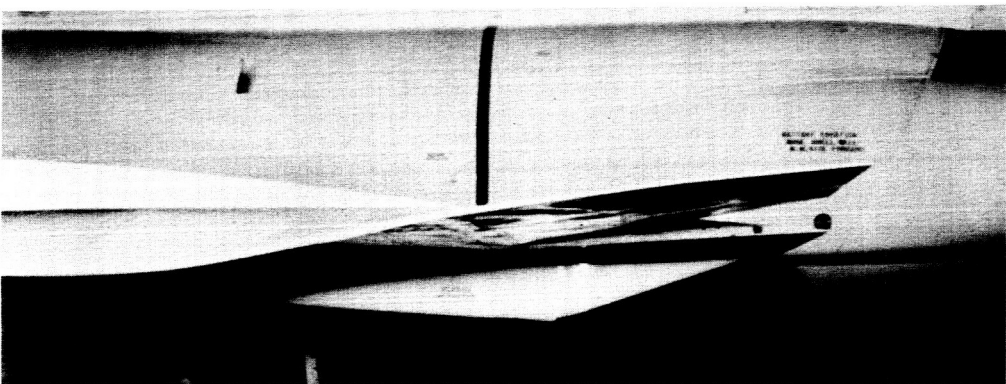
H-116
911-H



E-4246



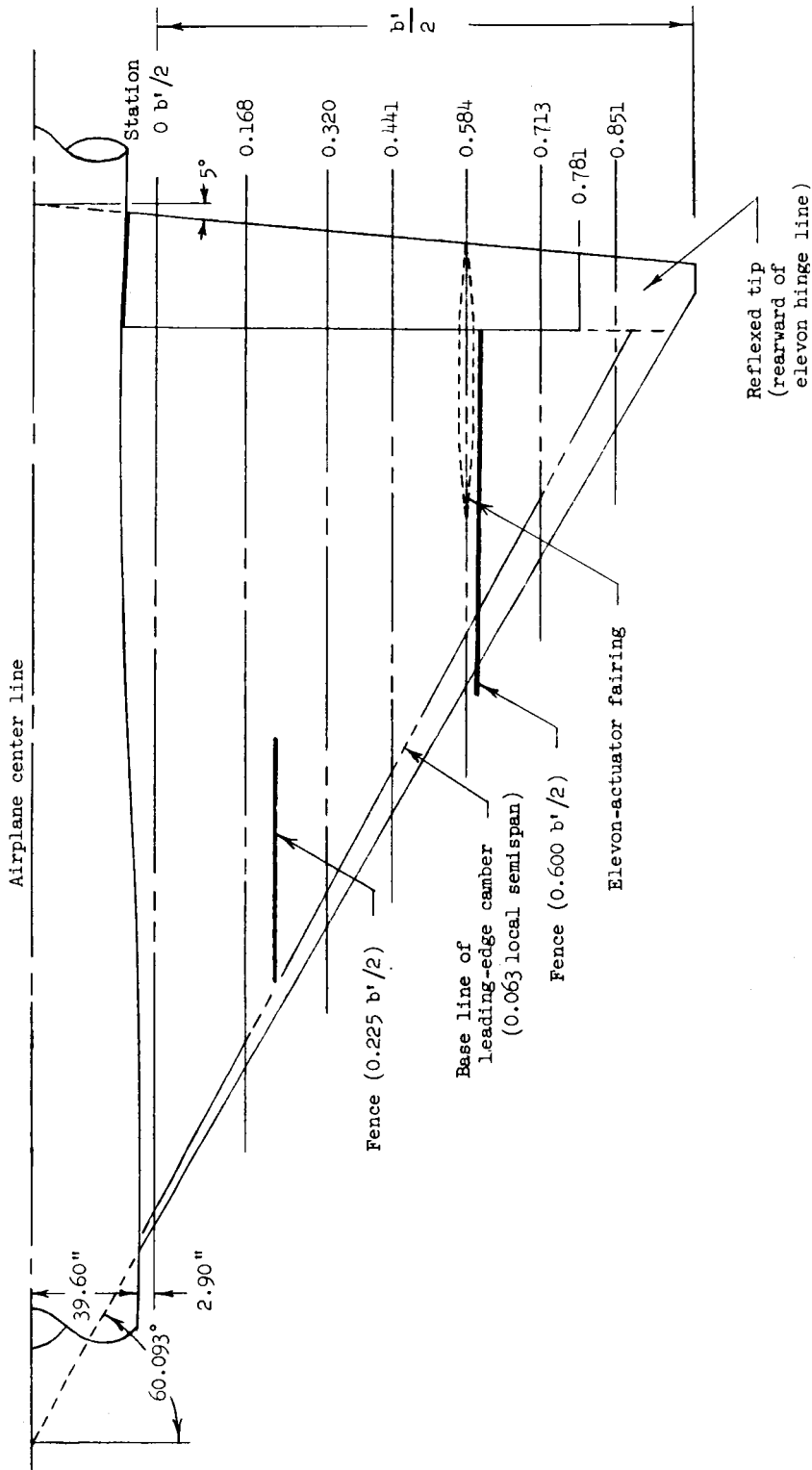
E-4244



(b) Close-up views of wing showing leading-edge camber, fences, reflexed tip, and elevon actuator fairing. ^{E-4245}

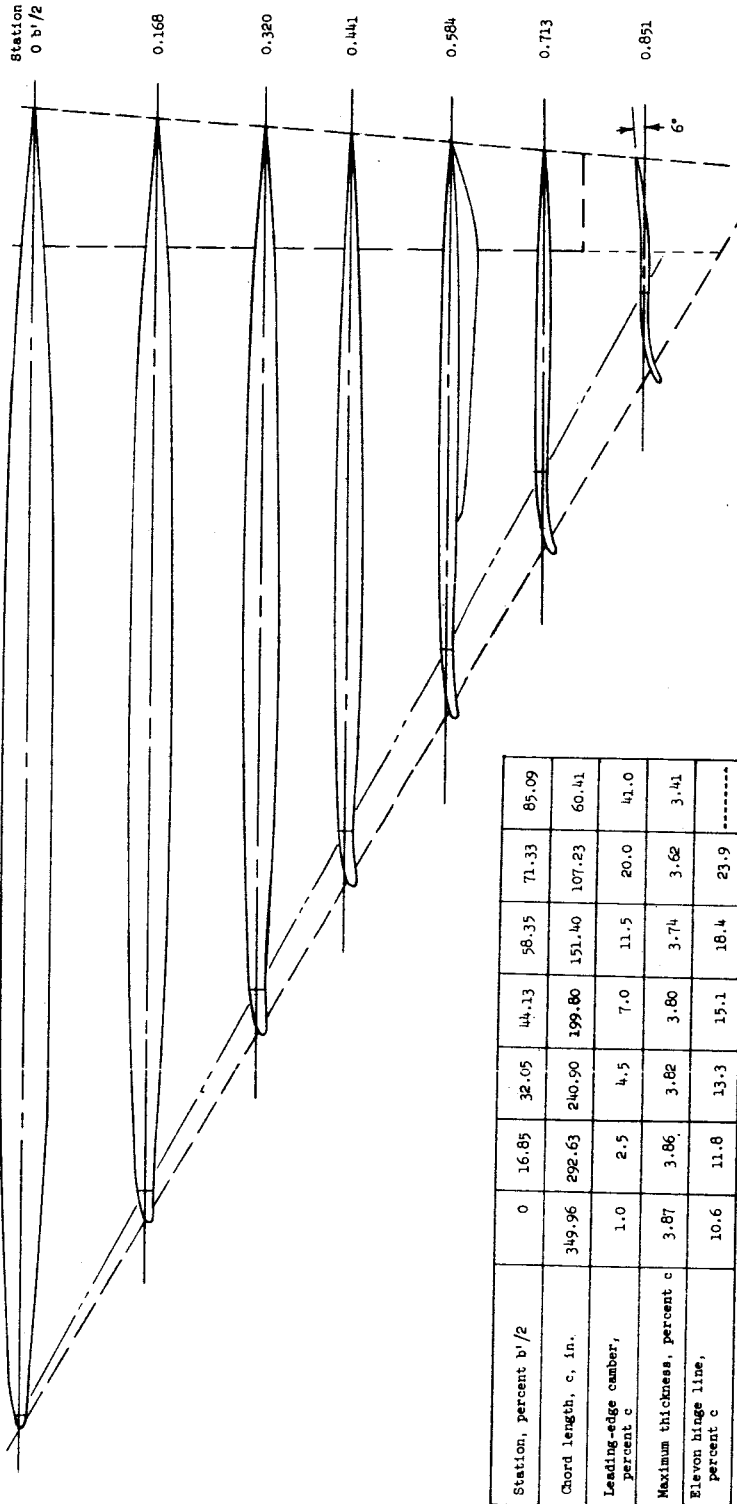
Figure 2.- Concluded.

H-116



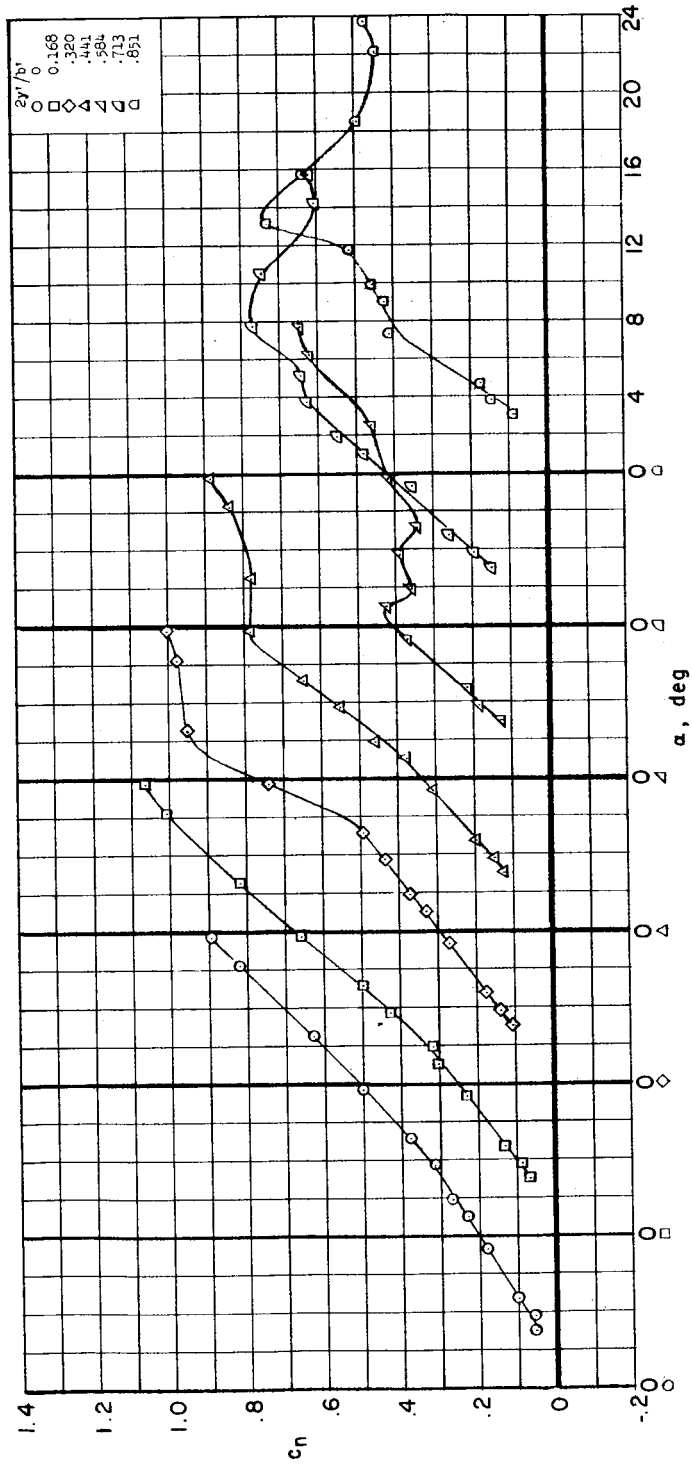
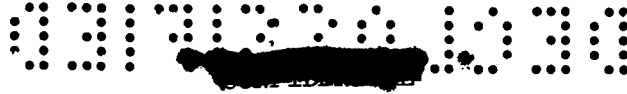
(a) Spanwise location of orifice stations.

Figure 3.- Drawing of left wing.



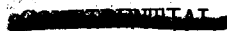
(b) Cross-sectional views at each orifice station.

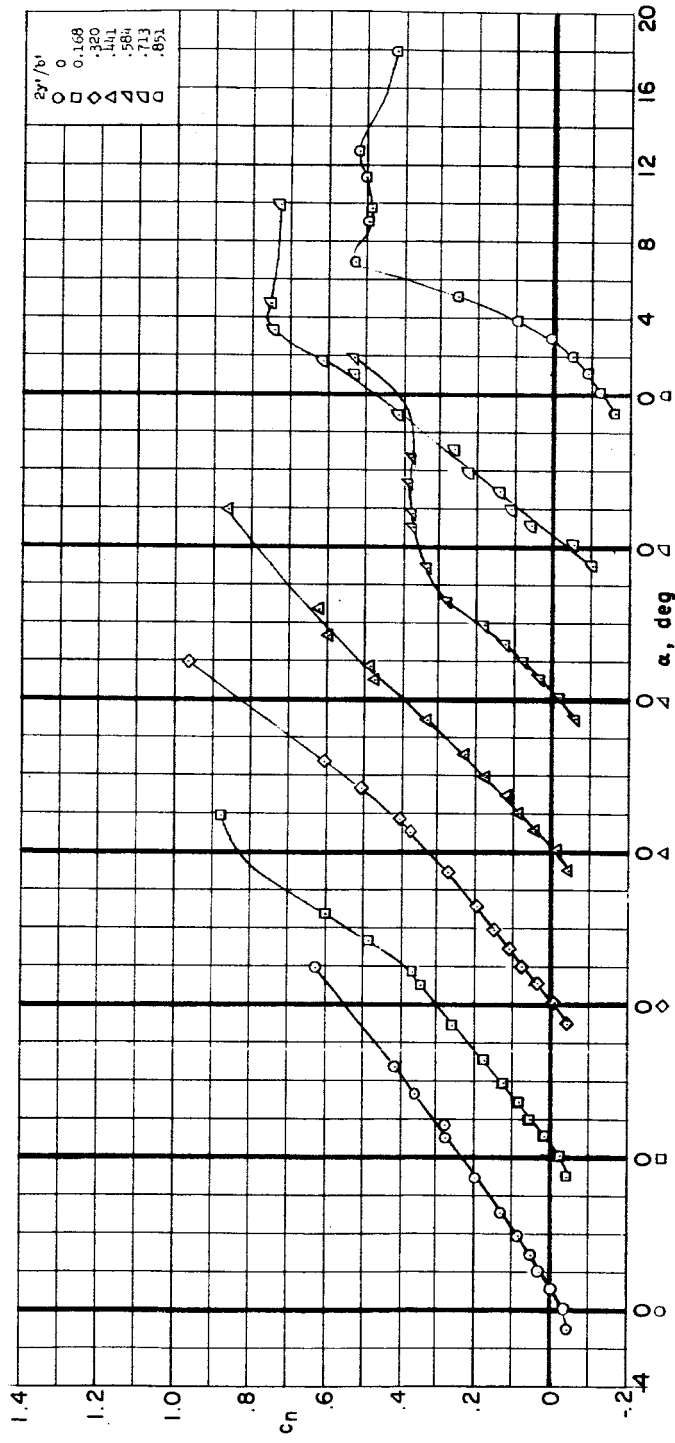
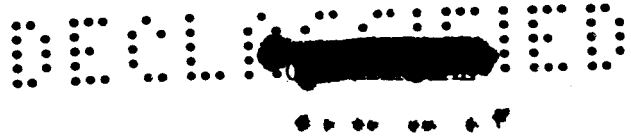
Figure 3.- Concluded.



(a) $M \approx 0.70$.

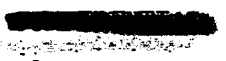
Figure 4.- Wing-section normal-force characteristics for the JF-102A airplane.

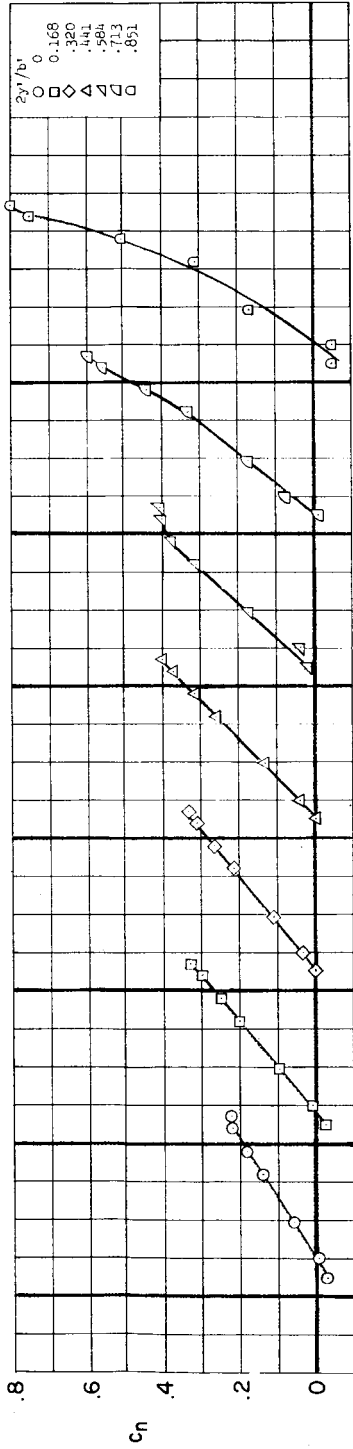
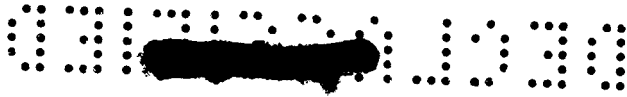




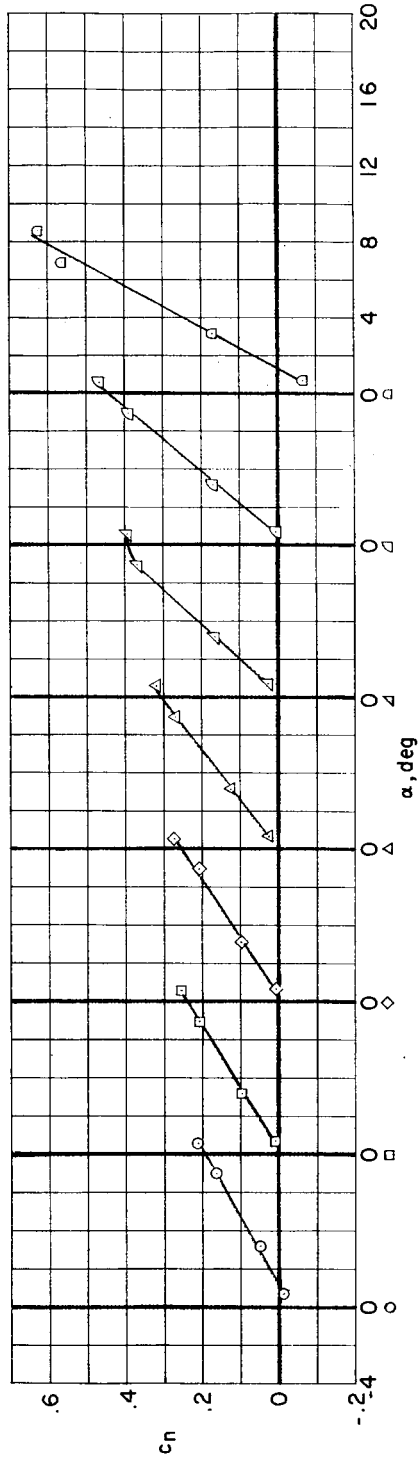
(b) $M \approx 0.90$.

Figure 4.- Continued.



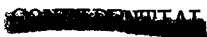


(c) $M \approx 1.02$.

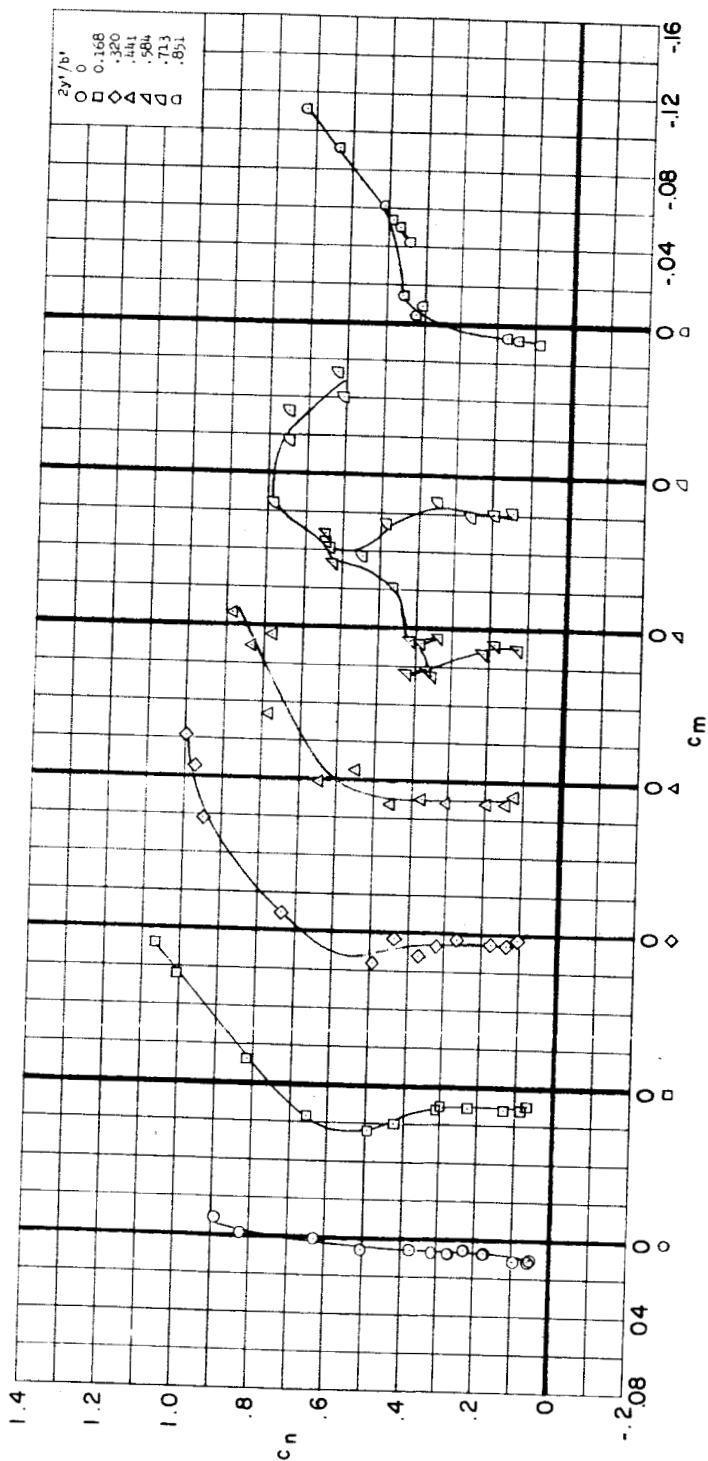


(d) $M \approx 1.19$.

Figure 4.- Concluded.



CONFIDENTIAL

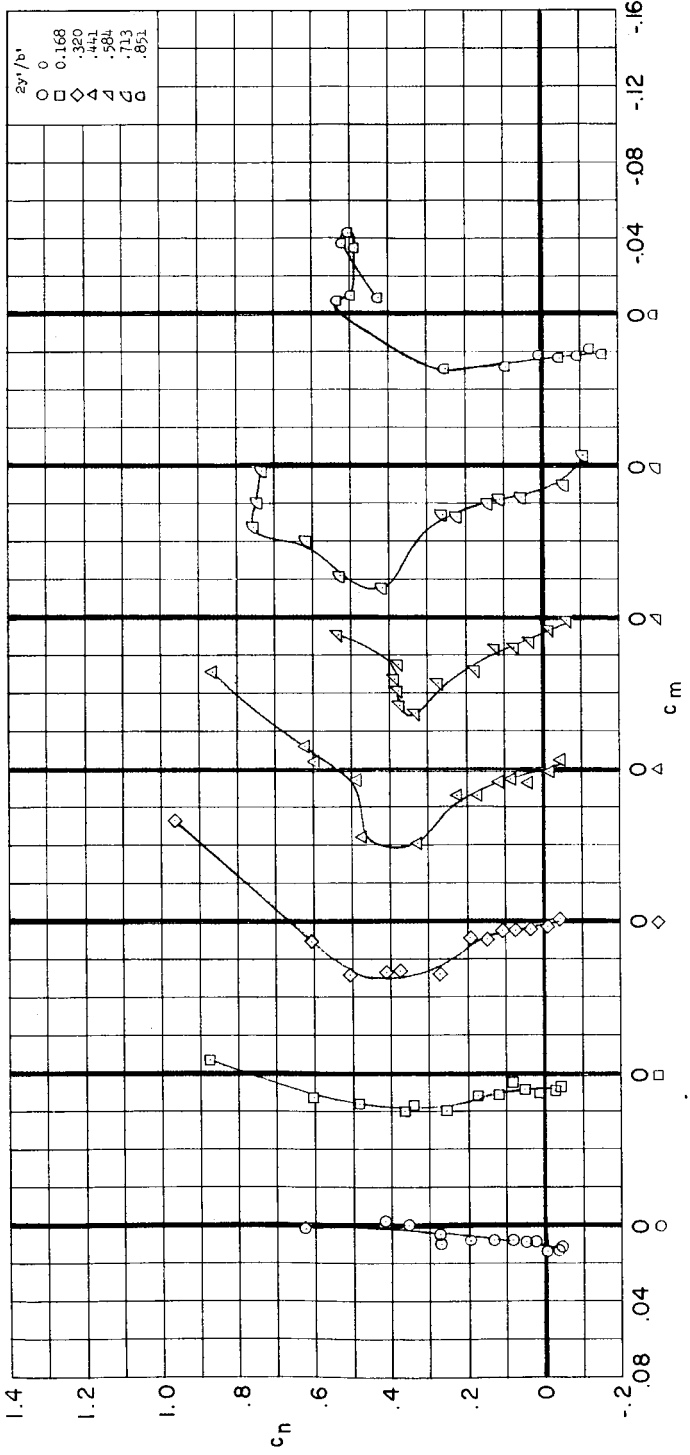


(a) $M \approx 0.70$.

Figure 5.- Wing-section pitching-moment characteristics for the JF-102A airplane.

CONFIDENTIAL

CONFIDENTIAL



(b) $M \approx 0.90$.

Figure 5.- Continued.

H-1116

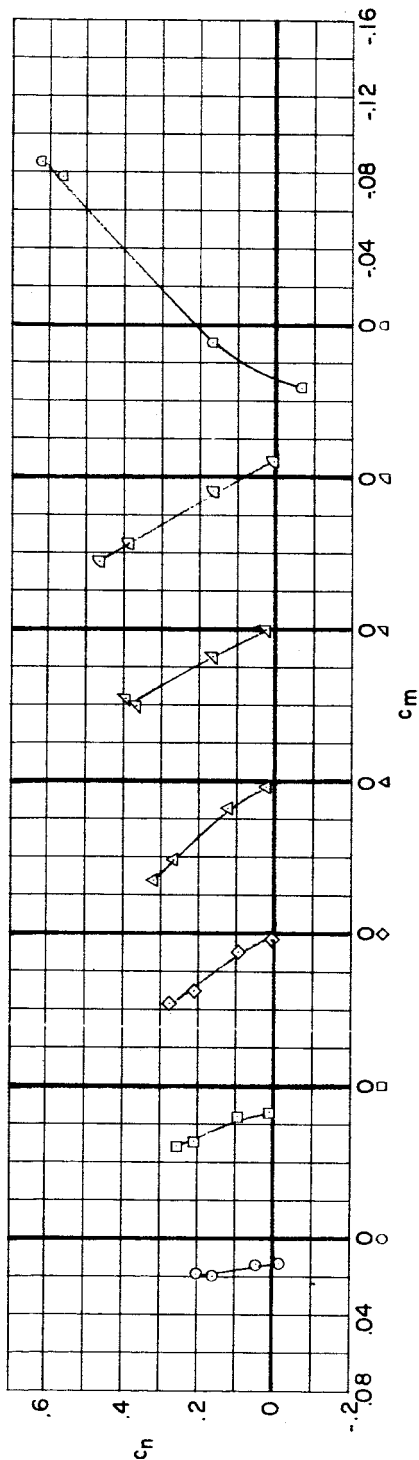
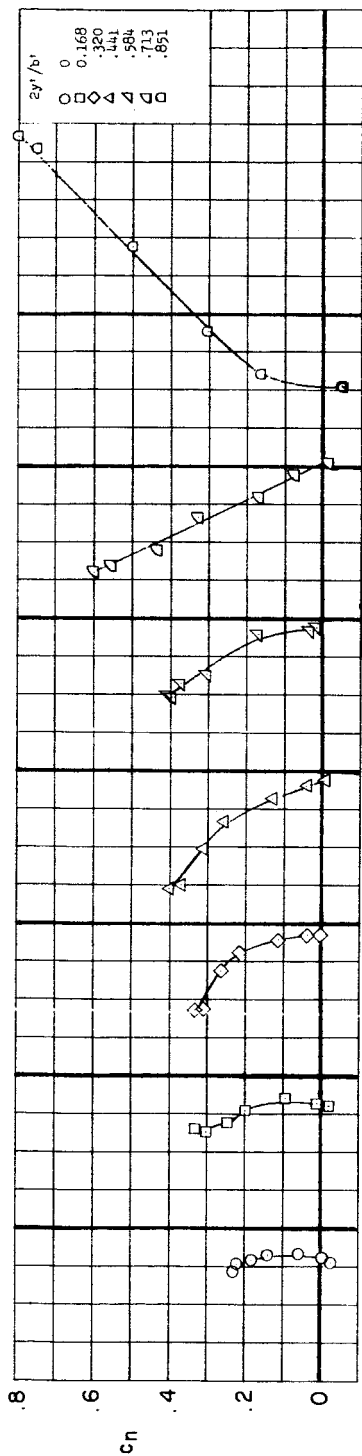
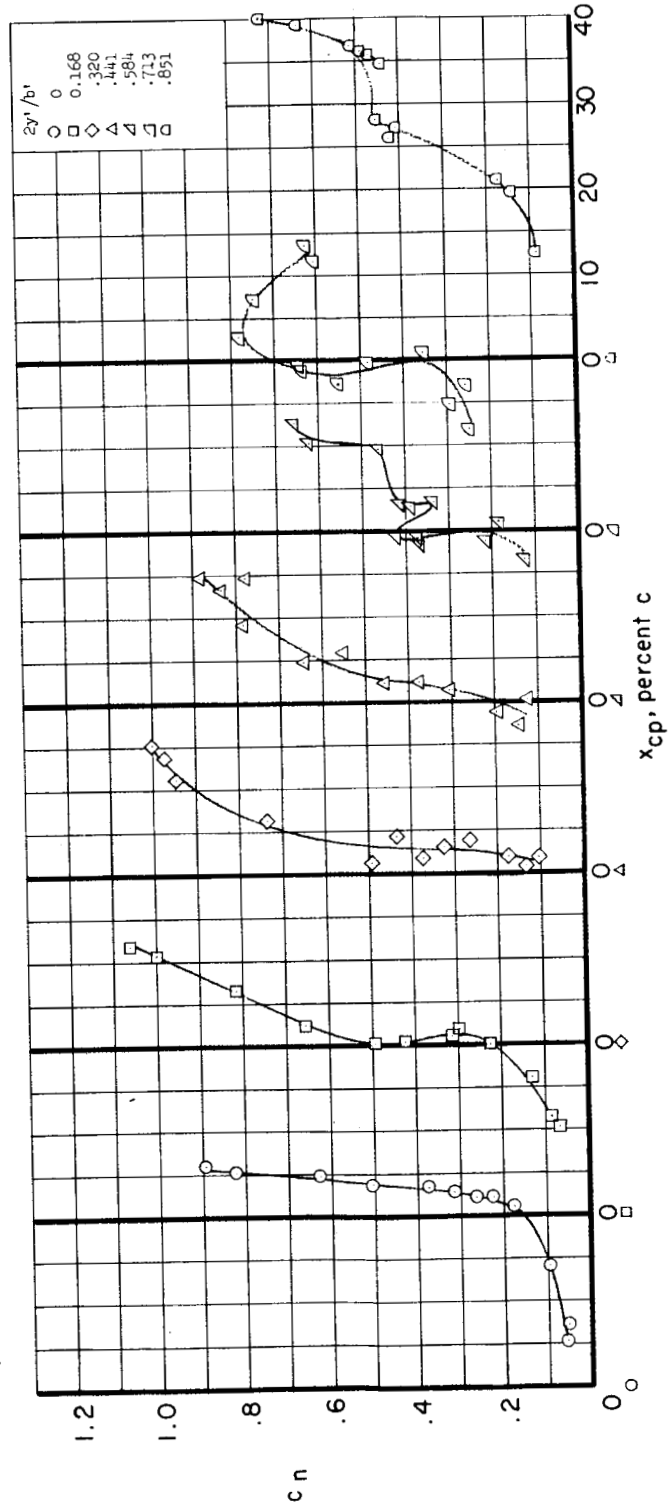


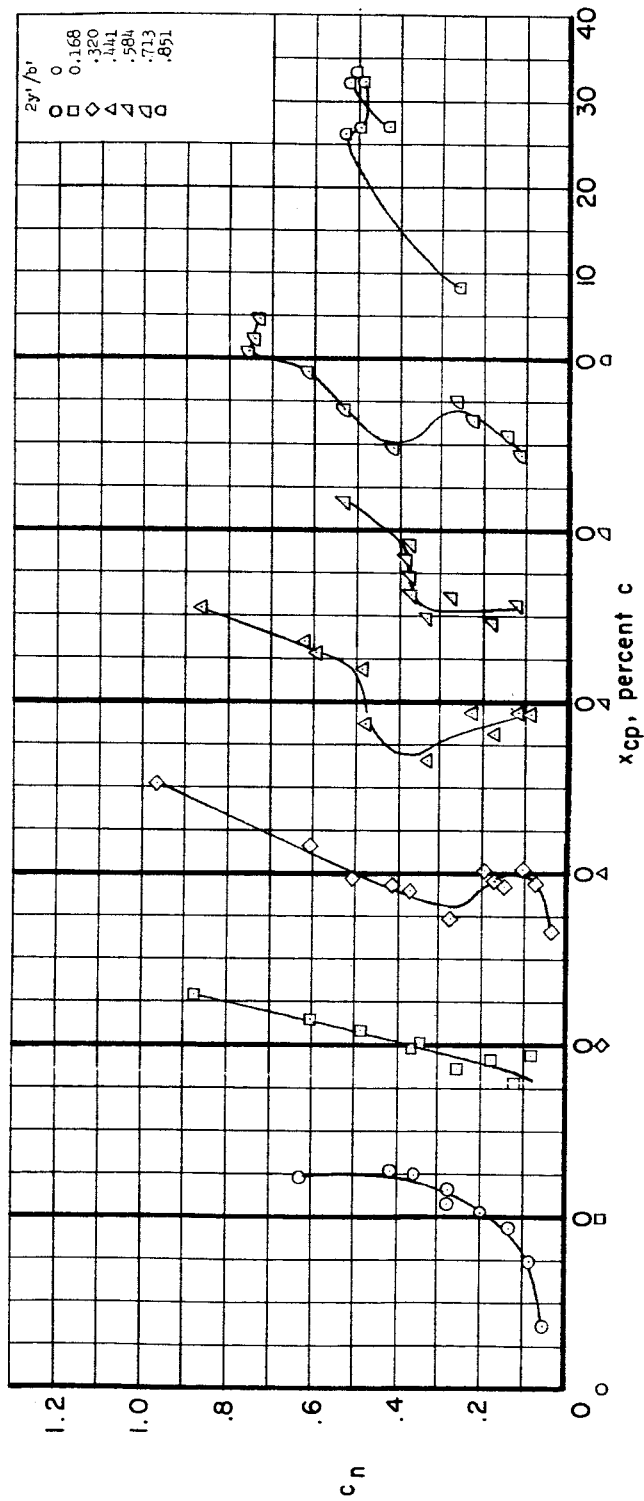
Figure 5.- Concluded.

CONFIDENTIAL



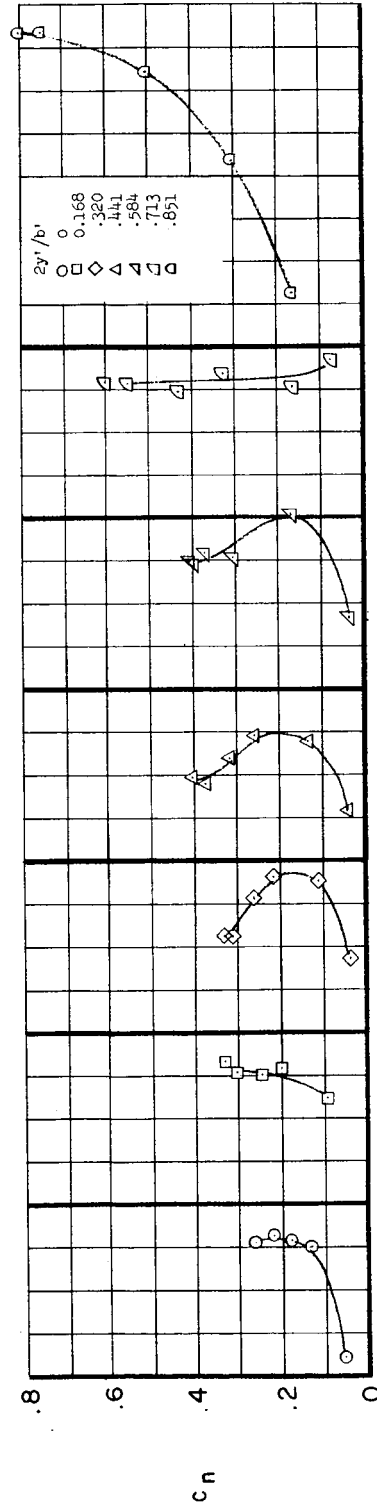
(a) $M \approx 0.70$.

Figure 6.- Wing-section center-of-pressure characteristics for the JF-102A airplane.

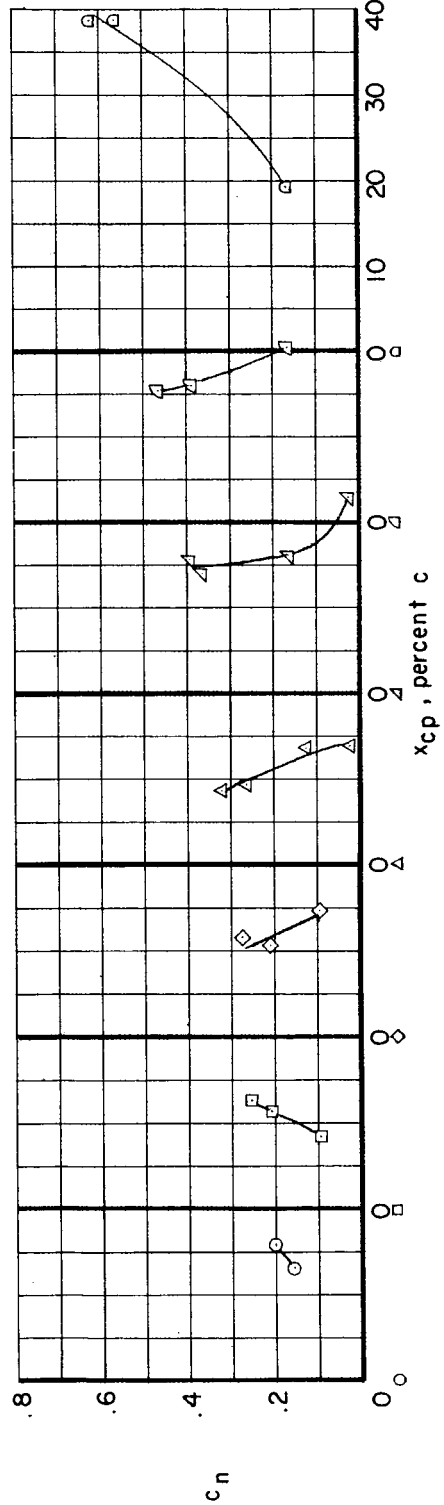


(b) $M \approx 0.90$.

Figure 6.- Continued.

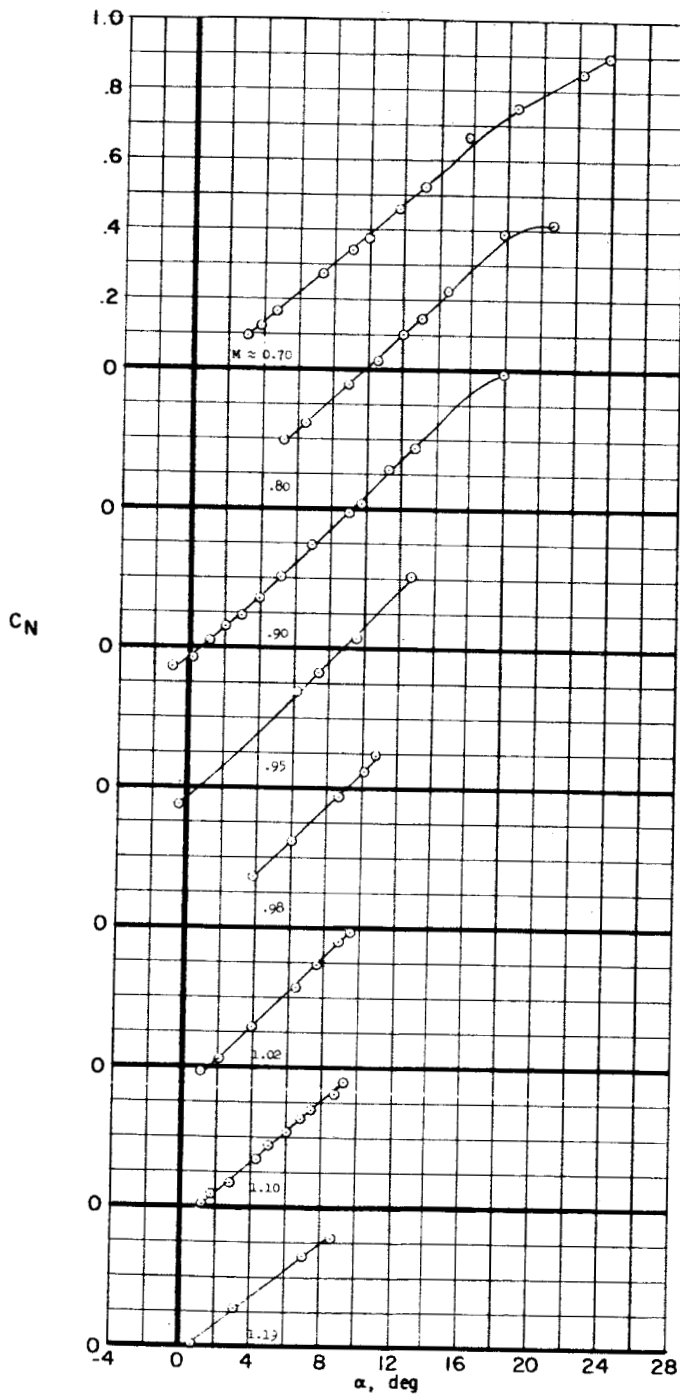


(c) $M \approx 1.02$.



(d) $M \approx 1.19$.

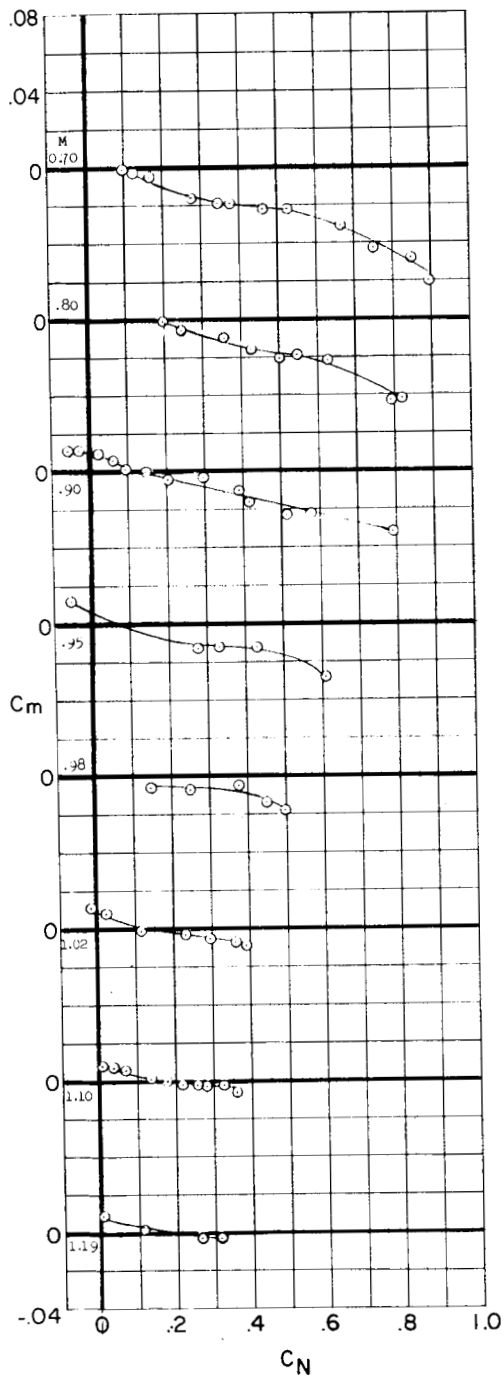
Figure 6.- Concluded.



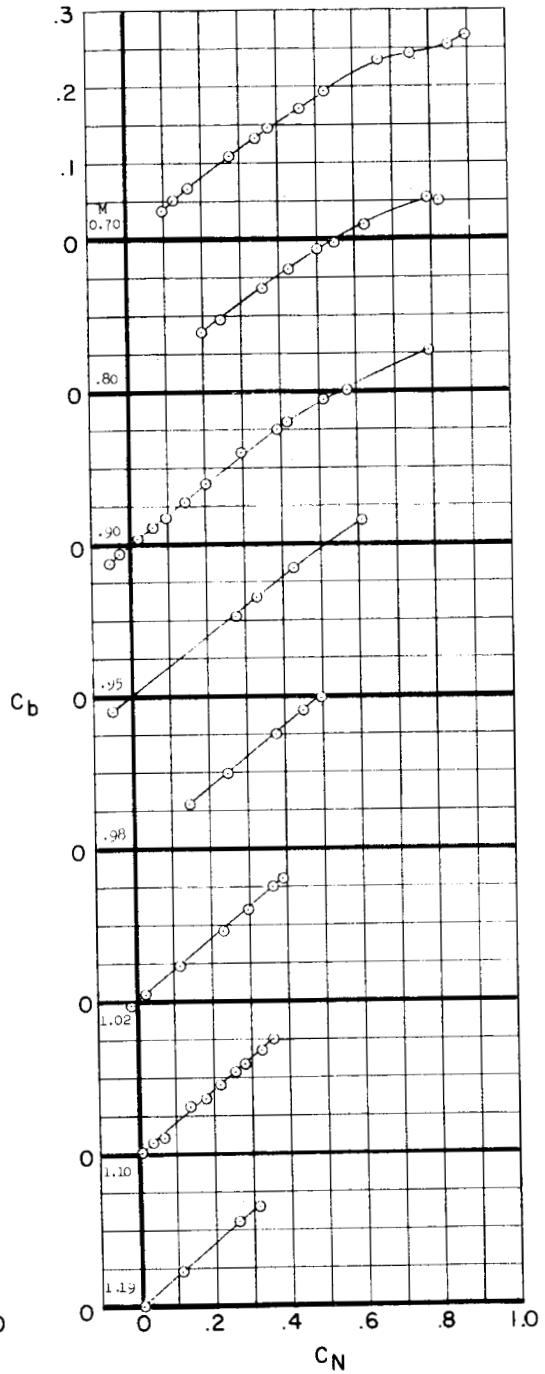
(a) Normal force.

Figure 7.- Wing-panel characteristics for the JF-102A airplane.

CONFIDENTIAL



(b) Pitching moment.



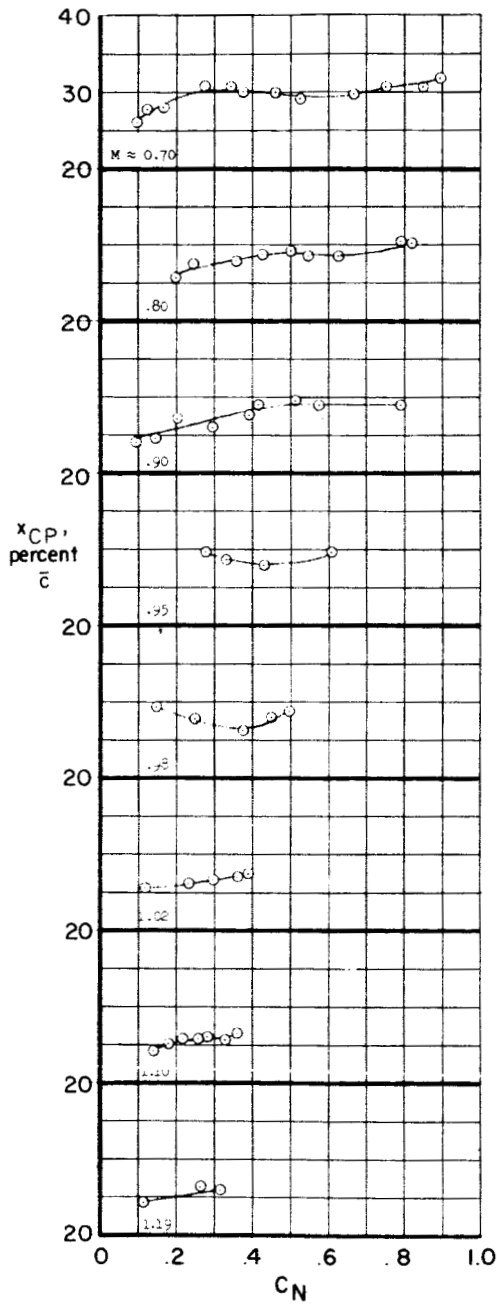
(c) Bending moment.

Figure 7.- Continued.

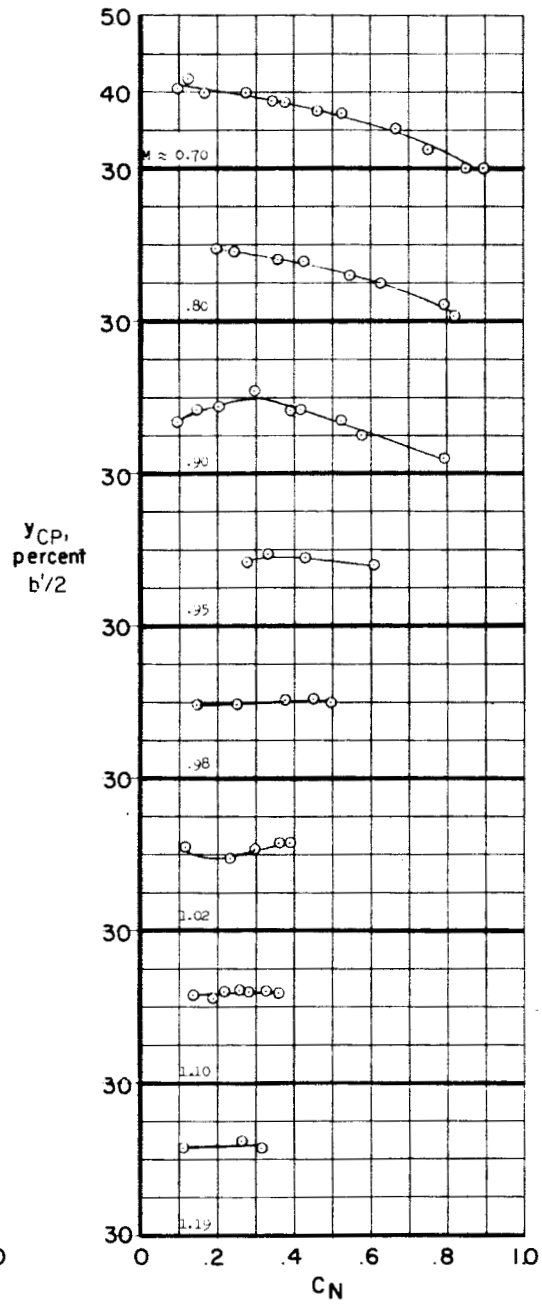
CONFIDENTIAL

DIT-11

H-110



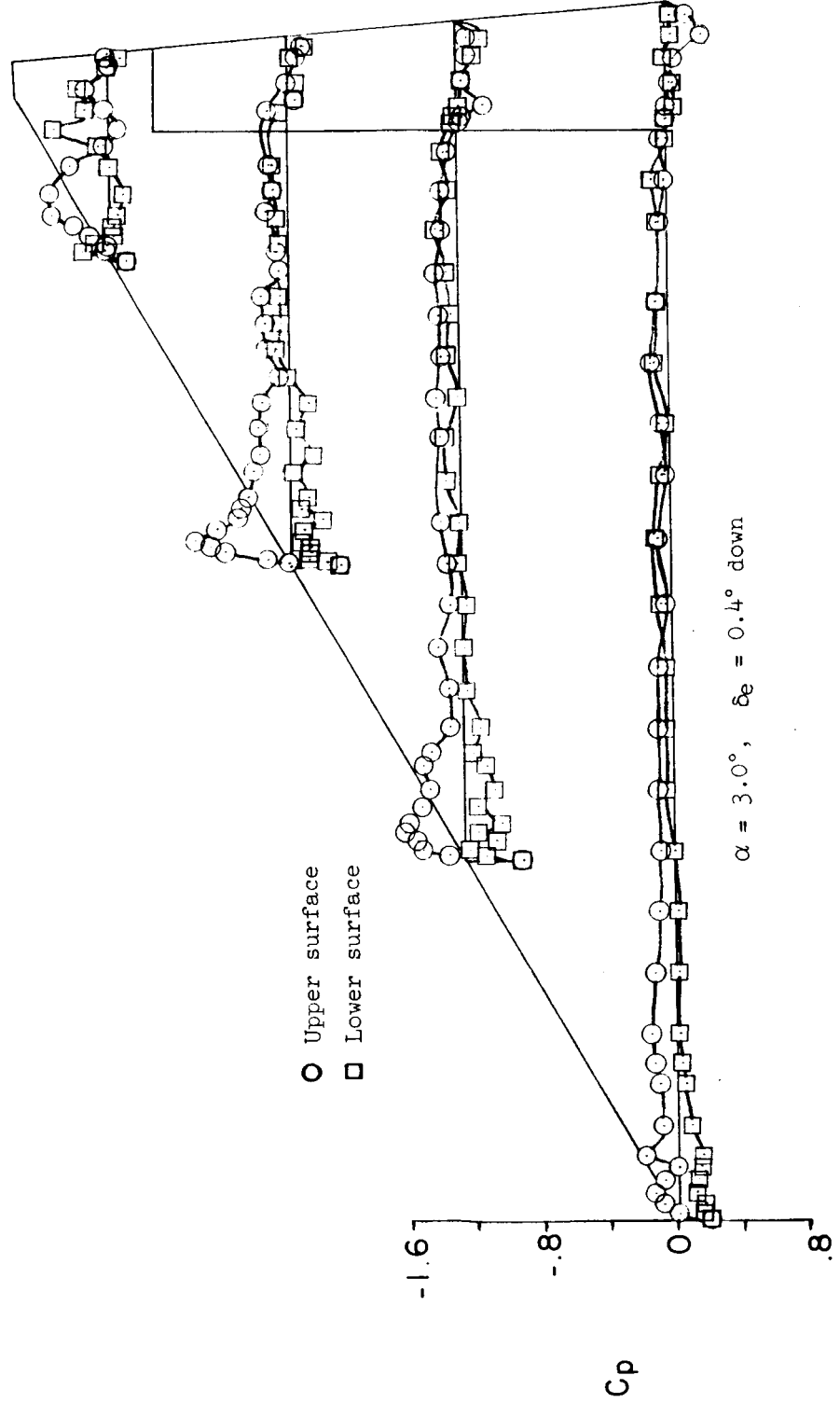
(d) Chordwise location of center of pressure.



(e) Spanwise location of center of pressure.

Figure 7.- Concluded.

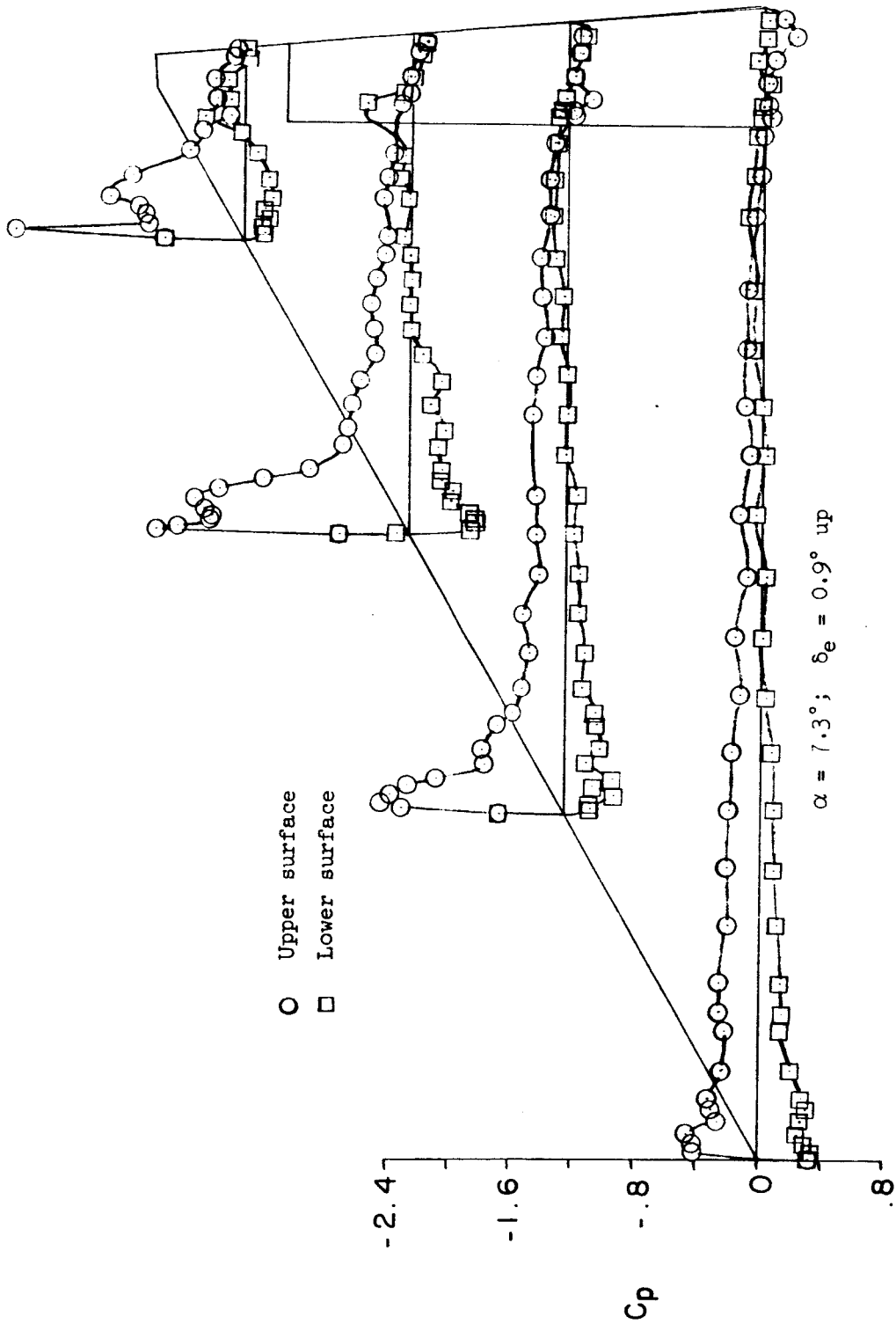
CONFIDENTIAL



(a) $M \approx 0.70; C_{p, \text{sonic}} \approx -0.78.$

Figure 8.- Chordwise pressure distributions over the wing of the JF-102A airplane.

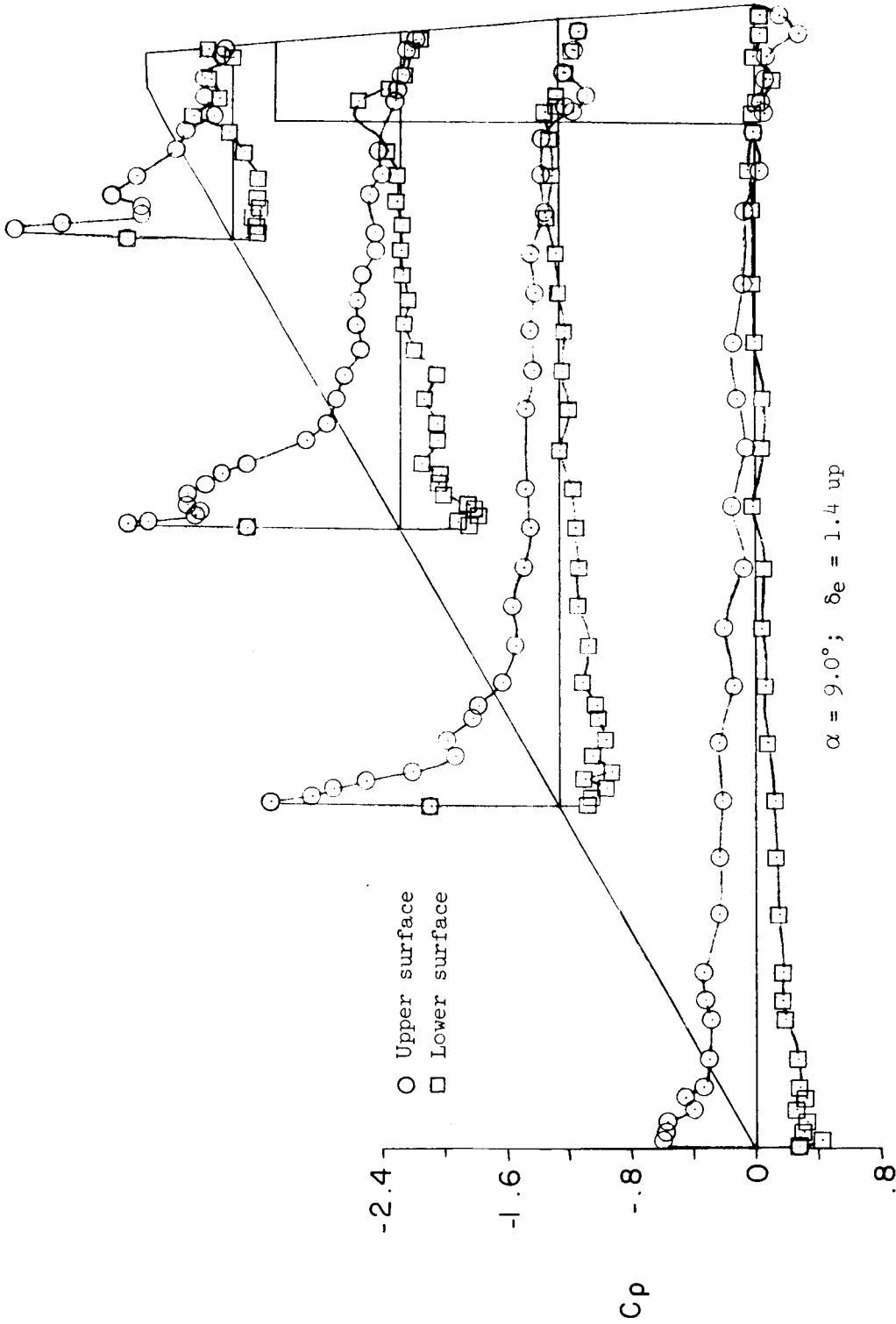
H-116



(a) $M \approx 0.70$ - continued.

Figure 8.- Continued.

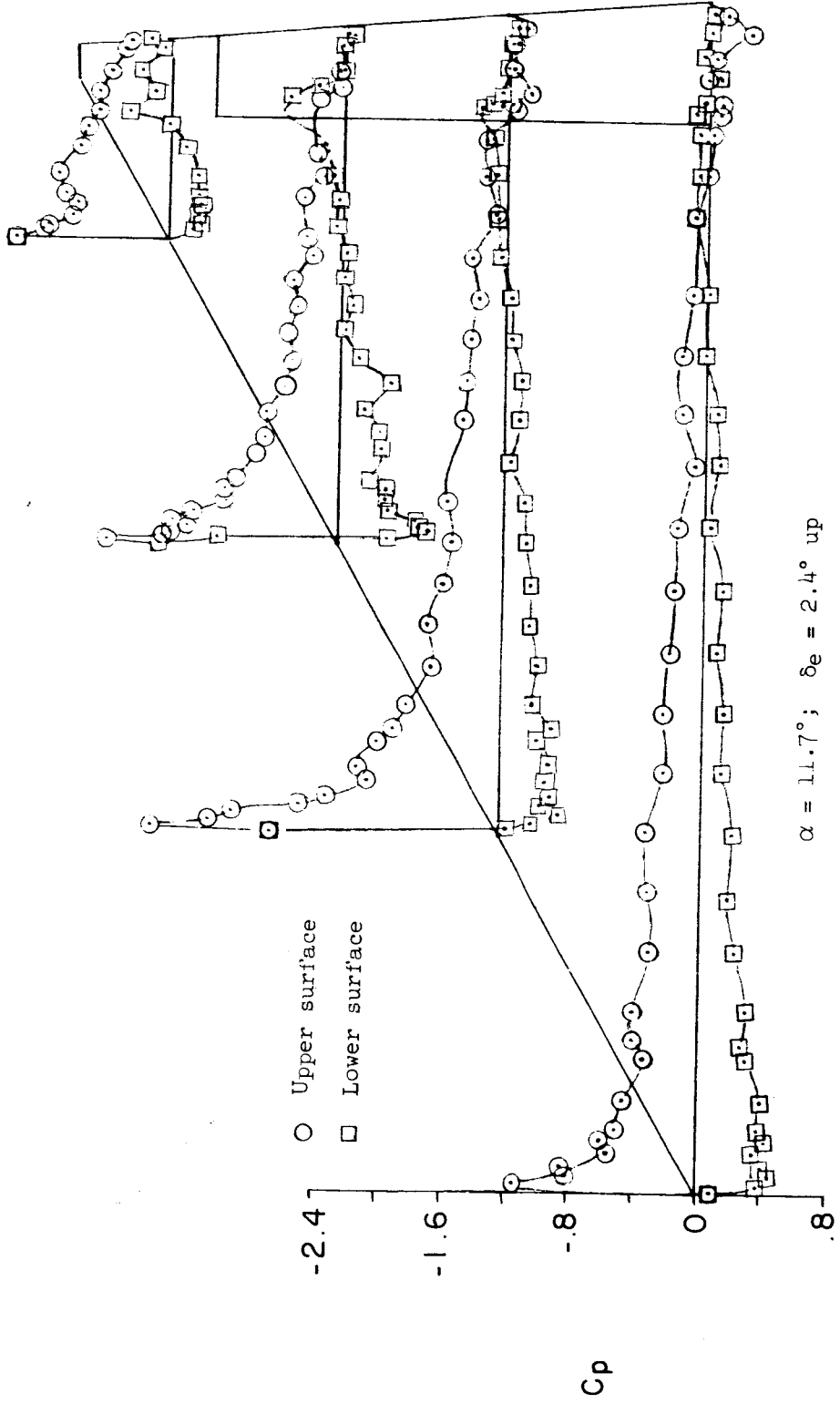
CONFIDENTIAL



(a) $M \approx 0.70$ - continued.

Figure 8.- Continued.

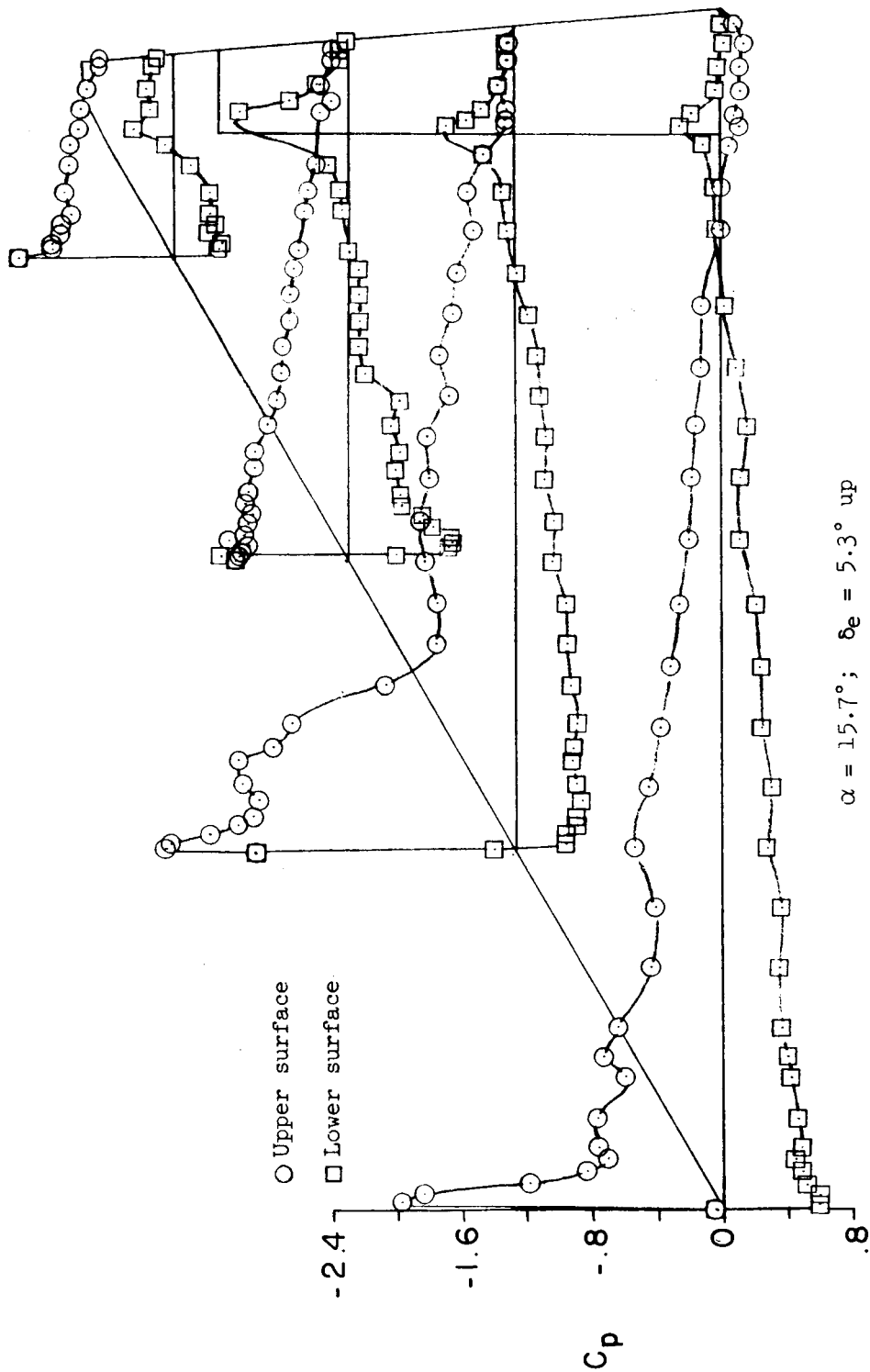
H-1116



(a) $M \approx 0.70$ - continued.

Figure 8.- Continued.

CONFIDENTIAL

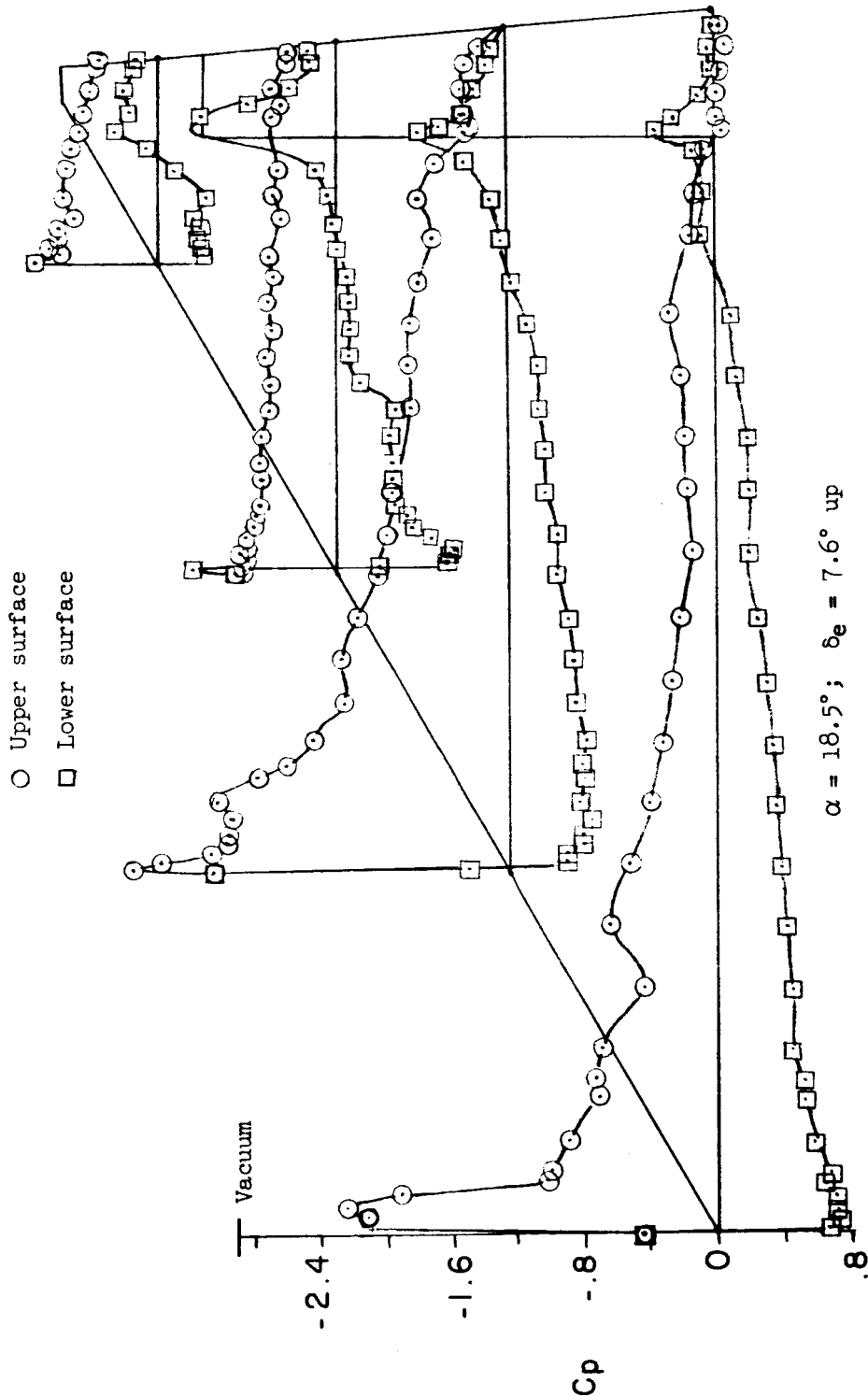


$\alpha = 15.7^\circ$; $\delta_e = 5.3^\circ$ up

(a) $M \approx 0.70$ - continued.

Figure 8.- Continued.

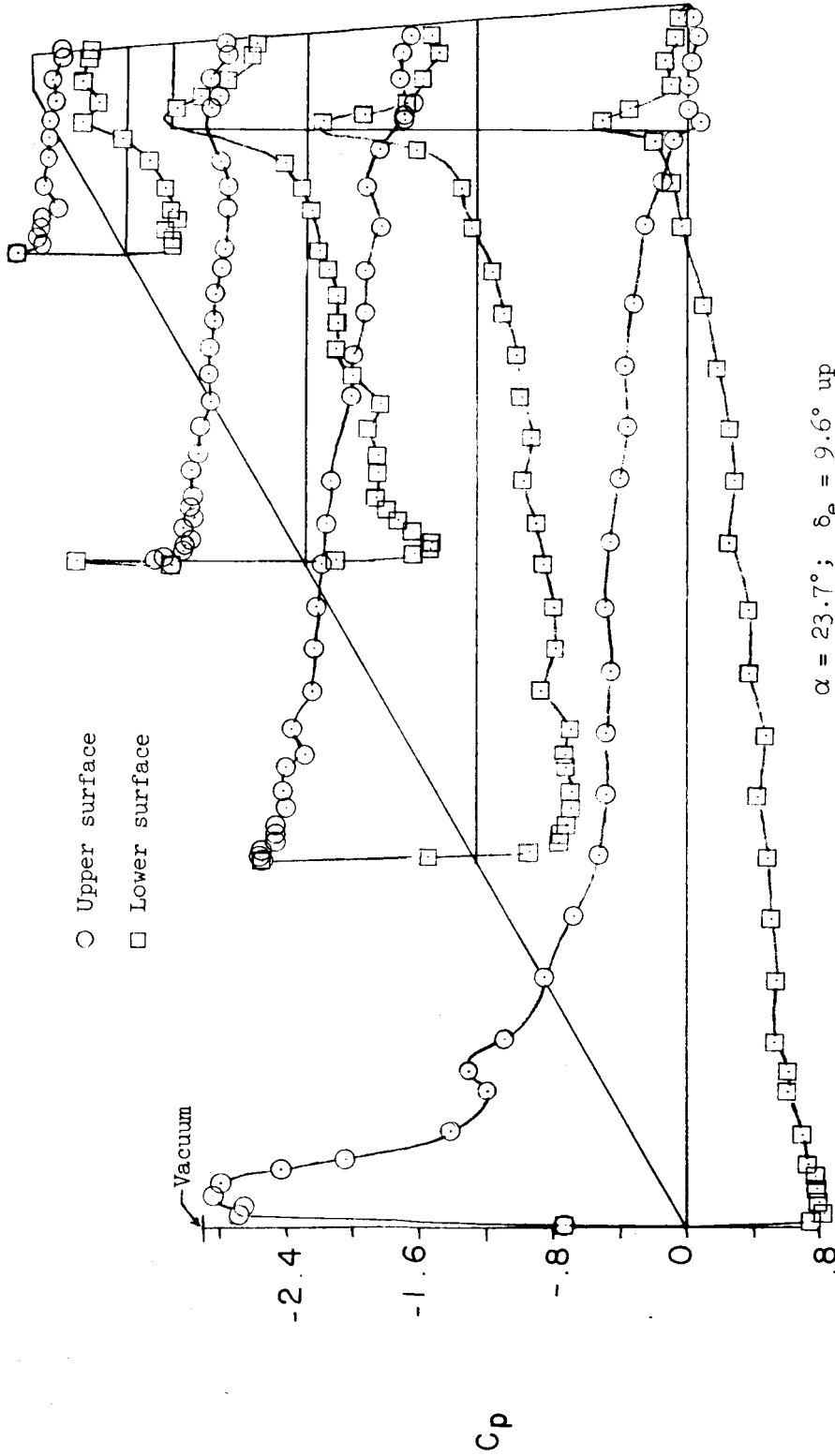
SECRET



(a) $M \approx 0.70$ - continued.

Figure 8.- Continued.

CONFIDENTIAL



$\alpha = 23.7^\circ$; $\delta_e = 9.6^\circ$ up

(a) $M \approx 0.70$ - concluded.

Figure 8:- Continued.

CONFIDENTIAL

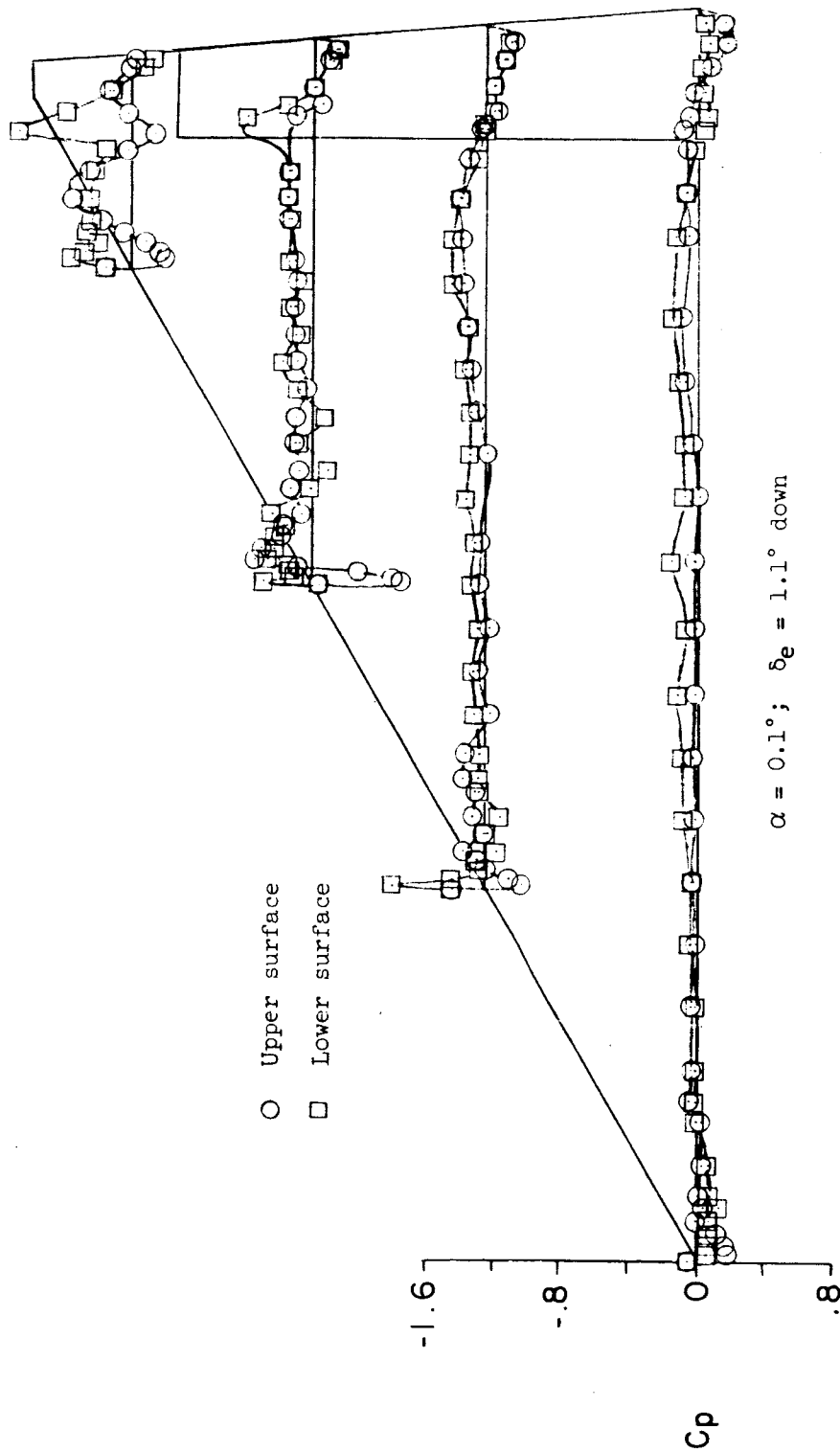
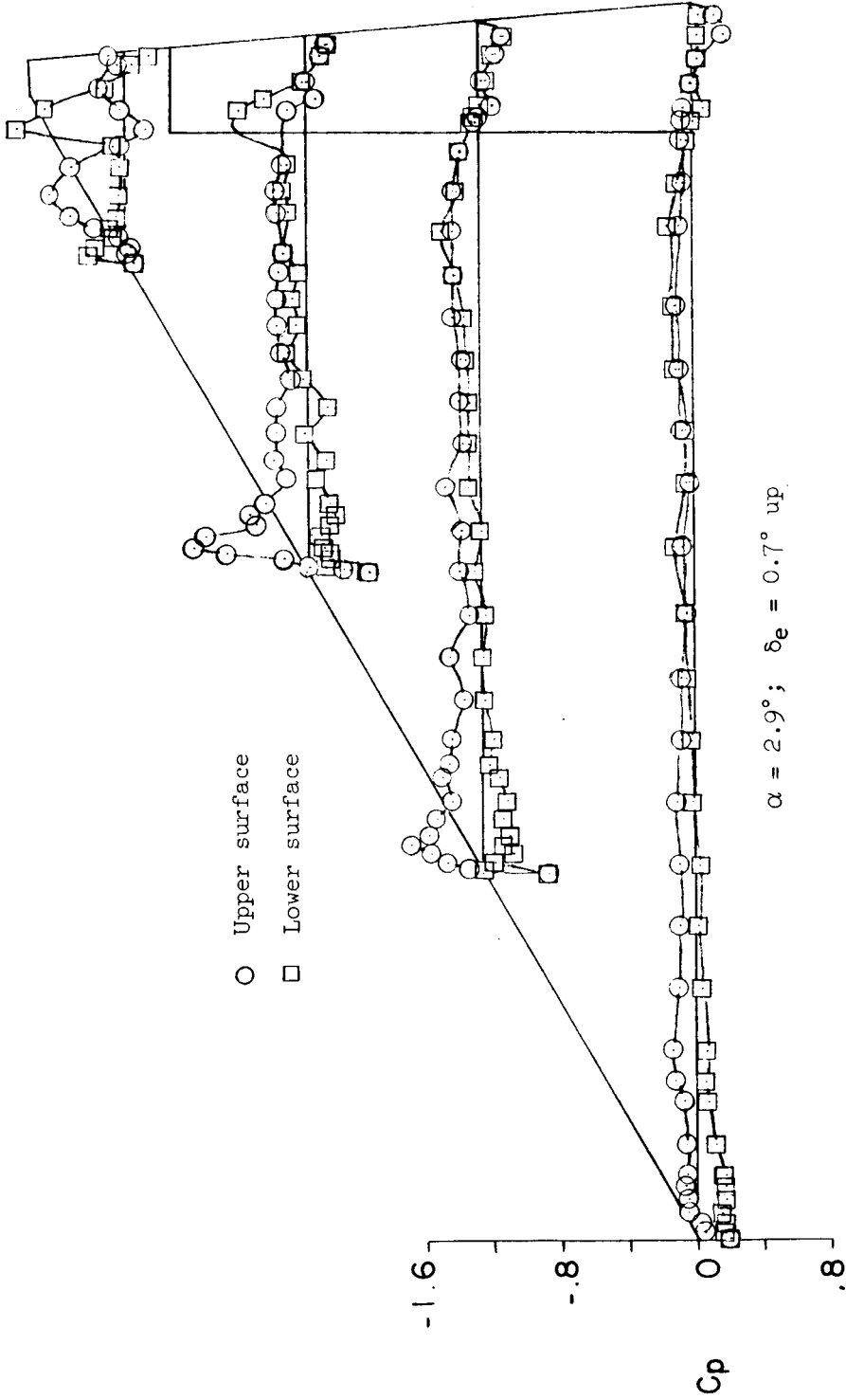


Figure 8.- Continued.

CONFIDENTIAL

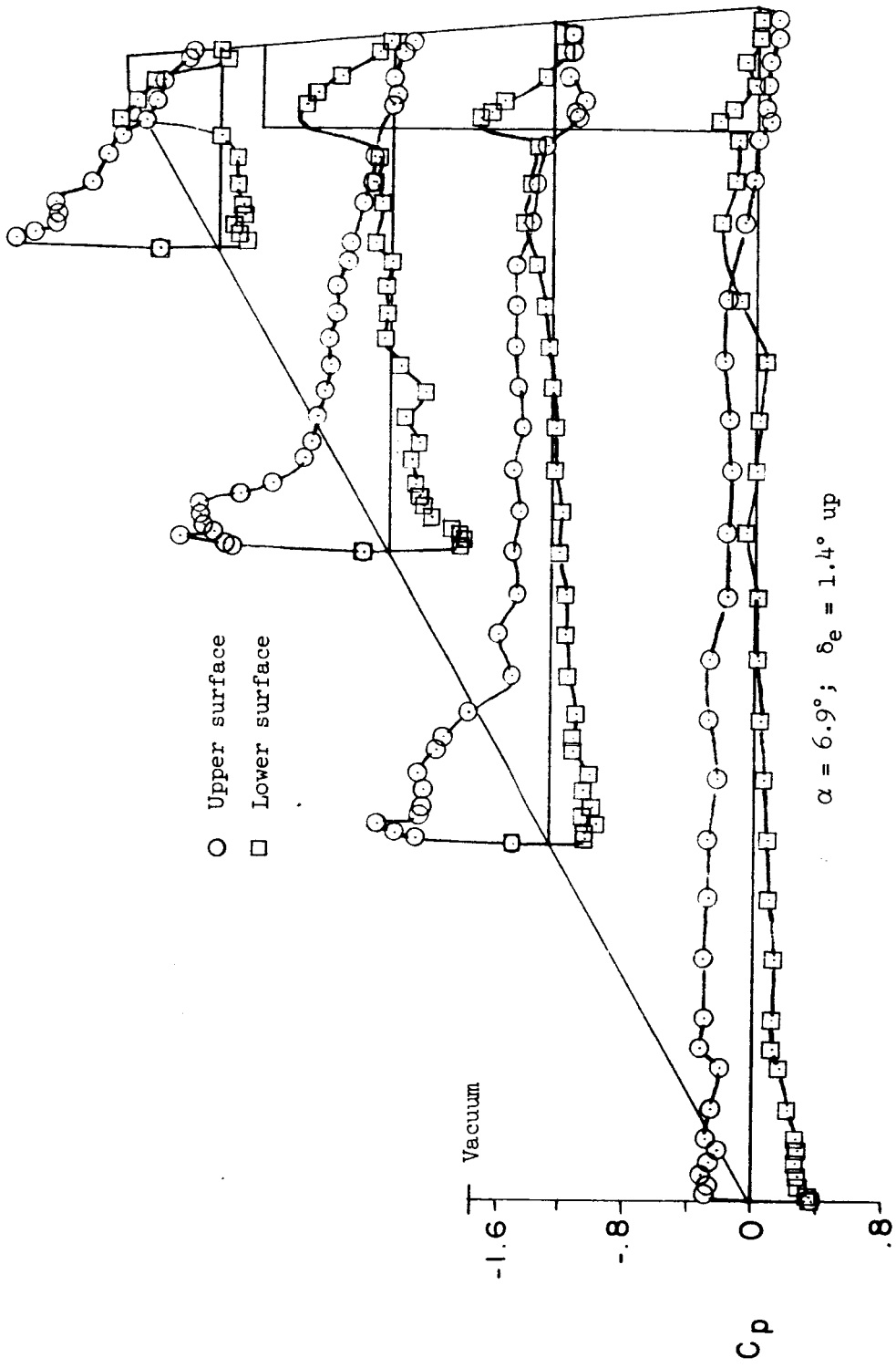


(b) $M \approx 0.90$ - continued.

Figure 8.- Continued.

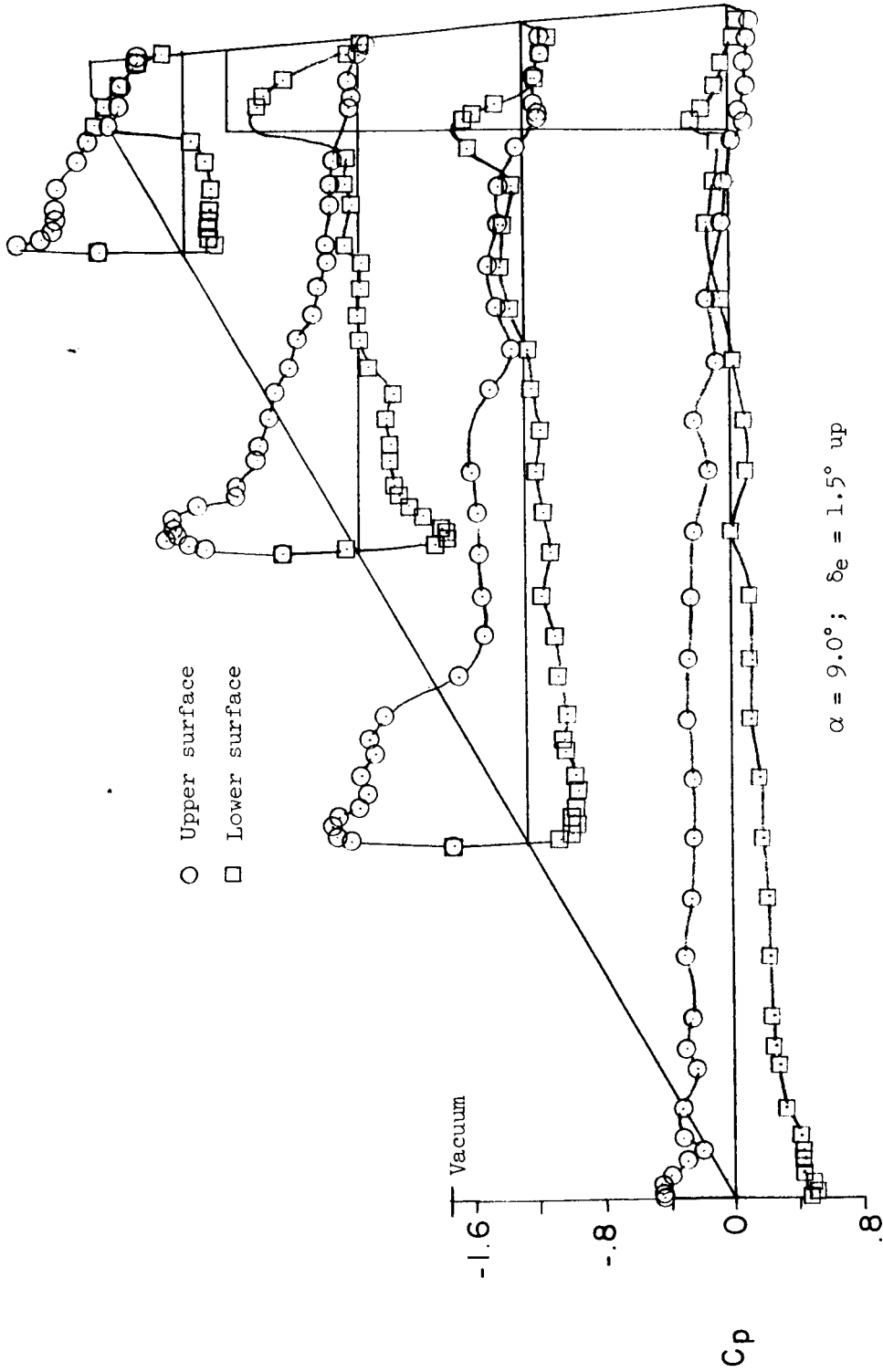
SECRET

H-1116



(b) $M \approx 0.90$ - continued.

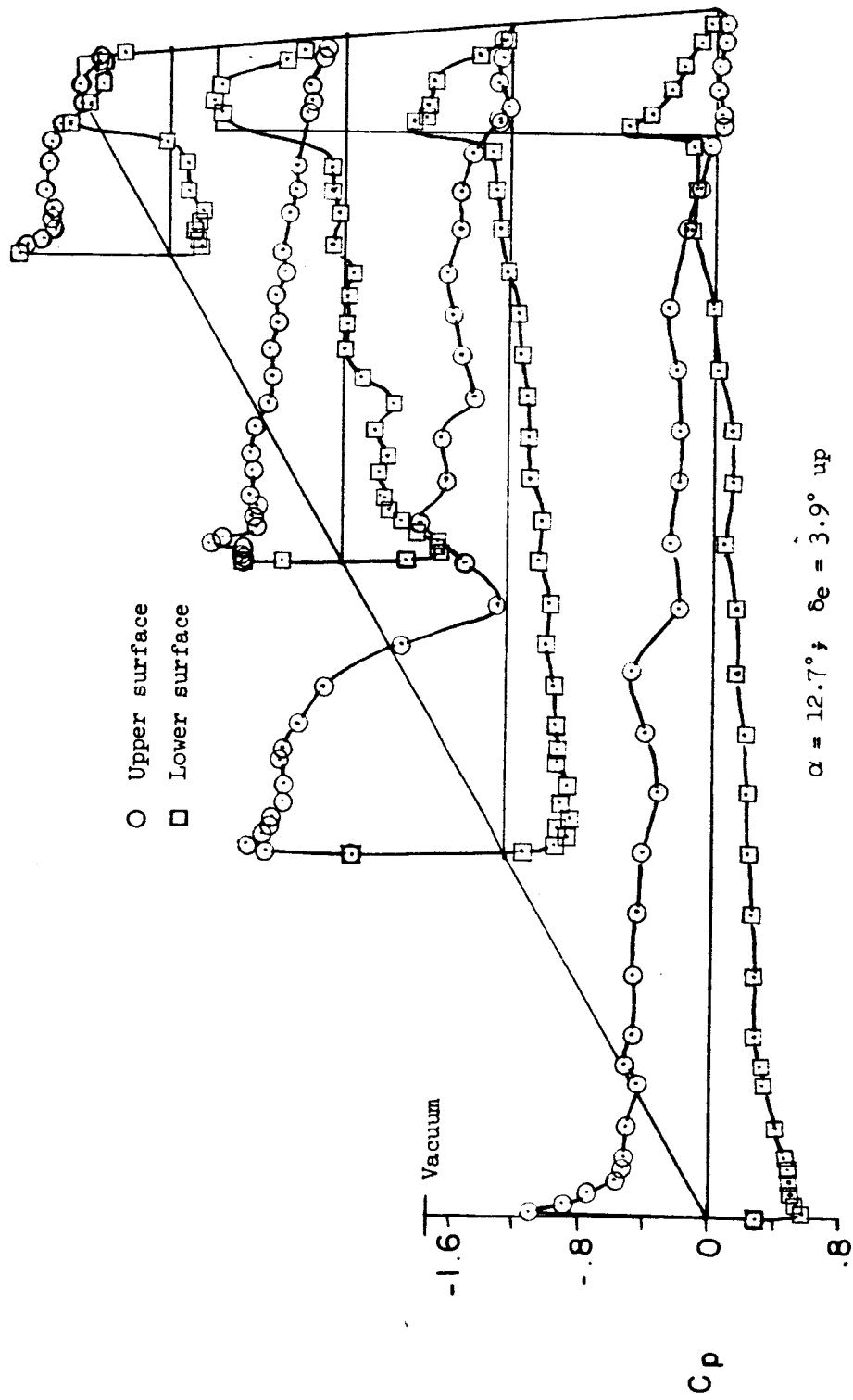
Figure 8.- Continued.



(b) $M \approx 0.90$ - continued.

Figure 8.- Continued.

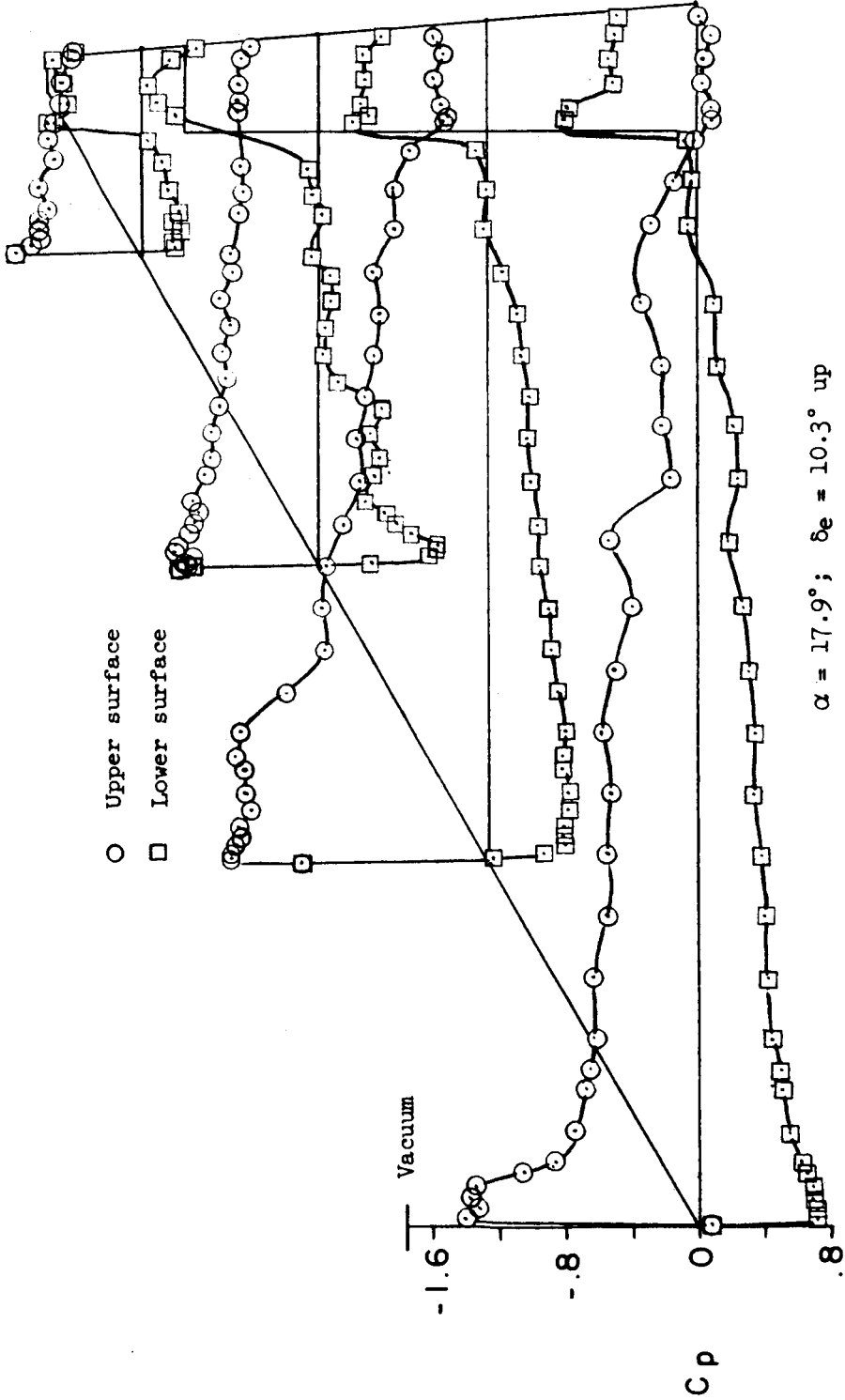
SECRET



(b) $M \approx 0.90$ - continued.

Figure 8.- Continued.

CONFIDENTIAL



(b) $M \approx 0.90$ - concluded.

Figure 8.- Continued.

CONFIDENTIAL

SECRET

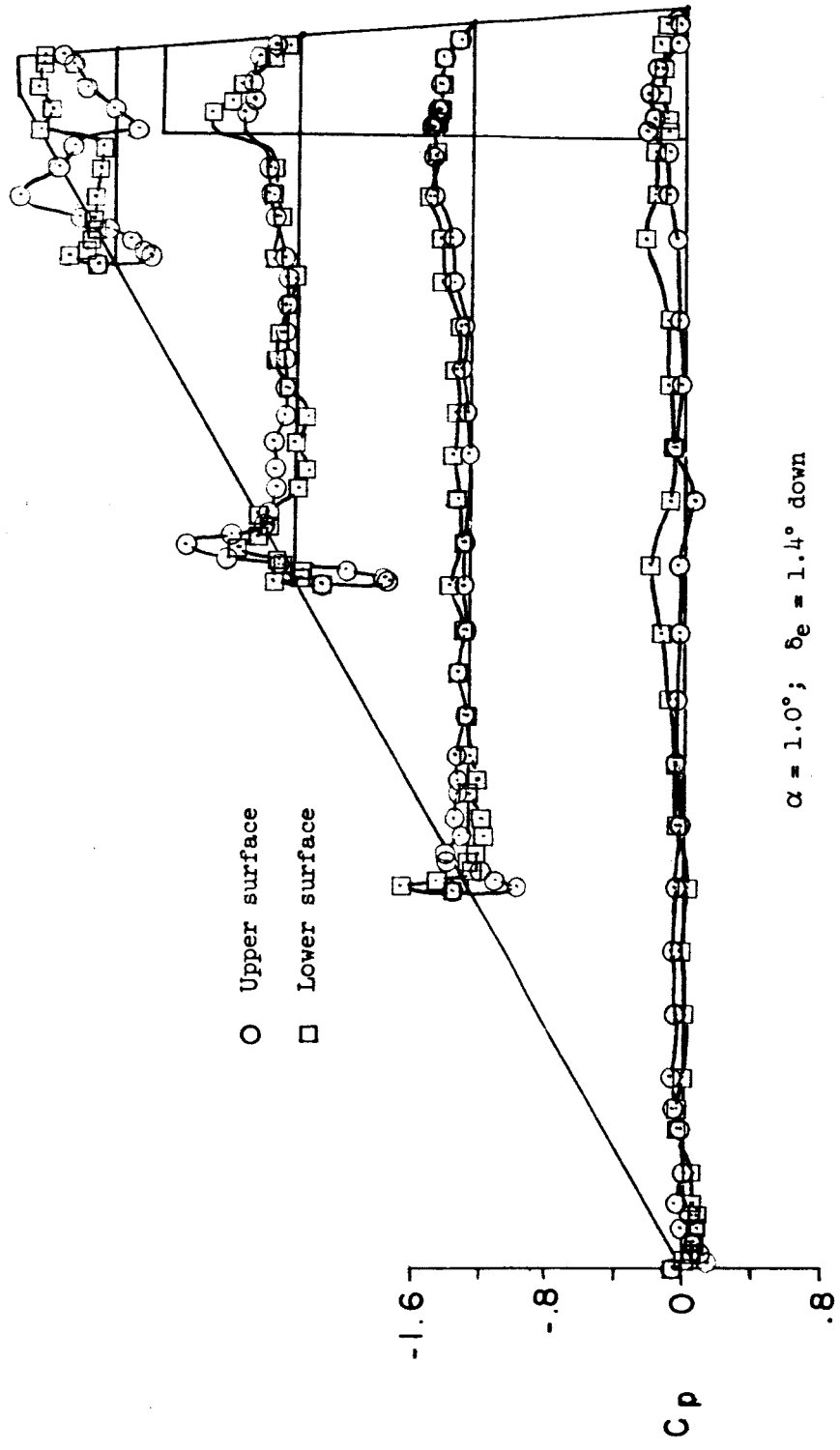
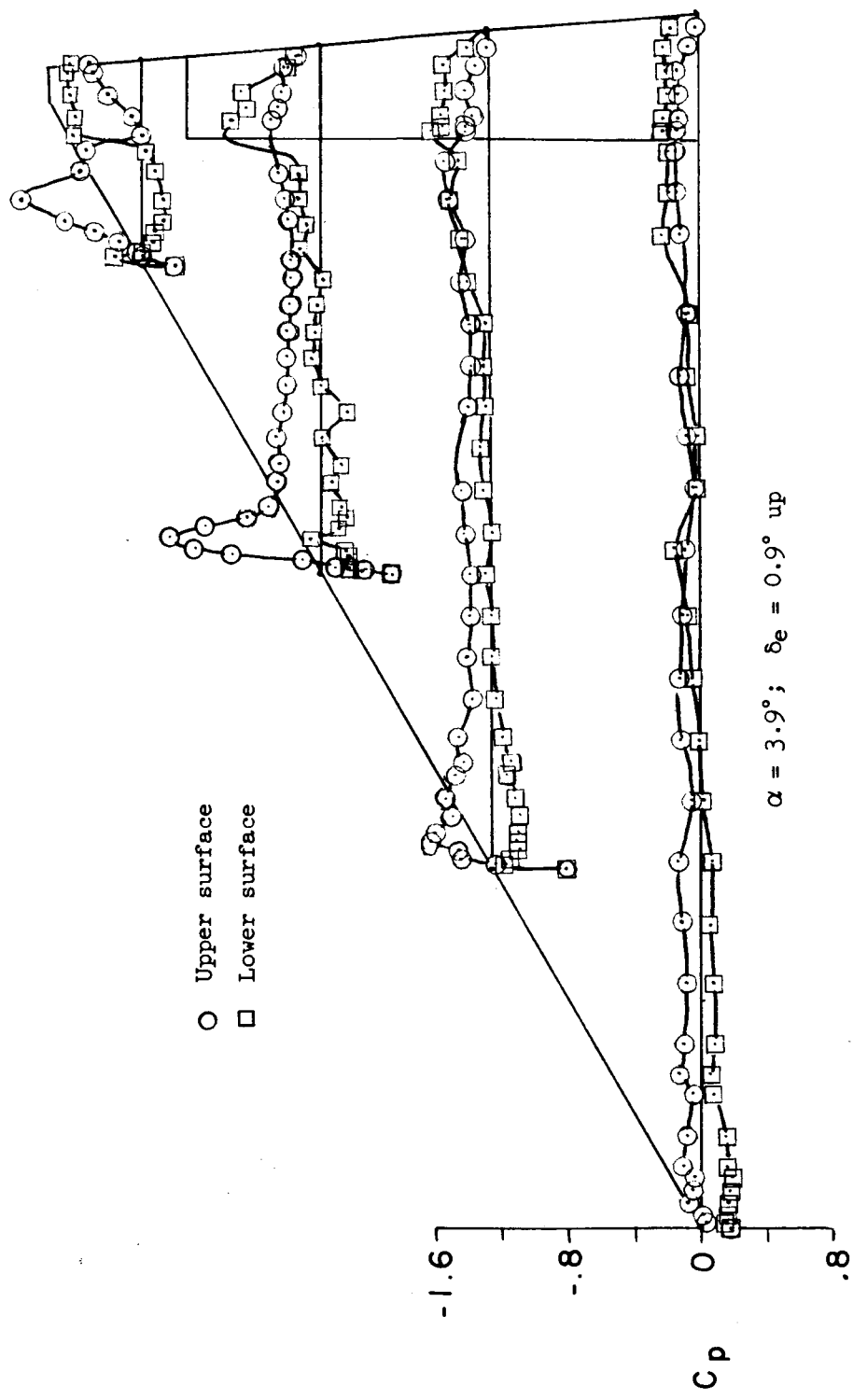


Figure 8.- Continued.

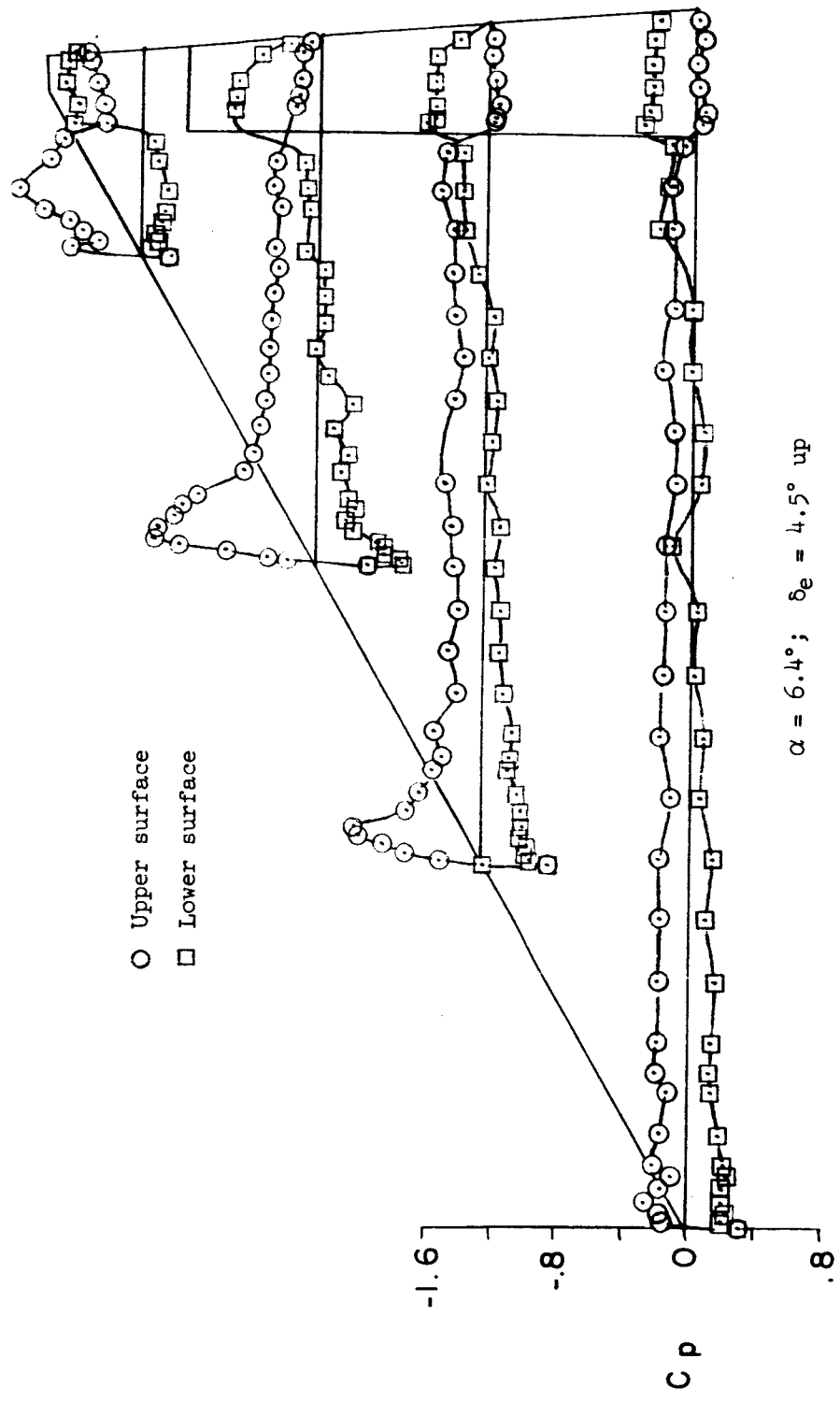
CONFIDENTIAL



(c) $M \approx 1.02$ - continued.

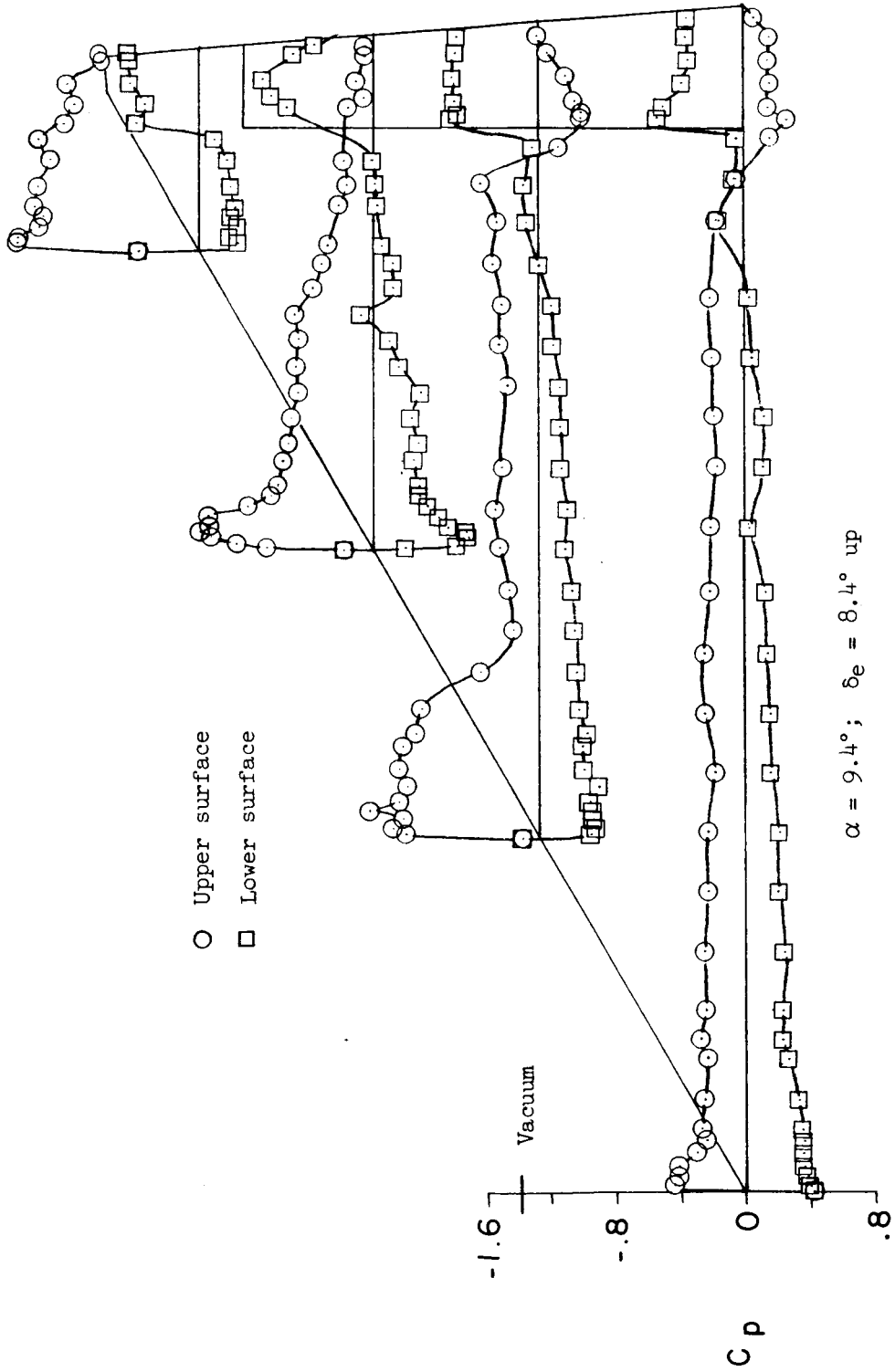
Figure 8.- Continued.

CONFIDENTIAL



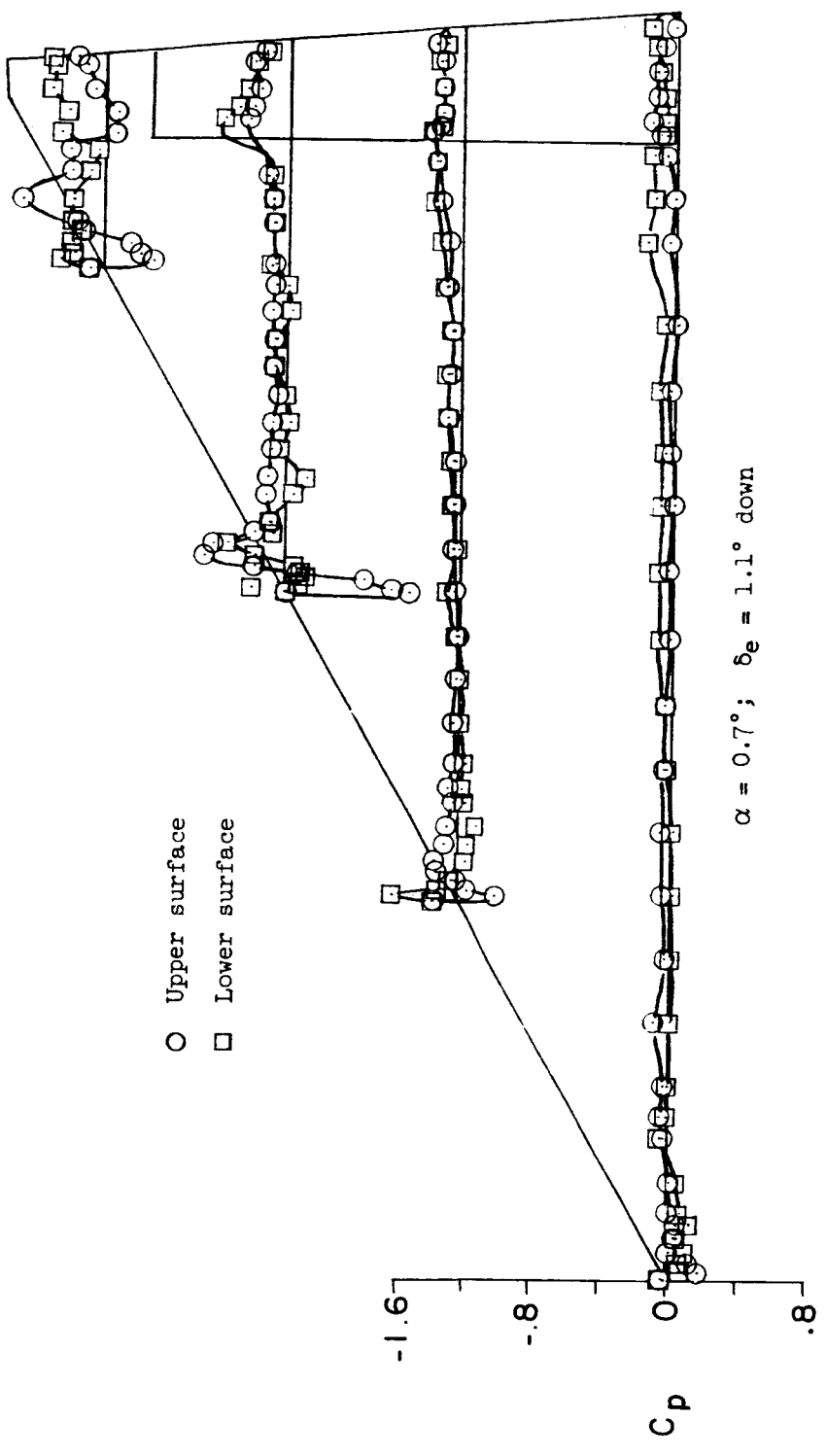
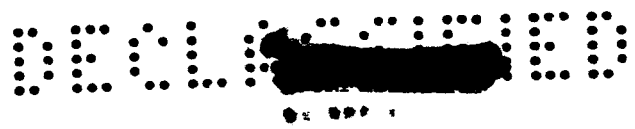
(c) $M \approx 1.02$ - continued.

Figure 8.- Continued.



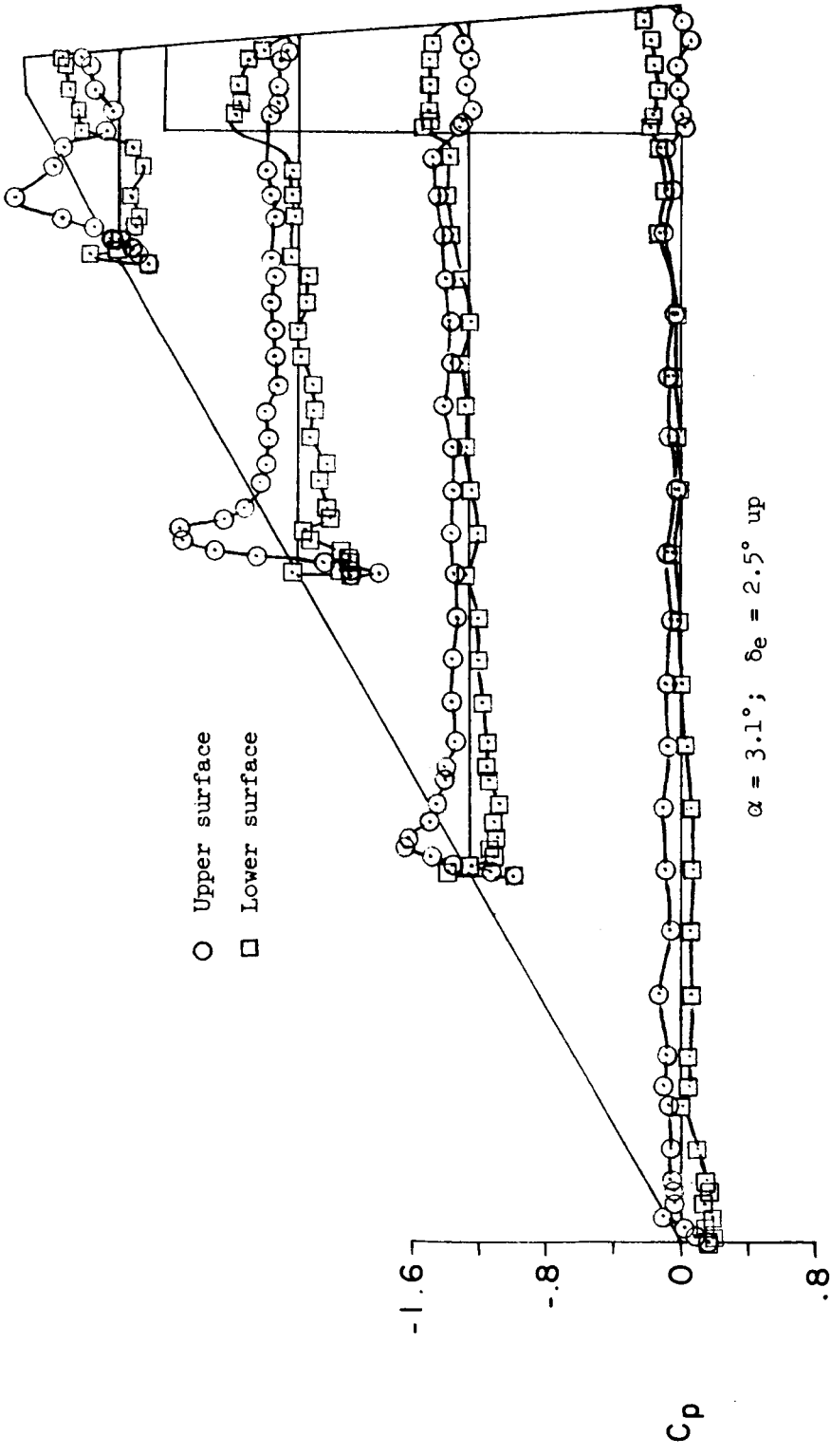
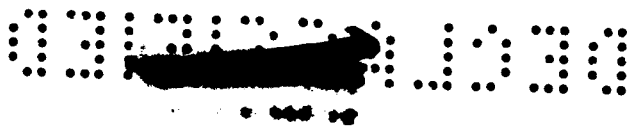
(c) $M \approx 1.02$ - concluded.

Figure 8.- Continued.



(d) $M \approx 1.19; C_{p, \text{sonic}} \approx 0.26.$

Figure 8.- Continued.

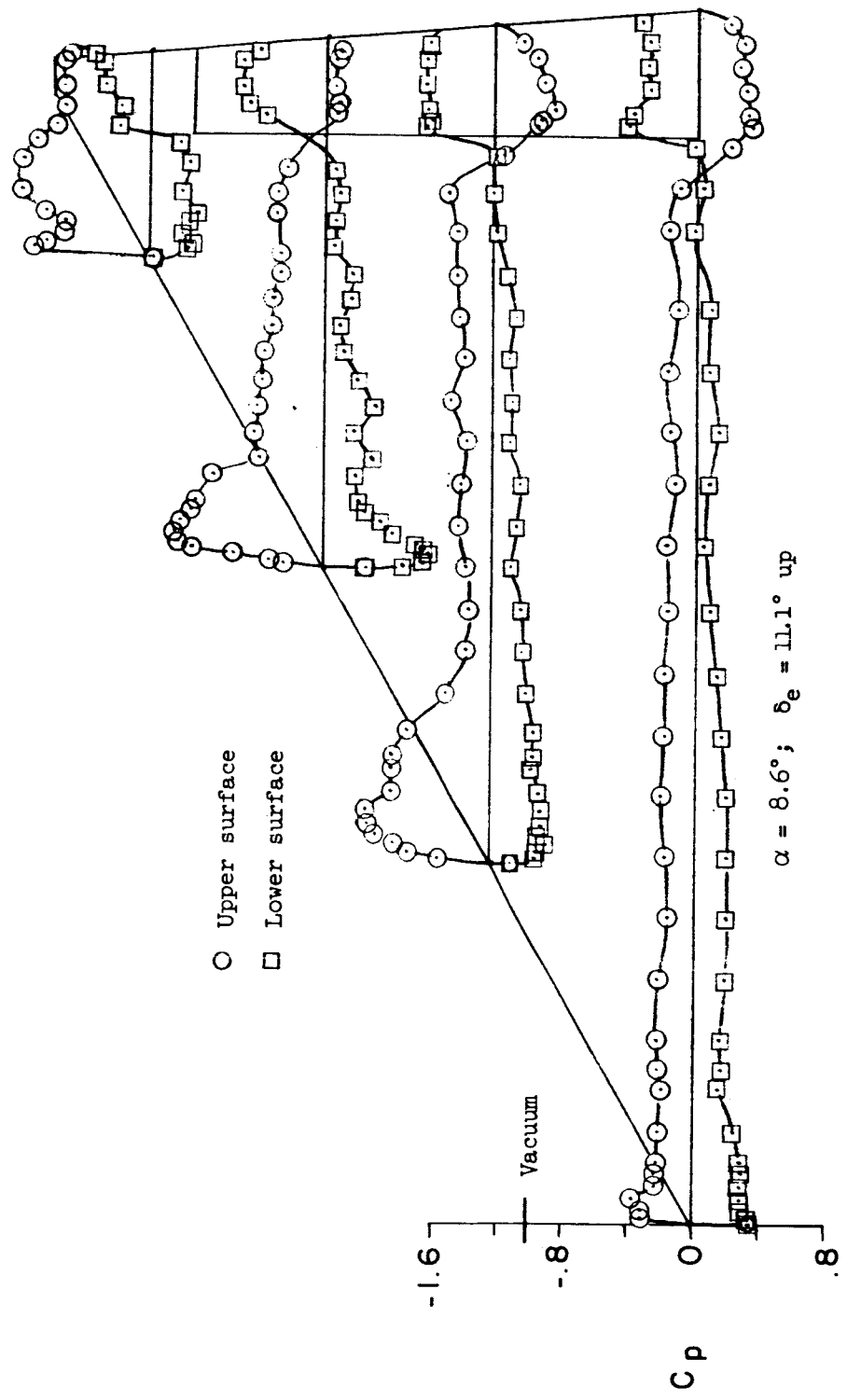


(d) $M \approx 1.19$ - continued.

Figure 8.- Continued.

CONFIDENTIAL

H-116



(d) $M \approx 1.19$ - concluded.

Figure 8.- Concluded.

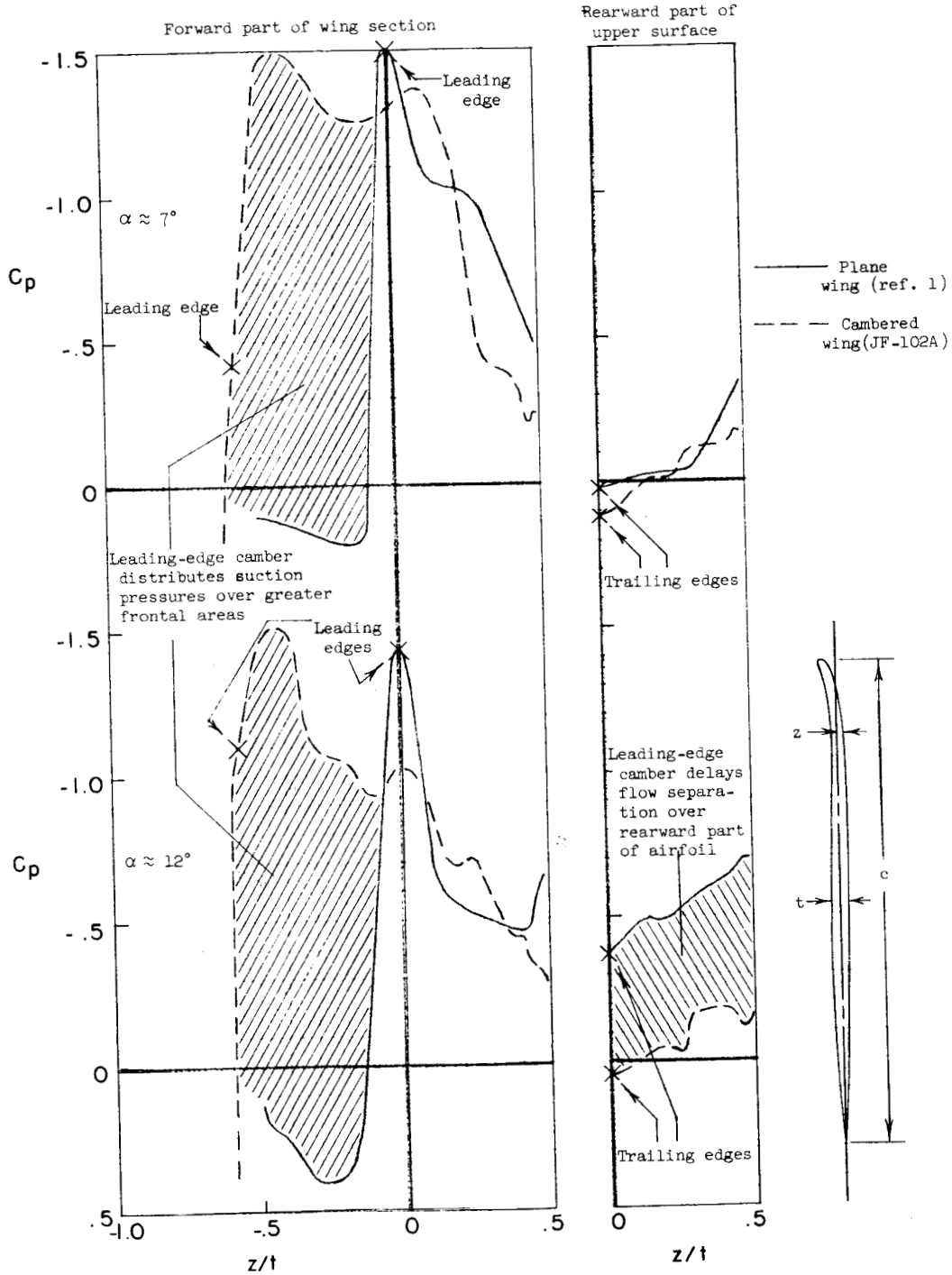
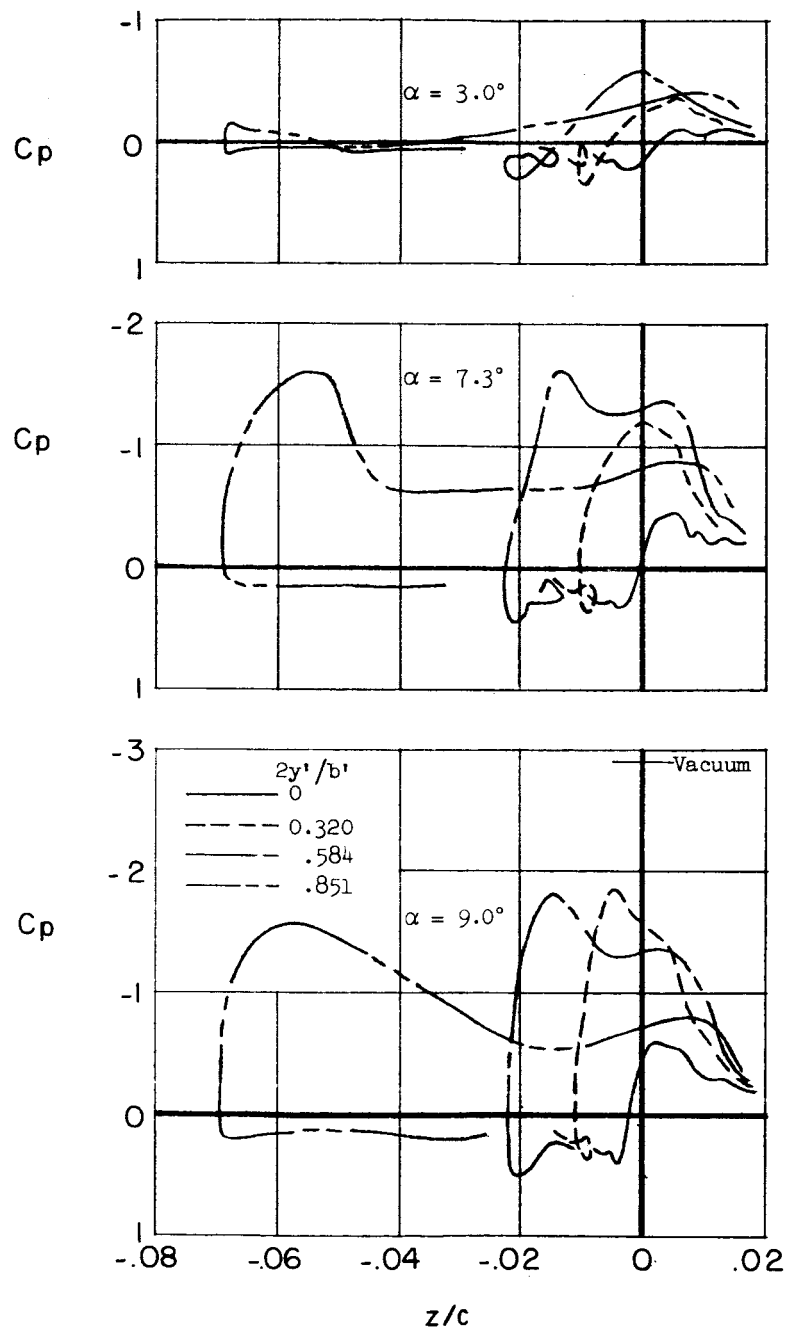


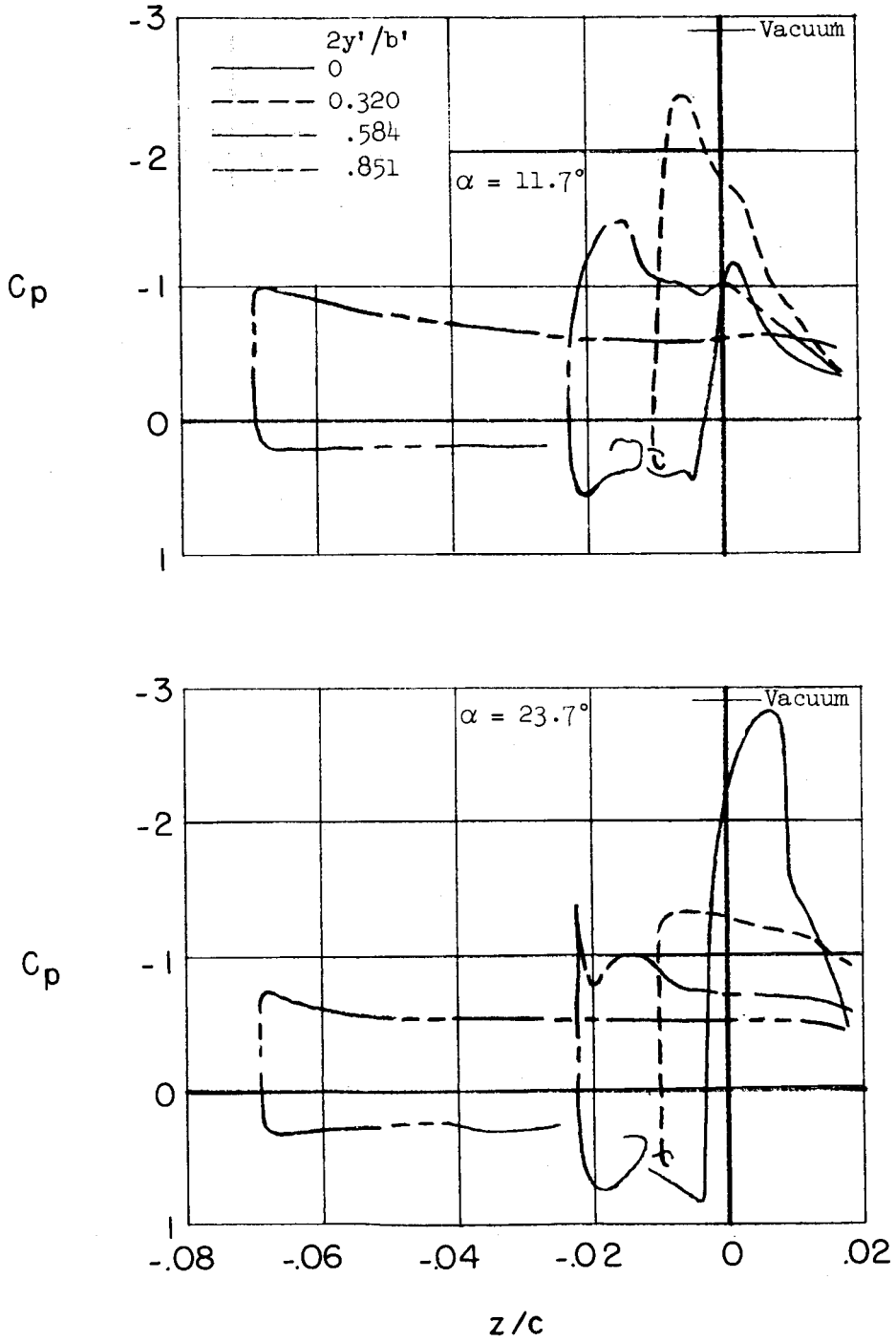
Figure 9.- Thicknesswise distribution of pressures for conically cambered and plane delta wings. $2y'/b' \approx 0.58$. $M \approx 0.70$.



(a) $M \approx 0.70$.

Figure 10.- Thicknesswise pressure distribution over the forward part of four stations of the JF-102A wing.

~~CONFIDENTIAL~~

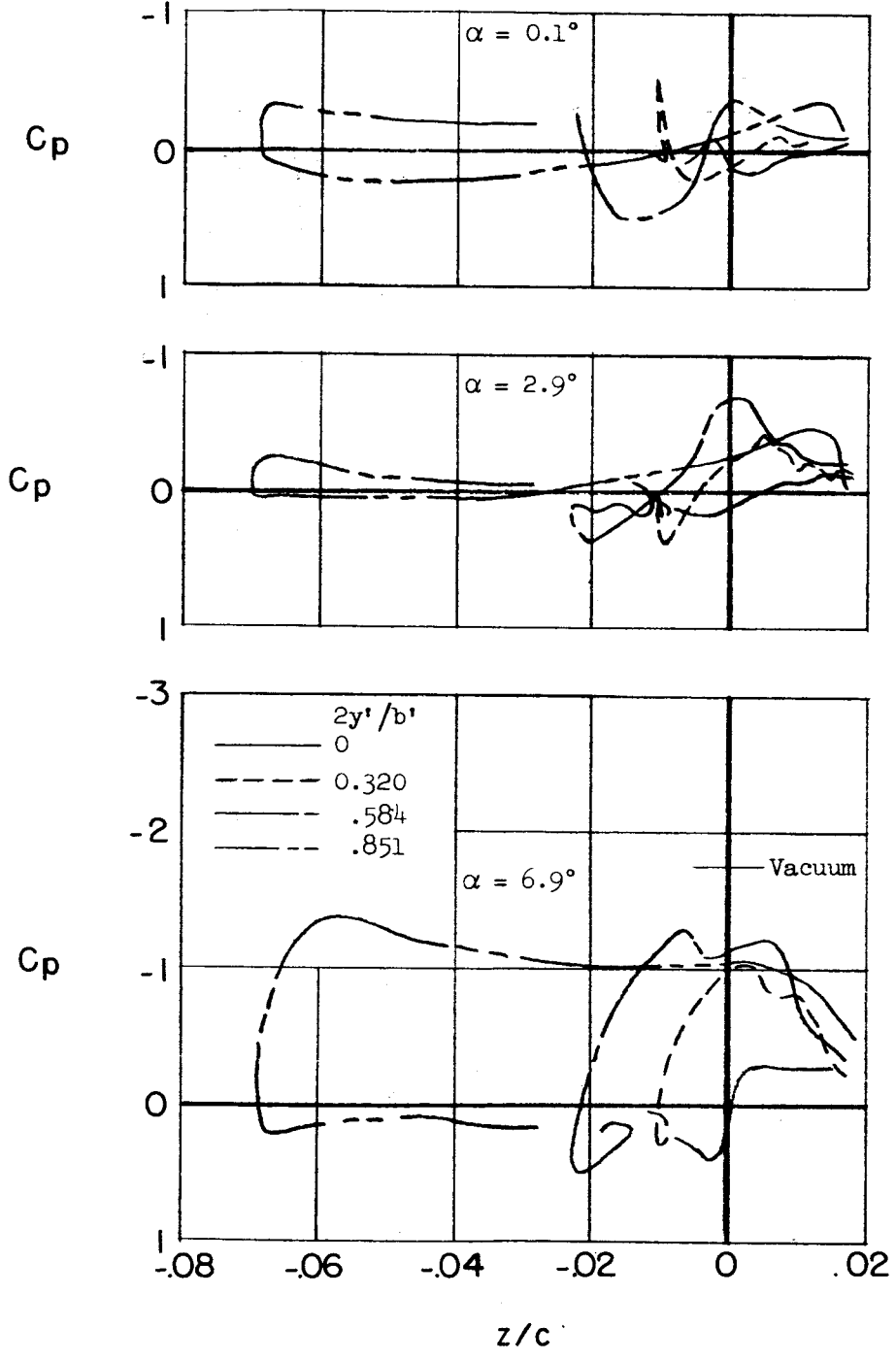


H-116

(a) Concluded.

Figure 10.- Continued.

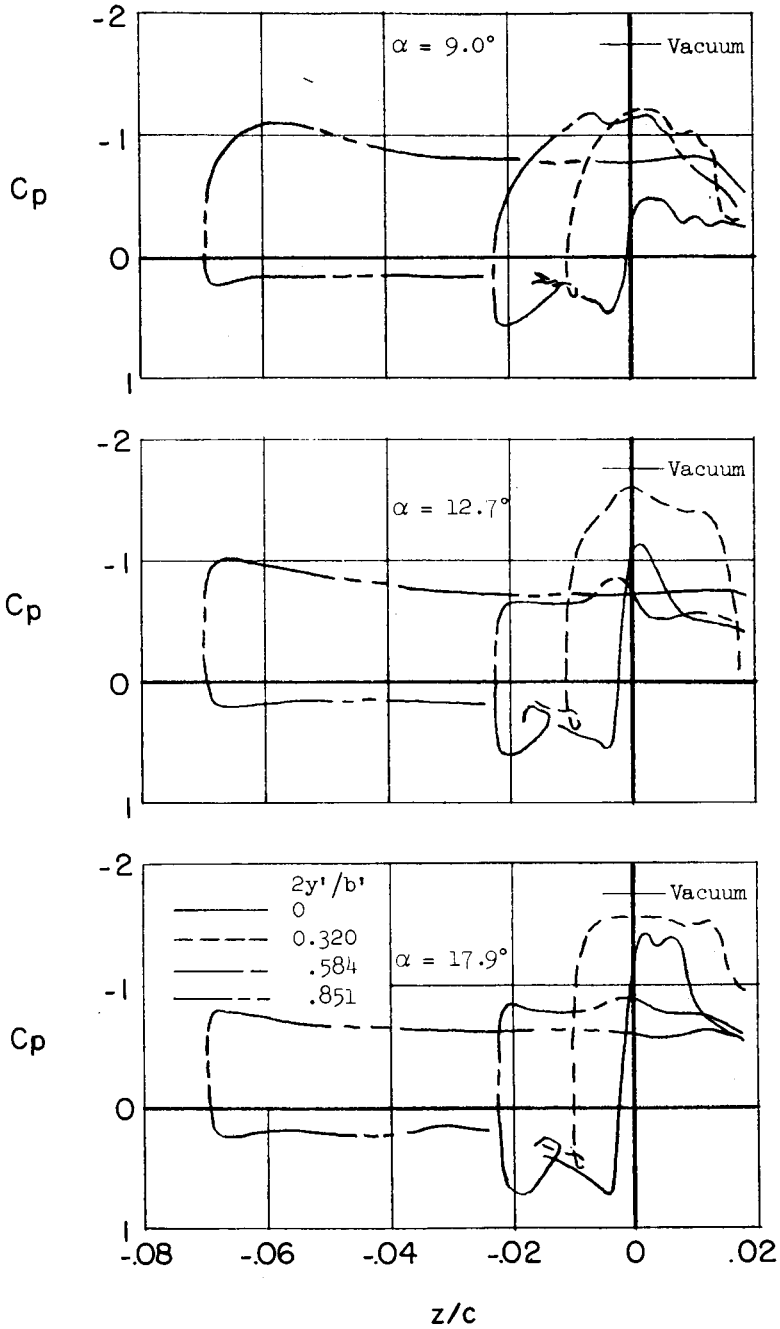
~~CONFIDENTIAL~~



(b) $M \approx 0.90$.

Figure 10.- Continued.

037122 [REDACTED]

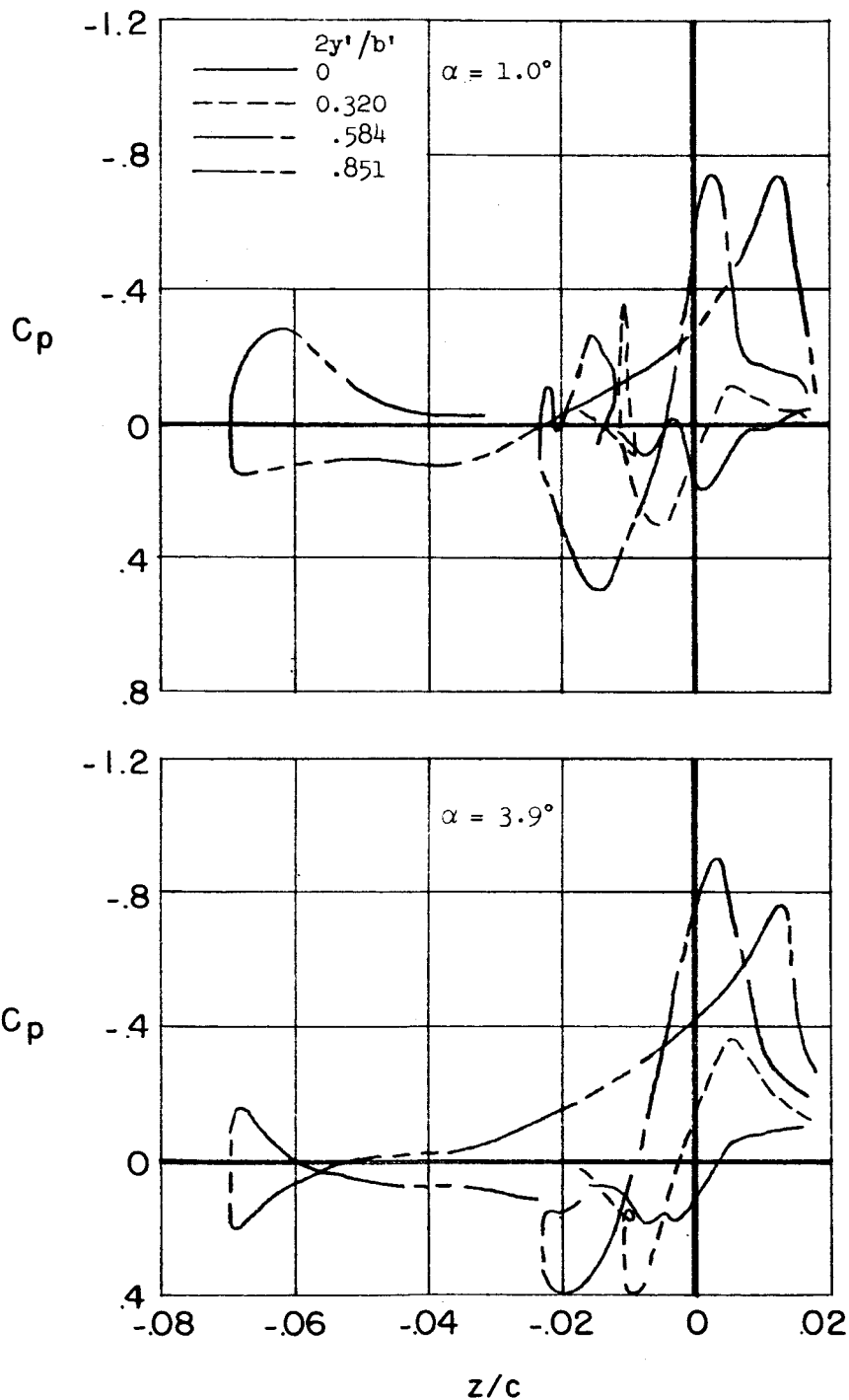


(b) Concluded.

Figure 10.- Continued.

[REDACTED]

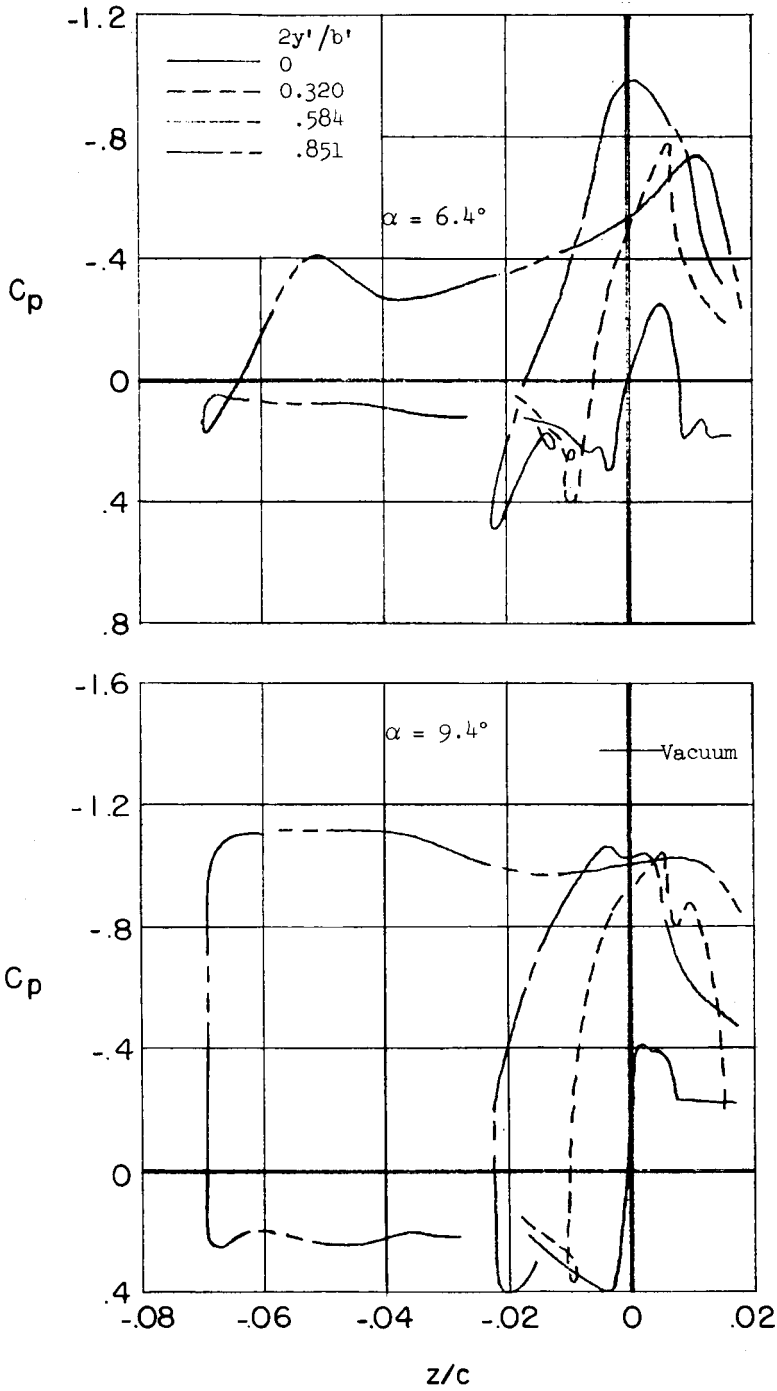
H-116



(c) $M \approx 1.02$.

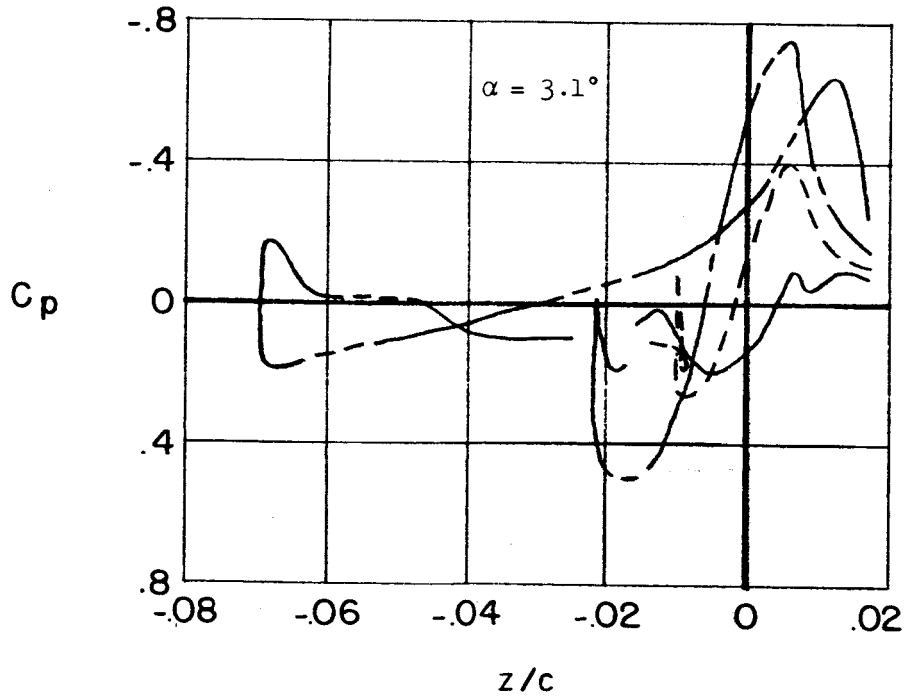
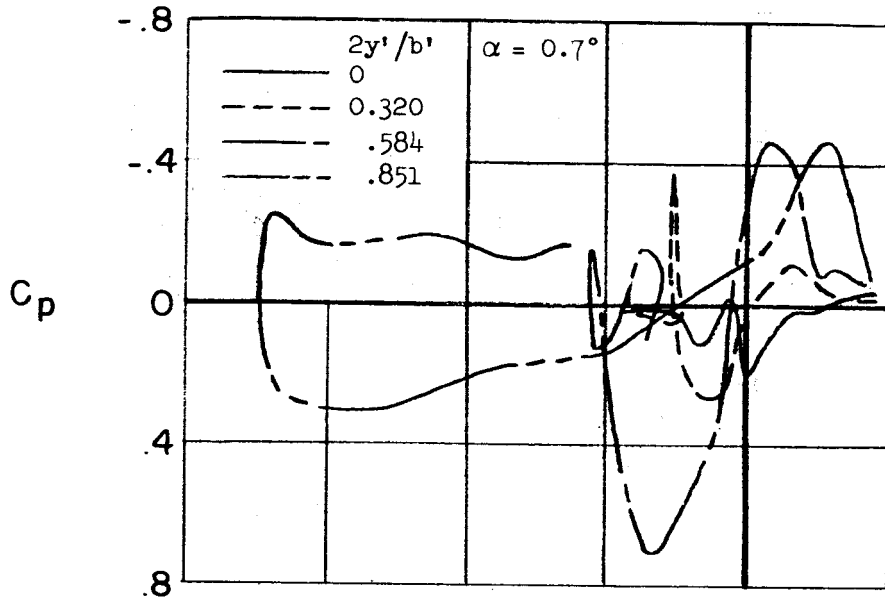
Figure 10.- Continued.

CONFIDENTIAL



(c) Concluded.

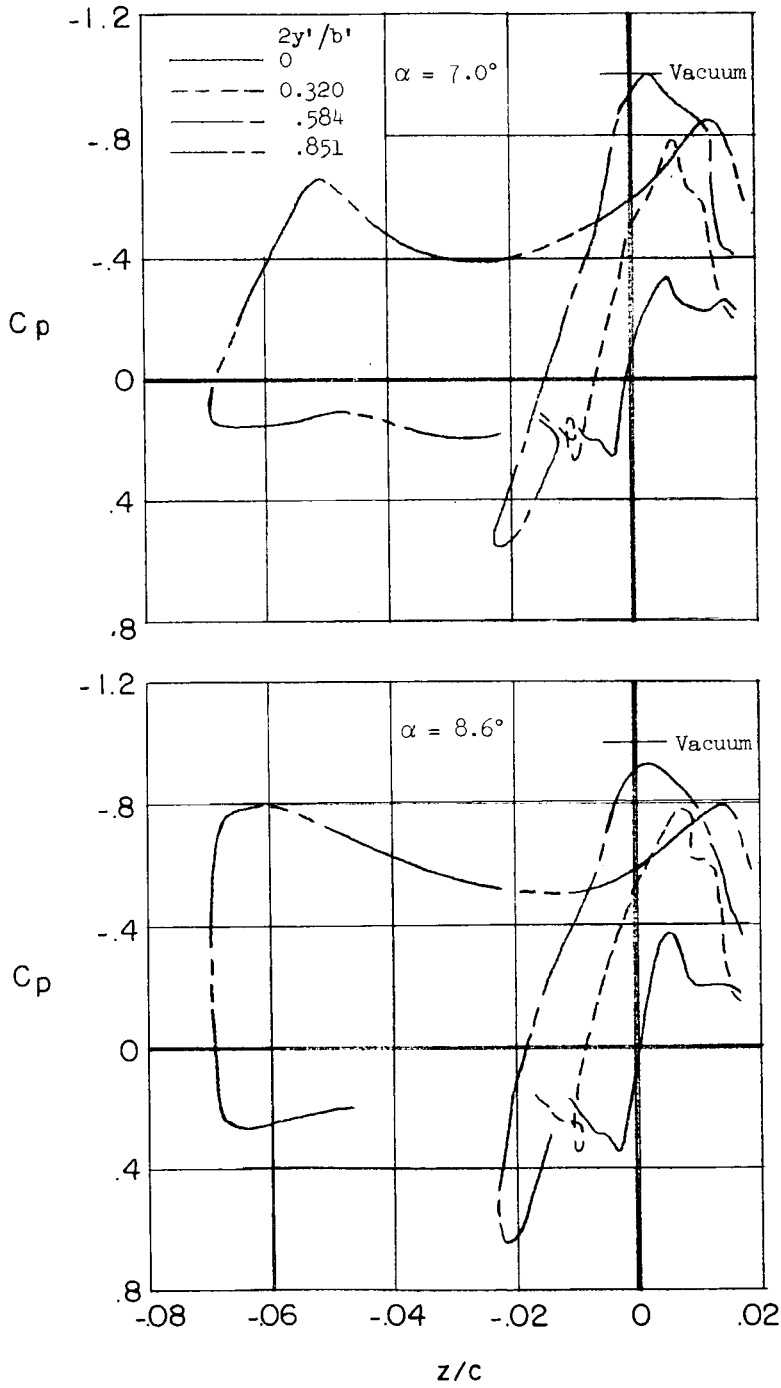
Figure 10.- Continued.



(d) $M \approx 1.19$.

Figure 10.- Continued.

H-1116



H-116

(d) Concluded.

Figure 10.- Concluded.

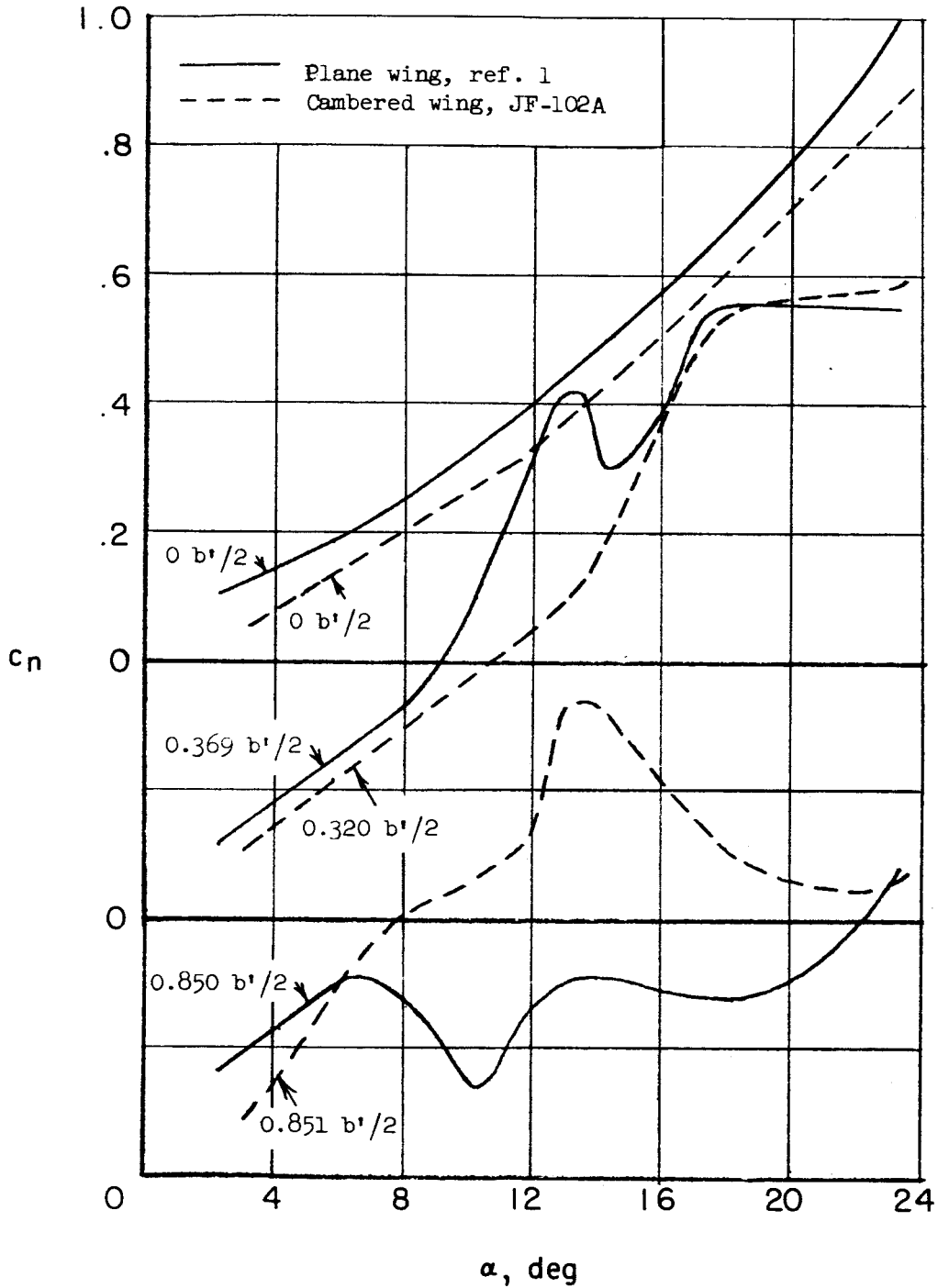
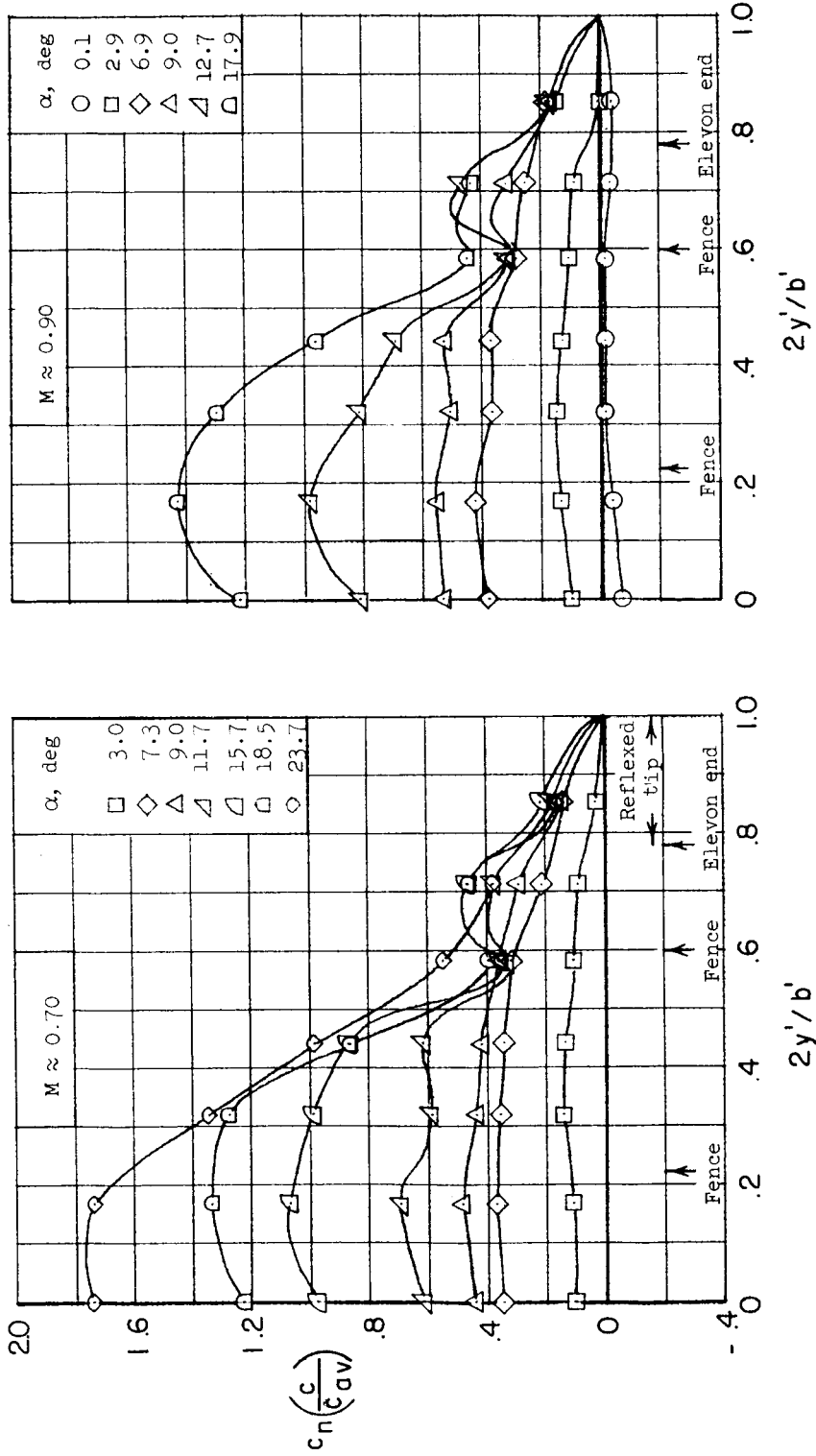


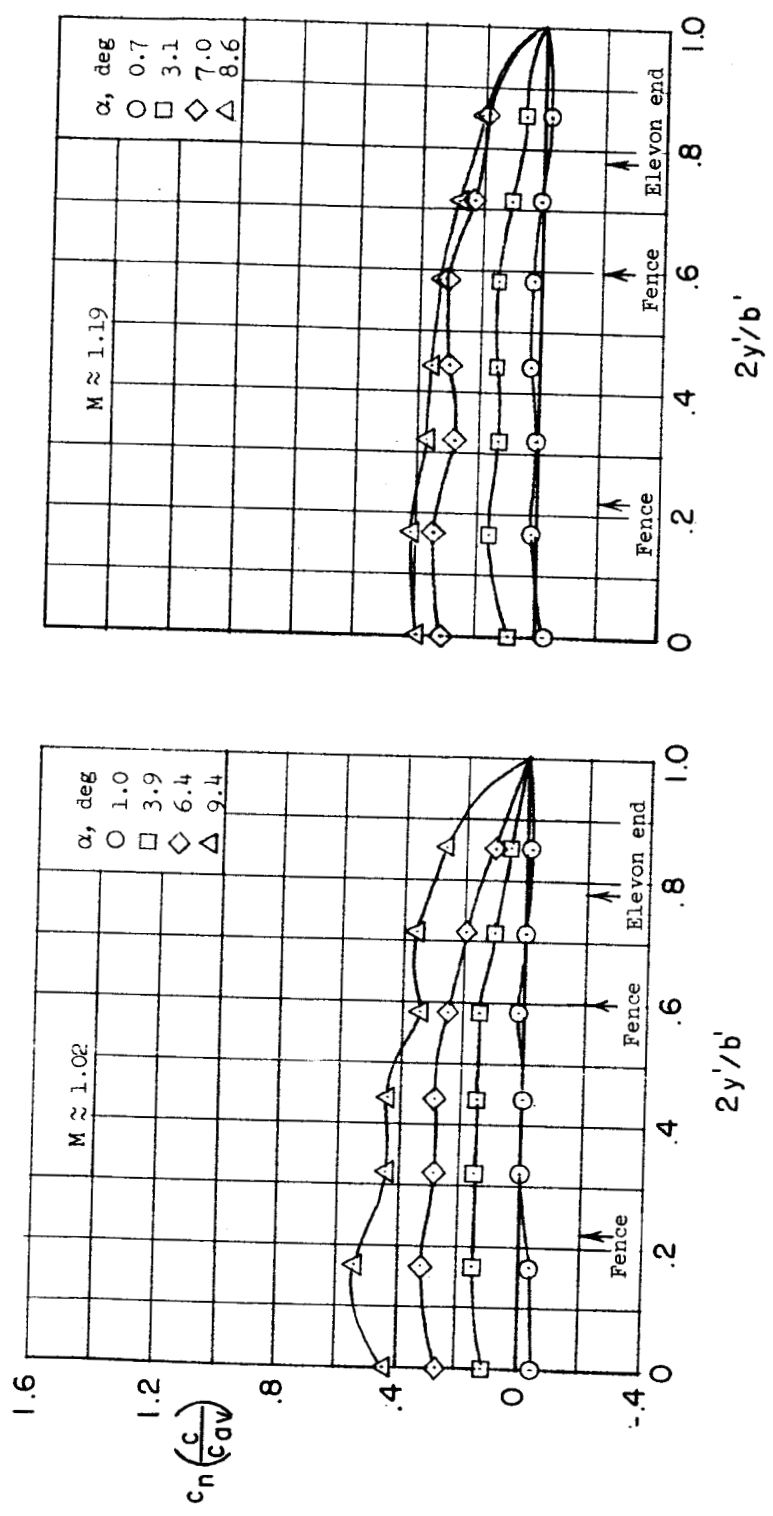
Figure 11.- Variation of section normal-force coefficient with angle of attack for conically cambered and plane delta wings at three stations. $M \approx 0.70$.

SECRET



(a) Subsonic Mach number.

Figure 12.- Spanwise load distribution over the wing of the JF-102A.



(b) Supersonic Mach number.

Figure 12.- Concluded.

SECRET

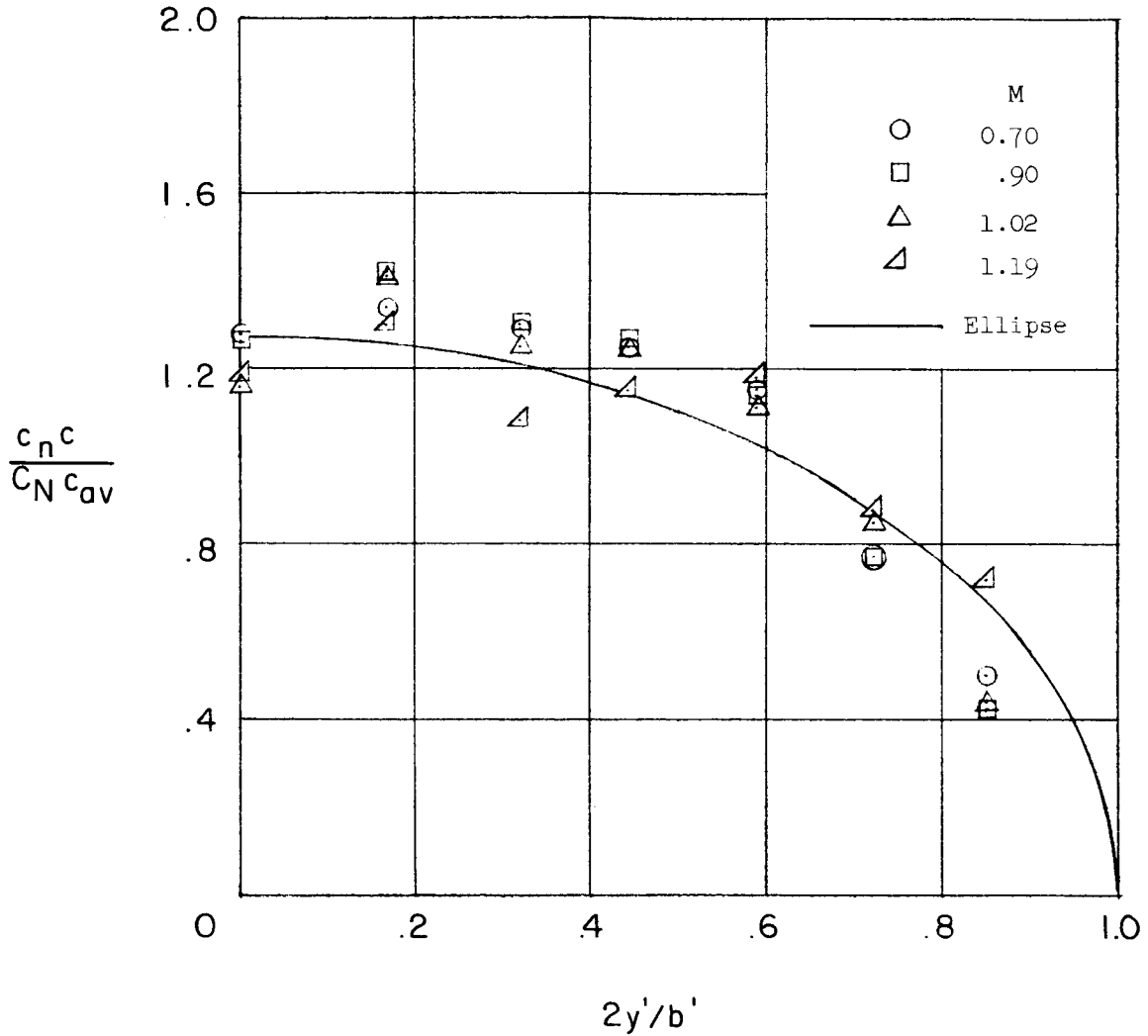


Figure 13.- Comparison of span-load distributions of cambered wing with an elliptic distribution. $\alpha \approx 7^\circ$.

SECRET

H-116

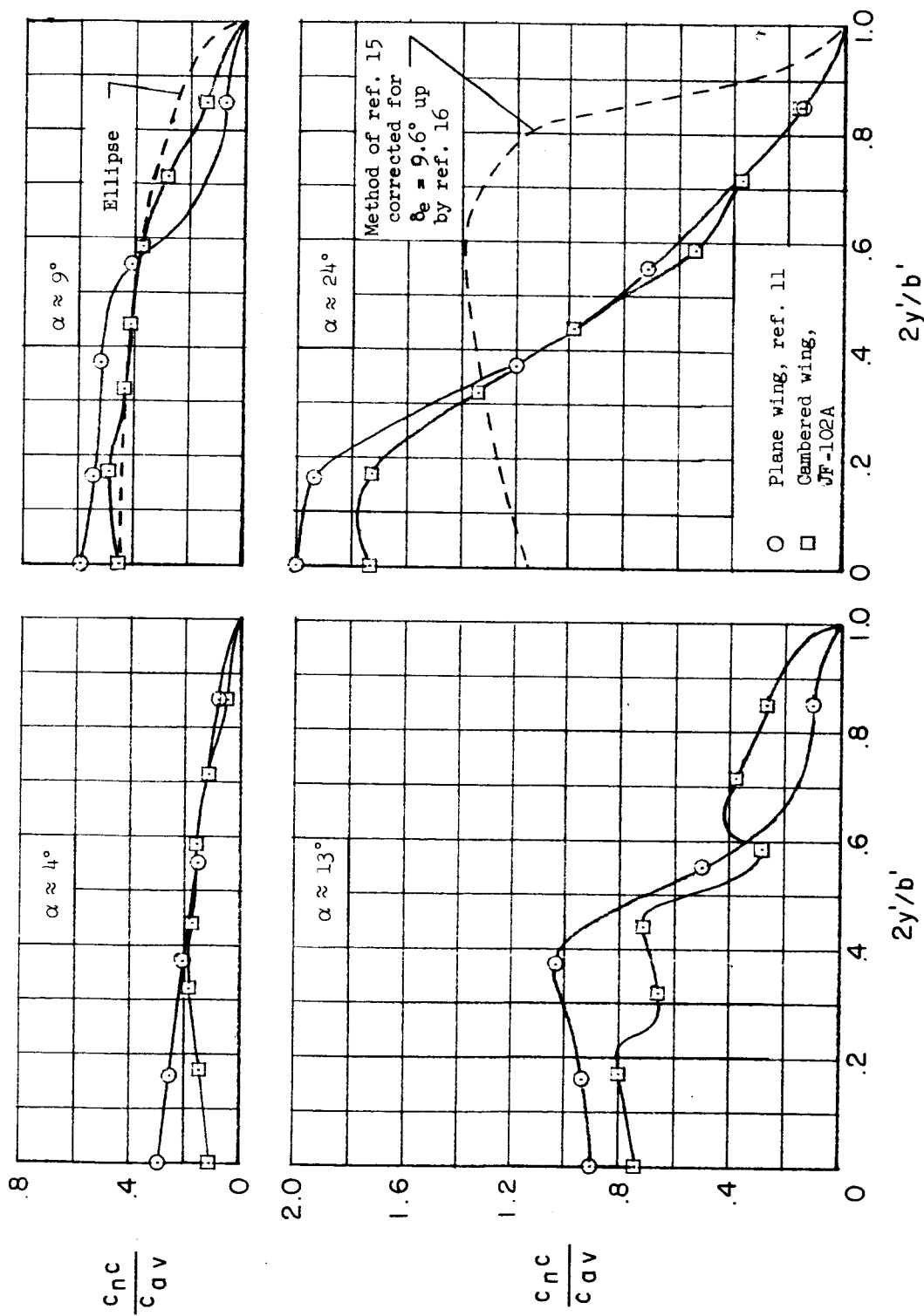


Figure 14.- Span-load distributions for conically cambered and plane delta wings. $M \approx 0.70$.